Novel sources of near– and mid–infrared femtosecond pulses for applications in gas sensing, pulse shaping and material processing

Łukasz Kornaszewski

Thesis submitted for the degree of Doctor of Philosophy

Heriot–Watt University

September 2008
Ultrafast Optics Group
Department of Physics
School of Engineering and Physical Sciences
David Brewster Building
Riccarton Campus
Edinburgh
EH14 4AS

Abstract

In this thesis the design, construction process and the performance of two femtosecond optical parametric oscillators and one second–harmonic generation femtosecond pulse shaper is described. One oscillator was applied to gas sensing while potential applications of other devices are outlined.

A Ti:sapphire oscillator was used to pump a periodically–poled lithium niobate–based optical parametric oscillator. This signal–resonant device was configured to produce broadband idler pulses tunable in the range of 2.7–3.4 µm. This wavelength coverage was matched to the ν_3 optical absorption band of methane, and Fourier–transform spectroscopy of a CH_4:N_2 mixture was implemented by employing a mid–IR silica photonic bandgap fibre simultaneously as a gas cell and an optical waveguide. Methane sensing below a 1% concentration was demonstrated and the main limiting factors were identified and improvements suggested.

Another optical parametric oscillator was demonstrated which was pumped by a commercial Yb:fibre master oscillator/power amplifier system and was based on a periodically–poled lithium niobate crystal. The signal was tunable between 1.42–1.57 µm and was intended as a source for a subsequent project for waveguide writing in silicon. The oscillator was a novel long–cavity device operating at 15 MHz. The 130 nJ pump pulse energies allowed for 21 nJ signal pulses at a pump power of 2 W. The performance of the oscillator was characterised via temporal and spectral measurements and the next steps of its development are outlined.

Finally a pulse shaper based on second harmonic generation in a grating–engineered periodically–poled lithium niobate crystal was demonstrated. Pulses from a 1.53 µm femtosecond Er:fibre laser were compressed and then used as the input to the shaper. The performance of the shaper was tested by performing cross–correlation frequency–resolved optical gating measurements on the output second harmonic pulses and this confirmed the successful creation of multiple pulses and other tailored shapes including square and chirped pulses, agreeing well with theoretical calculations.

Acknowledgements

First I must thank the father of it all, Derryck. He was the author of all new ideas for which I was merely an executor. Derryck is an excellent supervisor, always ready to help and offer his priceless advice, which was especially important for this thesis, as nonlinear optics is much broader area than I originally suspected and without his patient guidance I'm sure I wouldn't find my way through it.

On the second place there are my parents, but maybe they should be prior to Derryck. They gave me everything which I needed, to become who I am through all these 29 years. They must have been a bit scared having heard that I'm leaving for Scotland... All this time they were very supportive and their visits were extremely refreshing.

The next person without whom I wouldn't be where I am now, is my wife, Agnieszka. She was a bit worried, too, but without any protest followed me faithfully to Scotland and (as she says) will follow me wherever I will go. However, I must mention that, before we actually had a faintest idea of getting married, it was she who suggested me looking for a PhD in Scotland, so originally it was her thought. Now, since we have our son, Grzegorz, we make a happy family and she is undoubtedly the author of the success in this field.

Then comes my brother Tomasz and his family: wife Iza and children Andrzej, Ula and Monika. They live near Balfron in a nice woodland area and it was a great spot to go for our weekends in the country. Besides they helped me a lot in the beginning and especially in organising family events here, most importantly our wedding, being wonderful hosts, always willing to accommodate any number of guests we asked for. Plus, it was good to have our own Poles to talk in Polish!

People in the Ultrafast Optics Group were very warm and supportive: Euan, Stuart, Keith, Karl, Jinghua, Tobias, Barry, Stephanie, Stephan and Markus. Whenever I had questions or requests, they were trying to help or explain.

A very important bit was done by the background people — the mechanical workshop staff and the physics and electronics storespersons. They are real professionals and I recommend consulting them to everybody who wants a valuable advice or a last–minute job done for yesterday — they might help you even then!

It was a good time for me and whenever I recall my PhD in the future I think it will be a very warm memory, despite the weather here. I must say I like it now.

ACADEMIC REGISTRY
Research Thesis Submission

Name*:*	**Lukasz Kornaszewski**		
School/PGI:	**EPS**		
Version: *(i.e. First, Resubmission, Final)*	**Final**	Degree Sought (Award **and** Subject area)	**PhD in Physics**

Declaration

In accordance with the appropriate regulations I hereby submit my thesis and I declare that:

1) the thesis embodies the results of my own work and has been composed by myself
2) where appropriate, I have made acknowledgement of the work of others and have made reference to work carried out in collaboration with other persons
3) the thesis is the correct version of the thesis for submission and is the same version as any electronic versions submitted*.
4) my thesis for the award referred to, deposited in the Heriot-Watt University Library, should be made available for loan or photocopying and be available via the Institutional Repository, subject to such conditions as the Librarian may require
5) I understand that as a student of the University I am required to abide by the Regulations of the University and to conform to its discipline.

* *Please note that it is the responsibility of the candidate to ensure that the correct version of the thesis is submitted.*

Signature of Candidate*:*		Date:	

Submission

Submitted By *(name in capitals):*	
Signature of Individual Submitting:	
Date Submitted:	

For Completion in Academic Registry

Received in the Academic Registry by *(name in capitals):*			
Method of Submission *(Handed in to Academic Registry; posted through internal/external mail):*			
*E-thesis Submitted (**mandatory from November 2008)***			
Signature:		Date:	

Please note this form should bound into the submitted thesis. February 2008, November 2008

Contents

1 Introduction **1**

1.1 Linear pulse propagation in dispersive media 2

1.1.1 Gaussian pulses 2

1.1.2 Linear pulse propagation 3

1.2 Nonlinear crystal optics 5

1.2.1 Nonlinear polarisation 6

1.2.2 Coupled wave equations 7

1.2.3 Second harmonic generation 9

1.2.4 Optical parametric oscillation 11

1.2.5 Birefringent phase matching 14

1.2.6 Quasi–phase matching idea 15

1.2.7 Third order effects 17

1.2.8 Nonlinear evolution of the pulse shape 18

1.2.9 Materials suitable for nonlinear interactions 19

1.3 Femtosecond pulse measurement 20

1.3.1 Autocorrelation functions 21

1.3.2 Frequency–Resolved Optical Gating (FROG) 23

1.3.3 Cross–Correlation Frequency–Resolved Optical Gating . . . 25

1.3.4 Spectral Phase Interferometry for Direct Electric–field Reconstruction (SPIDER) 25

1.4 Outline 27

1.5 References 27

2 Methane detection using an optical parametric oscillator and photonic bandgap fibre **33**

2.1 Motivation and background — methane sensing 33

2.2 The origin of methane IR absorption spectra . . . 34
2.2.1 Rotations . . . 35
2.2.2 Oscillations . . . 37
2.3 Overview of methane sensing techniques . . . 43
2.3.1 Detection methods . . . 44
2.3.2 Spectral ranges and light sources . . . 45
2.3.3 Summary of detection schemes . . . 47
2.4 Optical parametric oscillator design . . . 49
2.5 Fourier transform spectrometer . . . 51
2.5.1 FTIR data acquisition and processing . . . 52
2.5.2 Experimental details of the FTIR spectrometer . . . 55
2.5.3 Sampling and resolution criteria . . . 55
2.6 Optical parametric oscillator characterisation . . . 56
2.7 Photonic bandgap fibre as a gas cell . . . 60
2.8 Characterisation of candidate fibres . . . 64
2.9 Methane sensing experiment . . . 66
2.9.1 Spectrum calibration . . . 69
2.10 Conclusions . . . 73
2.11 References . . . 75

3 Design and construction of a high–energy femtosecond optical parametric oscillator for silicon material processing 82
3.1 Motivation and background – femtosecond material processing . . 82
3.1.1 The work outline . . . 85
3.2 Pump laser characterisation . . . 86
3.2.1 Repetition frequency . . . 86
3.2.2 Spectra for different output powers . . . 87
3.2.3 Temporal characteristics and compression scheme . . . 88
3.2.4 Pump beam profile measurement . . . 91
3.3 Crystal design . . . 94
3.4 Cavity design . . . 96
3.5 System characterisation . . . 97
3.5.1 Slope efficiency . . . 97
3.5.2 Optimal output coupling . . . 98

3.5.3 Signal tunability . . . 101
3.5.4 Cavity group delay dispersion . . . 103
3.5.5 Signal pulse measurement . . . 105
3.5.6 Phase noise measurement . . . 105
3.6 Signal dynamics simulations . . . 107
3.7 Conclusions and outlook . . . 109
3.8 References . . . 110

4 Femtosecond pulse shaping with engineered quasi–phase matching of second harmonic generation in aperiodically poled lithium niobate 113
4.1 Motivation and background — pulse shaping . . . 113
4.2 Programmable methods of femtosecond pulse shaping . . . 114
4.2.1 Liquid crystal modulators . . . 114
4.2.2 Deformable mirrors . . . 118
4.2.3 Other devices . . . 120
4.3 Static methods of femtosecond pulse shaping . . . 121
4.3.1 Fibre Bragg gratings . . . 122
4.3.2 Poled nonlinear crystals . . . 122
4.4 Spectral and temporal transfer functions . . . 123
4.4.1 The transfer function concept . . . 123
4.4.2 Pulse propagation in a poled crystal . . . 124
4.4.3 The crystal transfer function . . . 125
4.5 Design of aperiodic gratings for pulse shaping . . . 126
4.6 Pulse shaping experiment . . . 129
4.6.1 Overview . . . 129
4.6.2 Er:fibre laser . . . 130
4.6.3 Measurement and optimisation of the shaped SH pulses . . . 133
4.7 Comparison with theory . . . 137
4.8 Conclusions . . . 138
4.9 References . . . 139

5 Conclusions and outlook 145
5.1 References . . . 148

List of Figures

1.1 Second harmonic generation 10
1.2 Wavevector relation in SHG 11
1.3 Optical parametric oscillation 12
1.4 Optical parametric oscillator 13
1.5 Birefringent phase matching 14
1.6 Quasi–phase–matching idea 16
1.7 Autocorrelation measurement setup 21
1.8 Second–order autocorrelation functions 22

2.1 Dipole oscillation during rotation 35
2.2 Methane molecule 36
2.3 Rotational energy levels 37
2.4 CO_2 molecule oscillation modes 38
2.5 Vibration–rotation energy levels 40
2.6 Vibration modes of the methane molecule 41
2.7 Methane absorption in linear scale 42
2.8 Methane absorption in logarithmic scale 43
2.9 OPO cavity schematic 50
2.10 OPO crystal mount 51
2.11 Michelson interferometer used to FTIR measurements 52
2.12 Example of the intensity fringes from the oscilloscope screen 53
2.13 Schematic of FTIR data processing 54
2.14 OPO spectrum in the visible and near–IR 57
2.15 OPO power and tunability 58
2.16 OPO example spectra 59
2.17 1D–bandgap structure 60
2.18 2D–bandgap structure 61

2.19 Cross–section of a photonic bandgap fibre used in this experiment . 62
2.20 Bragg fibre and photonic fibre 62
2.21 FTIR measurement setup 65
2.22 Fibres' transmission curves 65
2.23 Fibre terminator 67
2.24 Gas installation 67
2.25 Screenshots for measurements with methane and without it 68
2.26 Result of 5% concentration measurement 69
2.27 Effect of shortening of the calibration wavelength 70
2.28 Calibrated result of 5% concentration measurement 71
2.29 Comparison of methane absorption for different concentrations . . 72
2.30 Improved measurement setup suggestion 74

3.1 Written waveguide structure 85
3.2 Spectra of the pump laser as a function of output power 87
3.3 FROG maps for the pump pulses 88
3.4 Grating compressor 89
3.5 Autocorrelation functions 90
3.6 Compressed pulse duration 90
3.7 Beam radius measurement data 92
3.8 Pump beam radius model 93
3.9 OPO theoretical tunability 95
3.10 OPO crystal 96
3.11 OPO cavity 96
3.12 OPO signal mode 97
3.13 OPO slope efficiency 98
3.14 Measurement of output power as a function of output coupling . . 99
3.15 Output power as a function of output coupling 100
3.16 Signal spectra 102
3.17 OPO oscillation conditions 103
3.18 Cavity GDD 104
3.19 OPO autocorrelations 105
3.20 OPO phase noise 106
3.21 OPO tunability simulation 108

4.1 LCM operating principle 115
4.2 Different types of LCM geometry 116
4.3 Transmittive geometry of programmable pulse shaping 117
4.4 Piezo–actuated deformable reflector 119
4.5 Bimorph piezo deformable mirror 119
4.6 Electrostatic deformable mirror 120
4.7 Q_u definition 125
4.8 Design algorithm flowchart 127
4.9 Crystal design 128
4.10 APPLN domain sizes 129
4.11 Experimental setup 130
4.12 Er:fibre oscillator 131
4.13 Er:fibre oscillator spectrum 132
4.14 Er:fibre oscillator autocorrelation 132
4.15 Shaped pulse cross–correlations 133
4.16 XFROG measurement program 135
4.17 XFROG measurement setup 136
4.18 XFROG maps of shaped pulses 136
4.19 Measured and calculated shaped pulses 137

List of publications

Journal articles

1 L. Kornaszewski, N. Gayraud, J. M. Stone, W. N. MacPherson, A. K. George, J. C. Knight, D. P. Hand and D. T. Reid, "Mid–infrared methane detection in a photonic bandgap fiber using a broadband optical parametric oscillator", *Optics Express* **15** (18), p. 11219-11224 (2007).

2 L. Kornaszewski, M. Kohler, U. K. Sapaev and D. T. Reid, "Designer femtosecond pulse shaping using grating–engineered quasi–phase–matching in lithium niobate", *Optics Letters* **33** (4), 3780380 (2008).

3 Nicolas Gayraud, Lukasz W. Kornaszewski, James M. Stone, Jonathan C. Knight, Derryck T. Reid, Duncan P. Hand and William N. MacPherson, "Mid–infrared gas sensing using a photonic bandgap fiber", *Applied Optics* **47** (9), 1269-1277 (2008).

Conference presentations

1 L. W. Kornaszewski, N. Gayraud, W. N. MacPherson, D. P. Hand, D. T. Reid, J. M. Stone, A. K. George, J. C. Knight, "Mid–infrared methane sensing using an optical parametric oscillator and a photonic bandgap fiber as a gas cell", *Conference on Lasers and Electro-Optics/Quantum Electronics and Laser Science Conference and Photonic Applications Systems Technologies 2007 Technical Digest*, paper CThO3, (Optical Society of America, Washington, DC), 2007.

2 L. Kornaszewski, M. Kohler, D. T. Reid and U. K. Sapaev, "Designer femtosecond pulse shaping using grating–engineered quasi-phasematching in lithium

niobate", *Conference on Lasers and ElectroOptics/Quantum Electronics and Laser Science Conference and Photonic Applications Systems Technologies 2008 Technical Digest*, paper CWK3, (Optical Society of America, Washington, DC), 2008.

3 Łukasz Kornaszewski, Markus Kohler, Usman K. Sapaev and Derryck T. Reid, "Designer femtosecond pulse shaping using grating–engineered quasi–phase-matching in lithium niobate," Paper MONIc.9 in Ultrafast Optics, Stresa, 2008.

4 Łukasz Kornaszewski, Markus Kohler, Usman K. Sapaev and Derryck T. Reid, "Designer femtosecond pulse shaping using grating–engineered quasi–phase-matching in lithium niobate," Paper QEP 2.7 in Photon08 (QEP–18), Edinburgh, 2008.

Chapter 1

Introduction

Since the invention of laser in 1960 [1.1, 1.2], when massive and well–controllable light intensities became readily available in laboratories, industry, and even in everyday life, there has been a huge interest in exploiting the light–matter interactions achievable under these extreme conditions for obtaining the whole family of nonlinear optical effects. The nonlinear effects in question are widely used for light frequency conversion, ultrashort pulse generation and characterisation as well as the construction of new, otherwise unobtainable laser–like sources showing some interesting, unique and useful properties.

Optical frequency conversion using the nonlinear response of certain crystals, demonstrated as early as the next year after laser devices became available [1.3, 1.4, 1.5] is nowadays a very important technique for building tunable lasers and is generally capable of extending the spectrum available from these sources to the entire range from terahertz ($\lambda \approx 1$ mm) to X–ray wavelengths ($\lambda \approx 1$ nm). Nonlinearities suitable for the construction of laser sources based on Kerr–lens modelocking (as originally demonstrated using the Ti:sapphire crystal [1.6]), and the broad extension of the available bandwidth of ultrafast lasers became possible due to the nonlinear effects in optical fibres and other materials [1.7, 1.8, 1.9]. Also, pulse measurement techniques in the ultrashort–duration regime rely on nonlinear processes to exactly characterise these phenomena, which are far too fast for any electronics–based monitoring system.

The unique properties of many nonlinear crystals can be used for even more versatile pulse generation and characterisation. Some materials are naturally suitable for certain applications under carefully chosen conditions, but others can be

freely designed and engineered using special formulæ and manufacturing techniques to configure favourable properties for dedicated processes or to become the basis of novel, versatile light sources. The most notable example of such engineering would be the periodic poling of a ferroelectric crystal to obtain a non–birefringent phasematching for a nonlinear process, first proposed by Armstrong et al. [1.10] and Franken et al. [1.11]. A more sophisticated application is the direct design of a crystal transfer function by aperiodic poling for the generation of shaped femtosecond pulses [1.12, 1.13].

In this PhD thesis I am presenting several studies involving complementary, novel applications of poled nonlinear crystals, describing the details of design–related theory and calculations, together with the experimental configurations and results. I begin with a general introduction to the fundamental concepts of nonlinear crystal optics.

1.1 Linear pulse propagation in dispersive media

1.1.1 Gaussian pulses

A simple case of an optical pulse useful for estimating the linear and nonlinear effects for its propagation is the Gaussian pulse, i.e. the spectral amplitude is a Gaussian function:

$$E(\omega) = E_0 \exp\left[-(a + ib)\,\omega^2\right] \tag{1.1}$$

with the full–width at half–maximum (FWHM):

$$\Delta\omega = \sqrt{\frac{\ln 4}{a}}. \tag{1.2}$$

It is natural to define the pulse shape in the frequency domain as it is well understood how a plane wave propagates in both linear and nonlinear regimes through a medium with given linear and nonlinear refractive indices $n_{\mathrm{L}}(\omega)$ and $n_{\mathrm{NL}}(\omega)$. If the spectral amplitude of any pulse is known, then the numerical modelling of the propagation effects can be performed (phase added and/or amplitude modified) to all the spectral components of the pulse. For the same reason analytical solutions of the propagation problems are also presented in the frequency domain.

The temporal profile of the pulse is given by the inverse Fourier transform of the $E(\omega)$:

$$E(t) = E_0' \exp\left[-\frac{at^2}{4\left(a^2+b^2\right)}\right] \exp\left[i\frac{bt^2}{4\left(a^2+b^2\right)}\right]. \tag{1.3}$$

The quantities a and b are responsible for the pulse duration. The a parameter is a positive constant for a given spectral shape and sets the lower limit for the pulse duration. The b parameter may be negative, zero or positive for every spectrum and describes the dispersive broadening of the pulse in the time domain.

The common measure of the pulse duration is the FWHM value, and for the Gaussian shape it is given by:

$$\Delta\tau = 2\sqrt{\left(\frac{a^2+b^2}{a}\right)\ln 4}. \tag{1.4}$$

From (1.4) it is clear that any non–zero b value increases $\Delta\tau$, stretching the pulse in time. The minimum duration for a given spectrum is present for $b = 0$ and equals:

$$\Delta\tau_{\mathrm{MIN}} = 2\sqrt{a\ln 4}. \tag{1.5}$$

When the b parameter is non–zero and the pulse duration is longer than the minimum, the pulse is called "chirped".

A good measure of chirp is the product $\Delta\omega\Delta\tau$. For a given pulse shape it has a constant minimum value, independent of the particular pulse details, corresponding to the zero chirp. In the case of Gaussian pulses, $\Delta\omega\Delta\tau = 2\ln 4 \approx 2.77$. Clearly when the pulse is chirped this quantity is bigger, and this way the duration–bandwidth product may be used as a chirp measurement.

The Gaussian shape can be found in the actively modelocked lasers, but there are more analytical solutions to the problems encountered in optical pulse generation. For example, a common shape found in the passively modelocked oscillators is $\mathrm{sech}^2(t)$. Its duration–bandwidth product is 1.98. On the other hand, in the amplifier regime, parabolic shapes are the solutions of the nonlinear Schrödinger equation. This shape is characterised with a theoretical duration–bandwidth product of 4.59.

1.1.2 Linear pulse propagation

Any dielectric medium has a frequency–dependent refractive index and the result is the phenomenon known as dispersion; as the optical frequency changes, the

wavevector in a medium also changes in a complicated way according to the dispersion formula:

$$|\vec{k}| = \frac{n(\omega)\omega}{c}, \tag{1.6}$$

where $n(\omega)$ is a frequency–dependent refractive index. This has a broadening effect for the optical pulses consisting of a finite spectrum because different spectral components have, in general, different phase velocities:

$$v_\varphi = \frac{c}{n(\omega)}. \tag{1.7}$$

The optical pulse will be stretched after propagating through a block of a transparent material. Rigorous analysis of the influence of the $k(\omega)$ to the pulse shape involves representing $k(\omega)$ as a Taylor series around the central frequency ω_0:

$$k(\omega) = k(\omega_0) + \left.\frac{dk}{d\omega}\right|_{\omega_0} (\omega - \omega_0) + \frac{1}{2}\left.\frac{d^2k}{d\omega^2}\right|_{\omega_0} (\omega - \omega_0)^2 + \dots \tag{1.8}$$

When searching for the effect of dispersion on the pulse, the accumulated phase must be added to the pulse shape:

$$\begin{aligned} E(\omega, z) &= E(\omega, z_0)e^{-ik(\omega)z} \Rightarrow \\ E(t, z) &= e^{i(\omega_0 t - k_0 z)}A(t', \omega_0), \end{aligned} \tag{1.9}$$

where $A(t', \omega_0)$ is the pulse envelope, propagating with the group velocity $v_g = [(dk/d\omega)|_{\omega_0}]^{-1}$. The carrier wave travels at the phase velocity $v_\varphi = \omega_0/k_0 = c/n(\omega_0)$. The fact that v_g depends from the optical frequency is the origin of pulse broadening while propagating. Actually, the next Taylor term

$$\frac{d^2k}{d\omega^2} = \frac{d}{d\omega}\left(\frac{1}{v_g}\right) \tag{1.10}$$

is defined as the group–velocity dispersion (GVD) and is a good measure of the chirp accumulated by the pulse due to the propagation through the material. When multiplied by the distance travelled, it becomes the group–delay dispersion GDD $= L \cdot d^2k/d\omega^2 = d^2\varphi/d\omega^2$, or the difference in the arrival times for different spectral components of the pulse.

When describing dispersion, commonly used is another parameter, β, which is defined as the imaginary part of a propagation constant γ:

$$\begin{aligned} \frac{A_0}{A(z)} &= e^{\gamma z} \\ \gamma &= \alpha + i\beta, \end{aligned} \tag{1.11}$$

where A_0 is the initial amplitude, $A(z)$ is the amplitude after some distance z, and α is called the attenuation constant. β is known as the phase constant and is measured in radians per meter. This notation is especially useful in the context of optical fibres.

1.2 Nonlinear crystal optics

Nonlinear phenomena in optics are defined as those light–matter interactions in which the optical properties of medium and the strength of the process depend on the light intensity. The dielectric polarisation P is always a nonlinear function of the electric light field E:

$$\vec{P}(\vec{E}) = \epsilon_0 \left(\chi^{(1)} \vec{E} + \chi^{(2)} \vec{E}^2 + \chi^{(3)} \vec{E}^3 + \dots \right), \tag{1.12}$$

but for weak beams all components of this expansion higher than first order may be neglected as they give no detectable effect. When it comes to laser light, at least some of the components must be taken into account and cause very spectacular and useful phenomena as second (third, fourth, ...) harmonic generation, difference– and sum–frequency generation, optical rectification, self–phase modulation, self–focusing and a whole array of parametric processes, including generation and amplification. In these processes the spectral, temporal and geometrical profiles of an input beam may be altered just by the interaction of the light with the medium, even though it is completely transparent. However, some nonlinear processes are not only responsible for exchanging energy between light beams, but can also remove the energy from the beam and transfer it to the medium (e.g. Raman scattering), so in those cases the medium is non–transparent.

It is thanks to nonlinear phenomena that we can build laser sources which are not formally lasers, but nevertheless act as wavelength converters. Not all frequency regions are covered by available laser transitions, but parametric ($\chi^{(2)}$) and Raman ($\chi^{(3)}$) oscillators and amplifiers make it possible to shift laser outputs far from their original frequencies.

The topic of nonlinear optics is the subject of many textbooks which discuss all the aspects in detail. As an example of a thorough review, the books [1.14] or [1.15] may be suggested.

1.2.1 Nonlinear polarisation

In a dielectric medium, the polarisation $\vec{P}$ is a field representing the density of the electric dipole moments.

In a linear case, where the external electric field in the material is not too strong, the polarisation stays in a simple relation to the electric field $\vec{E}$, but is not necessarily collinear to it:

$$P_{\mathrm{i}} = \epsilon_0 \sum_{\mathrm{j}} \chi_{\mathrm{ij}} E_{\mathrm{j}}, \tag{1.13}$$

where i and j are indices representing Cartesian coordinates, ϵ_0 is the vacuum permittivity and χ_{ij} is the electric susceptibility tensor.

For more intense electric fields, as in the case of laser light, the linear approximation is not valid and nonlinear components must be taken into account:

$$P_{\mathrm{i}}(\vec{E}) = \epsilon_0 \left(\underbrace{\sum_{\mathrm{j}} \chi^{(1)}_{\mathrm{ij}} E_{\mathrm{j}}}_{P_{\mathrm{L}}/\epsilon_0} + \underbrace{\sum_{\mathrm{jk}} \chi^{(2)}_{\mathrm{ijk}} E_{\mathrm{j}} E_{\mathrm{k}} + \sum_{\mathrm{jkl}} \chi^{(3)}_{\mathrm{ijkl}} E_{\mathrm{j}} E_{\mathrm{k}} E_{\mathrm{l}} + \ldots}_{P_{\mathrm{NL}}/\epsilon_0} \right), \tag{1.14}$$

where $\chi^{(\mathrm{p})}$ are the electric susceptibility tensors of the respective p rank. The non–zero elements of the tensors of $p > 1$ determine the value of the nonlinear polarisation P_{NL} which is the origin of the nonlinear processes.

In general, $\vec{P}$ is not constant and may depend upon the strength of the $\vec{E}$ field (nonlinearity), the polarisation of the $\vec{E}$ field and its direction of propagation (birefringence), the optical frequency (dispersion), the position in a non–uniform material and the $\vec{E}$ field history (hysteresis). To highlight the nonlinear response, the term P_{NL} is separated, which reflects the dependence of polarisation from the higher–order powers of the electric field, or the non–zero value of $\chi^{(\mathrm{p})}$ for $p > 1$.

Commonly in the literature the nonlinear tensor d is used, which for the second–order nonlinearity is defined as follows:

$$d_{\mathrm{ijk}} = \frac{1}{2} \chi^{(2)}_{\mathrm{ijk}}. \tag{1.15}$$

The i^{th} component of a monochromatic travelling optical field in the medium may be represented as:

$$\begin{aligned} E^{\omega}_{\mathrm{i}}(z,t) &= \frac{1}{2}\left[E^{\omega}_{\mathrm{i}} e^{i(\omega t - kz)} + E^{\omega}_{\mathrm{i}} e^{-i(\omega t - kz)} \right] = \\ E^{\omega}_{\mathrm{i}}(z,t) &= \frac{1}{2}\left[E^{\omega}_{\mathrm{i}} e^{i(\omega t - kz)} + c.c. \right], \end{aligned} \tag{1.16}$$

where z and t are spatial and temporal propagation coordinates, ω is the optical oscillation frequency of the electric field and k is the magnitude of the wavevector defined as $|\vec{k}| = n\omega/c$. If there are two or more electric fields present oscillating at different optical frequencies $\omega_1, \omega_2, \ldots$, multiplication of their respective $\exp[i(\omega_j t - kz)]$ components by each other according to (1.14) yields the polarisation terms containing frequencies other than the fundamental frequency, namely their linear combinations, e.g. $\omega_1 + \omega_2$, $\omega_1 - \omega_2$, $\omega_1 + \omega_2 + \omega_3$,.... The result is a new electric field oscillating at the new frequency, created thanks to the nonlinear interaction in the medium and propagating in it as a real optical field.

1.2.2 Coupled wave equations

The equation (1.14) shows the coupling between the fields propagating in the medium. Existing electric fields interact to create a new field which, in turn, in combination with the previously existing fields, will interact too and they will co–propagate further, continuously exchanging energy with each other. This energy flow rate and direction depend on the material structure (χ), the fields strength and relative phases. To find the exact formulae governing the propagation of light in a medium, it is necessary to refer to general electromagnetism, namely the Maxwell's Equations [1.16]:

$$\begin{aligned} \nabla \times \vec{E} &= -\frac{\partial \vec{B}}{\partial t} \\ \nabla \times \vec{H} &= \frac{\partial \vec{D}}{\partial t} + \vec{J}, \end{aligned} \tag{1.17}$$

which describe the interdependence between oscillating electric and magnetic fields in a medium. The detailed definitions of the components are:

$$\begin{aligned} \vec{J} &= \sigma \vec{E} \\ \vec{B} &= \mu \vec{H} \\ \vec{D} &= \epsilon_0 \vec{E} + \vec{P} = \epsilon_0 (1 + \chi_L)\vec{E} + \vec{P}_{NL} = \epsilon \vec{E} + \vec{P}_{NL}, \end{aligned} \tag{1.18}$$

where $\vec{J}$ is the current density, σ is the conductivity, $\vec{B}$ is the magnetic field, μ is the permeability, $\vec{H}$ is the magnetising field, and $\vec{D}$ is the electric displacement field in the medium. χ_L is the linear part of the susceptibility, $\chi^{(1)}$, whereas P_{NL} contains all the higher orders $\chi^{(p)}$ for $p > 1$.

If the curl of the equations of the form (1.17) is taken, then, according to the general mathematical vector identity stating that:

$$\nabla \times (\nabla \times \vec{A}) = \nabla(\nabla \cdot \vec{A}) - \nabla^2 \vec{A}, \tag{1.19}$$

we may rewrite the left–hand side of the first equation (1.17) as:

$$\nabla \times (\nabla \times \vec{E}) = \nabla(\underbrace{\nabla \cdot \vec{E}}_{=0}) - \nabla^2 \vec{E} = -\nabla^2 \vec{E} = \nabla \times \mathbb{L}, \tag{1.20}$$

where $\nabla \cdot \vec{E} = 0$ due to the material being dielectric and possessing no free electric charges. The right–hand side of the formula is:

$$\begin{aligned} \nabla \times \left(-\frac{\partial \vec{B}}{\partial t} \right) &= \frac{-\partial \left(\nabla \times \vec{B} \right)}{\partial t} = -\mu_0 \frac{\partial \left(\nabla \times \vec{H} \right)}{\partial t} = -\mu_0 \frac{\partial}{\partial t} \left(\frac{\partial \vec{D}}{\partial t} + \overbrace{\vec{J}}^{=0} \right) = \\ &= -\mu_0 \frac{\partial^2 \left(\epsilon \vec{E} + \vec{P}_{\mathrm{NL}} \right)}{\partial t^2} = \nabla \times \mathbb{R}, \end{aligned} \tag{1.21}$$

where $\vec{J} = 0$ due to the dielectric nature of the medium. Comparing the sides $\nabla \times \mathbb{L}$ and $\nabla \times \mathbb{R}$ we obtain the nonlinear wave equation:

$$\nabla^2 \vec{E} = \mu_0 \epsilon \frac{\partial^2 \vec{E}}{\partial t^2} + \mu_0 \frac{\partial^2 \vec{P}_{\mathrm{NL}}}{\partial t^2}, \tag{1.22}$$

which describes the spatio–temporal dependence of the electric field from itself or from other fields present in the material.

For a simple analysis of a three–wave mixing process all three, independent waves can be assumed as monochromatic and propagating in one direction z:

$$\begin{aligned} E_{\mathrm{i}}^{\omega_1}(z,t) &= \frac{1}{2} \left[E_{1\mathrm{i}}^{\omega} e^{i(\omega_1 t - k_1 z)} + c.c. \right] \\ E_{\mathrm{j}}^{\omega_2}(z,t) &= \frac{1}{2} \left[E_{2\mathrm{j}}^{\omega} e^{i(\omega_2 t - k_2 z)} + c.c. \right] \\ E_{\mathrm{k}}^{\omega_3}(z,t) &= \frac{1}{2} \left[E_{3\mathrm{k}}^{\omega} e^{i(\omega_3 t - k_3 z)} + c.c. \right] \end{aligned} \tag{1.23}$$

As the propagation direction is z, the polarisation of each of the waves can be either x or y and is symbolised by independent i, j and k indices. The nonlinear polarisation under the examination oscillates at the frequency $\omega_3 = \omega_1 + \omega_2$.

The second order nonlinear polarisation at the frequency ω_1 is $P_{\mathrm{NL,i}}^{\omega_1} = 2\varepsilon_0 d_{ijk} E_j E_k$ and this is the equation describing the relation of the amplitudes and phases of the three waves mixing in the medium. Multiplication of E_j by E_k introduces new

frequency terms, namely $\omega_2 + \omega_3$, $\omega_2 - \omega_3$ and $\omega_3 - \omega_2$. In this analysis we are interested in the process involving only three frequencies so the polarisation term showing the coupling to the wave with $\omega_1 = \omega_3 - \omega_2$ becomes:

$$P^{\omega_1}_{\mathrm{NL},i}(z,t) = 2\varepsilon_0 d_{ijk} E^{\omega_2}_j(z)[E^{\omega_3}_k(z)]^*. \tag{1.24}$$

Substituting the E and P fields at frequency ω_1 to the nonlinear wave equation gives the first wave equation for the amplitude of the E^{ω_1} field showing its evolution during the propagation through the medium:

$$\frac{dE^{\omega_1}_i}{dz} = -\frac{i\omega_1}{cn_1} d_{ijk} E^{\omega_2}_j \left(E^{\omega_3}_k\right)^* \exp\left(-i\Delta k z\right), \tag{1.25}$$

where the slowly varying envelope approximation was used ($\nabla^2 E^{\omega_1}_i \approx 0$) together with some simplifying relationships:

$$\begin{aligned} k_1 &= \frac{n_1\omega_1}{c} \\ c &= \frac{1}{\sqrt{\mu_0\varepsilon_0}}. \end{aligned} \tag{1.26}$$

A similar analysis can be performed for the other frequencies ω_2 and ω_3 and the set of coupled wave equations for the quadratic polarisation is completed by:

$$\frac{d\left(E^{\omega_2}_j\right)^*}{dz} = \frac{i\omega_2}{cn_2} d_{ijk} E^{\omega_1}_i \left(E^{\omega_3}_k\right)^* \exp\left(i\Delta k z\right) \tag{1.27}$$

$$\frac{dE^{\omega_3}_k}{dz} = -\frac{i\omega_3}{cn_3} d_{ijk} E^{\omega_1}_j E^{\omega_2}_k \exp\left(i\Delta k z\right), \tag{1.28}$$

and the following second–order nonlinear processes are described by these equations: sum frequency generation, difference frequency generation and parametric amplification and oscillation.

In the remainder of the thesis unless otherwise stated, I will be referring by default to the lowest order nonlinearities, namely those involving $\chi^{(2)}$.

1.2.3 Second harmonic generation

Second harmonic generation (SHG) is the degenerate case of sum frequency generation, where two electric fields oscillating at optical frequencies polarise the medium and force it to radiate another optical field at the new frequency. In the case of SHG the new frequency is equal to the doubled fundamental frequency, hence the alternative name — frequency doubling. This phenomenon was discovered just the year after the first laser construction [1.3]. It is observable when

a strong electric field at the frequency ω is present in a suitable material. This field may be represented according to (1.16). The non–zero value of some $\chi^{(2)}$ components will cause the appearance of the electric fields of the form:

$$E_{\mathrm{i}}^{\omega_{\mathrm{NEW}}}(z,t) = \epsilon_0 \sum_{\mathrm{jk}} \chi_{\mathrm{ijk}}^{(2)} E_{\mathrm{j}} E_{\mathrm{k}} \left\{ \left[e^{i(\omega_{\mathrm{j}} t - k_{\mathrm{j}} z)} + c.c. \right] \left[e^{i(\omega_{\mathrm{k}} t - k_{\mathrm{k}} z)} + c.c. \right] \right\}. \tag{1.29}$$

One of the fields is that of the doubled frequency 2ω:

$$E_{\mathrm{i}}^{2\omega}(z,t) = \epsilon_0 \sum_{\mathrm{jk}} \chi_{\mathrm{ijk}}^{(2)} E_{\mathrm{j}} E_{\mathrm{k}} \left[e^{2i(\omega_{\mathrm{j}} t - k_{\mathrm{j}} z)} + c.c. \right]. \tag{1.30}$$

In such nonlinear frequency conversion processes both energy and momentum must be conserved. Energy conservation places a constraint on the output frequency and can be written as:

$$\hbar\omega + \hbar\omega = 2\hbar\omega = \hbar 2\omega, \tag{1.31}$$

meaning that two photons from the fundamental beam at frequency ω (having energy $\hbar\omega$) interact to create one photon at frequency 2ω (having energy $2\hbar\omega$) — hence "energy conservation". The idea of the energy exchange between the three waves in this process is shown in Fig. 1.1.

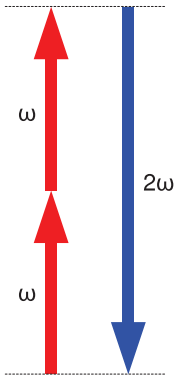

Figure 1.1: The idea of the second harmonic generation process illustrated with an energy diagram. The energy of two photons is combined and exchanged for the energy of a single photon with a doubled optical frequency. To make it possible, a "virtual energy level" is used as a transition stage for this instantaneous three–photon process without leaving any energy in the medium. It is analogous to the real energy states in the medium, for example involved in a laser process.

Momentum conservation means that some other quantities are constrained:

$$\hbar\vec{k} + \hbar\vec{k} = 2\hbar\vec{k} = \hbar 2\vec{k}, \tag{1.32}$$

which describes a relation between photon momenta or, equivalently, wavevectors $\vec{k}$. When we consider the meaning of magnitude of a wavevector, it can be discovered that these conservation rules denote not only to frequencies, but simultaneously to phase velocities of light in the medium:

$$\begin{aligned} 2|\vec{k}|\cos\left(\frac{\alpha}{2}\right) &= |2\vec{k}| \\ 2\frac{n(\omega)\omega}{c}\cos\left(\frac{\alpha}{2}\right) &= \frac{n(2\omega)2\omega}{c} \\ n(\omega)\cos\left(\frac{\alpha}{2}\right) &= n(2\omega), \end{aligned} \tag{1.33}$$

where α is the angle between two fundamental beams (as illustrated in Fig. 1.2) and, in the case of the collinear propagation, the factor $\cos(\alpha/2)$ equals 1. The above formula is the phase–matching condition for the SHG process as it describes the equality of the phase velocities of the three interacting fields. It is clear that this is a very restrictive condition. Even if it is met for a certain frequency, the dispersion ruins the match for other frequencies. If there is no phase–matching, the energy conversion process is not efficient. There are some ways of preparing the medium for broadband phase–matching and those are explained in the subsections 1.2.5 and 1.2.6.

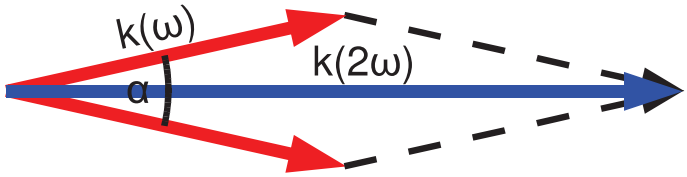

Figure 1.2: The illustration of the wavevector relation in the process of second harmonic generation. The wavevector of second harmonic $\vec{k}(\omega)$ must be equal to the sum of two wavevectors of the interacting fundamental waves $2\vec{k}(\omega)$.

The discussion so far was based on the approximation of a plane waves interaction. The more sophisticated theory of a more realistic SHG process including the Gaussian beam geometry and its experimental validation is described in the article [1.17].

1.2.4 Optical parametric oscillation

One of the other nonlinear phenomena is parametric down–conversion, which occurs when one photon is annihilated and in its place two lower–energetic pho-

tons are created. In a wave description this event corresponds to light at one frequency being converted into two beams having new, lower frequencies. Again, this phenomenon falls into the class of three–wave mixing. This process obeys both energy and momentum conservation laws, so the optical frequencies are related to each other:

$$\begin{aligned} \hbar\omega_P &= \hbar\omega_S + \hbar\omega_I \Rightarrow \\ \omega_P &= \omega_S + \omega_I, \end{aligned} \tag{1.34}$$

where subscripts P, S and I denote, respectively, the traditional descriptions of the waves taking part in this interaction: *pump*, *signal*, and *idler* which are named so in the order of decreasing frequency, as shown schematically in Fig. 1.3.

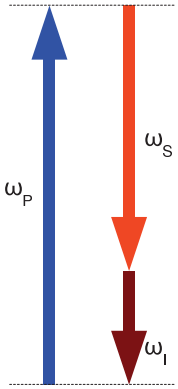

Figure 1.3: The idea of the optical parametric oscillation process. Similarly to second harmonic generation, a virtual energy level is used for an instantaneous energy exchange with the medium. The energy of one photon is split and exchanged for the energy of two lower–energetic photons.

Momentum conservation requires another relation to be fulfilled:

$$\hbar\vec{k}_P = \hbar\vec{k}_S + \hbar\vec{k}_I. \tag{1.35}$$

In the case of a collinear interaction this general, vectorial relation can be further simplified using magnitudes only:

$$\begin{aligned} \hbar\frac{n(\omega_P)\omega_P}{c} &= \hbar\frac{n(\omega_S)\omega_S}{c} + \hbar\frac{n(\omega_I)\omega_I}{c} \Rightarrow \\ n(\omega_P)\omega_P &= n(\omega_S)\omega_S + n(\omega_I)\omega_I, \end{aligned} \tag{1.36}$$

which together with Eq. 1.34 makes it necessary to search for favourable phase–matching conditions. When a suitable medium for performing this process can

be found, a single–pass geometry (formally a situation known as optical parametric generation — OPG) may be used, however it requires extremely high light intensities (usually femtosecond amplifiers). A common way of removing this difficulty is placing the nonlinear crystal in an optical cavity which consists of highly–reflecting mirrors optimised for one of the generated wavelengths — either signal or idler (*signal–* or *idler–resonant* OPO). This way a nanojoule–energy femtosecond oscillator or even a CW laser can be used as a pump. A simple concept of an OPO cavity is presented in Fig. 1.4.

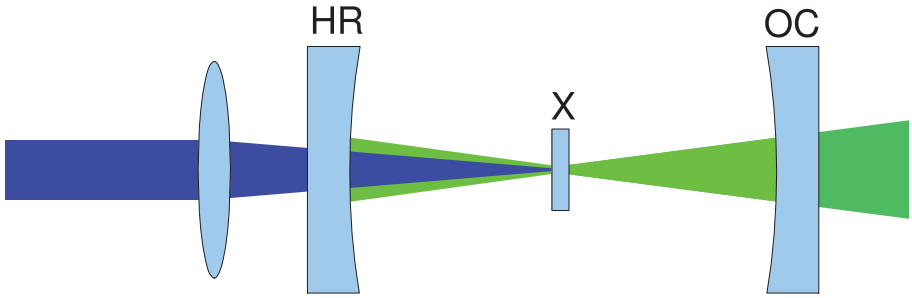

Figure 1.4: The OPO cavity concept. The blue beam is the pump focused into the nonlinear crystal *X* through the mirror *HR*, which is transparent for the pump wavelengths but highly reflective for the longer–wavelength signal, symbolised by the green beam, which oscillate in the cavity. The output coupler *OC* is the partially transparent mirror which transmits the usable portion of the generated signal beam.

The first OPO was built by Giordmaine et al. in 1965 [1.18] and was based on a $LiNbO_3$ crystal pumped by a giant–pulse Nd^{3+}:$CaWO_4$ laser. Later the synchronously pumped OPO idea was proposed by Burneika et al. in 1972 [1.19]. These demonstrations opened fields for creating tunable, broadband sources working in previously unavailable spectral IR regions. Mode–locked dye lasers made it possible to create 100–200 fs pulses [1.20, 1.21, 1.22] tunable in ranges of 750–1040 nm (signal) and 1.5–3.2 µm (idler). Further development came when stable and simple femtosecond Ti:sapphire oscillators became available [1.23, 1.24]. At the same time, new nonlinear materials were appearing, e.g. periodically poled lithium niobate (PPLN), exploiting the quasi–phase–matching principle, described in the subsection 1.2.6. Not relying on birefringence any more, this approach offers arbitrary orientation, making it possible to use the crystal direction associated with highest nonlinearity d and avoid lateral walkoff between pump

and generated wavelengths. It can be phase–matched to a variety of processes and originally was used as an efficient second harmonic generator [1.25, 1.26], but later in OPO construction as well [1.27].

1.2.5 Birefringent phase matching

In the early years of modern nonlinear optics, the birefringence–based idea of realizing phase–matched interactions was found [1.28]. The medium (typically a crystal) needs to be birefringent, so differently polarised beams at the same frequency have different refractive indices. One of the polarisations (the *extraordinary* one) experiences a dependence of its refractive index on the propagation angle with respect to one of the principal optical axes. In the case of SHG, in some crystals a direction of propagation can be found in which the extraordinary ray of second harmonic radiation propagates at the same velocity as the fundamental ordinary ray; then the equality $\vec{k}_2 = 2\vec{k}_1$ is fulfilled and phase–matching is obtained:

$$n_{\mathrm{e}}(2\omega, \theta_{\mathrm{PM}}) = n_{\mathrm{o}}(\omega), \tag{1.37}$$

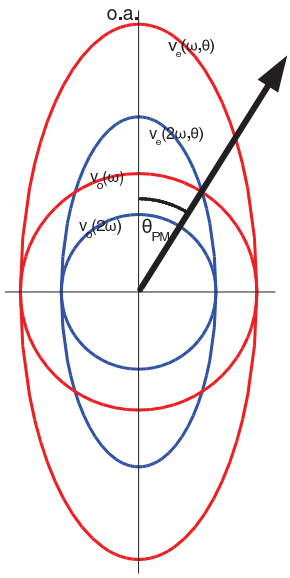

Figure 1.5: The sphere and the ellipsoid of the ordinary and the extraordinary wave phase velocities in a uniaxial birefringent crystal. Due to the dispersion the velocities are different for different frequencies and it may happen that for a certain frequency ω the ordinary ray travels at the same velocity as the extraordinary ray at the doubled frequency 2ω, when propagating at the phase–matching angle θ_{PM}.

where the indices e and o denote to the extraordinary and ordinary waves, respectively, and θ_{PM} is the phase–matching angle. Schematically this situation is shown for a uniaxial birefringent crystal in Fig. 1.5. Propagation along this direction ensures the equality of the phase velocities, however due to the non–collinearity of its Poynting vector and wavevector, the extraordinary wave experiences lateral walkoff, so the overlap between the interacting beams is gradually decreased and the efficiency is reduced. For other nonlinear processes, very commonly birefringent crystals are used for the phase–matching, too.

1.2.6 Quasi–phase matching idea

Birefringent phase–matching is not ideal for several reasons: when it comes to converting broad spectra, in one direction the vectors are matched only for a certain wavelength. Another problem is a complete lack of control of the nonlinearity in crystals; the polarisations and propagation direction that maximise the crystal nonlinearity may not be phase–matchable, forcing the use of a crystal orientation giving phase–matching but with less than optimal efficiency. Another problem is that ordinary and extraordinary waves with collinear $\vec{k}$ vectors do not really propagate collinearly as their Poynting vectors are not collinear; lateral walkoff causes the sliding of the extraordinary beam from the ordinary one, limiting the maximum interaction path.

In a direction which is not exactly phasematched (i.e. $\Delta k \neq 0$), a second harmonic beam is created, but after a short path (of the orders of tens of micrometres) its energy is returned back to the fundamental one. The situation is periodic (see Figure 1.6) as after some characteristic propagation length Λ, dependent on the phase velocities of the waves involved, the situation is again in the starting point thanks to the periodicity of the phases of the electric fields.

In the original paper describing quasi–phasematching [1.10], Armstrong et al. presented the idea of modulating the optical properties of a crystal so that the sign of nonlinearity could be periodically inverted. After a distance of $\Lambda/2$, where the back–conversion begins, the stronger wave should be forced to produce the generated signal with an opposite sign, adding it to the previously generated one rather than subtracting it as it happens in the case of the phase mismatch. One of the ways to ensure this is by the inverting the sign of the nonlinear tensor, d, by

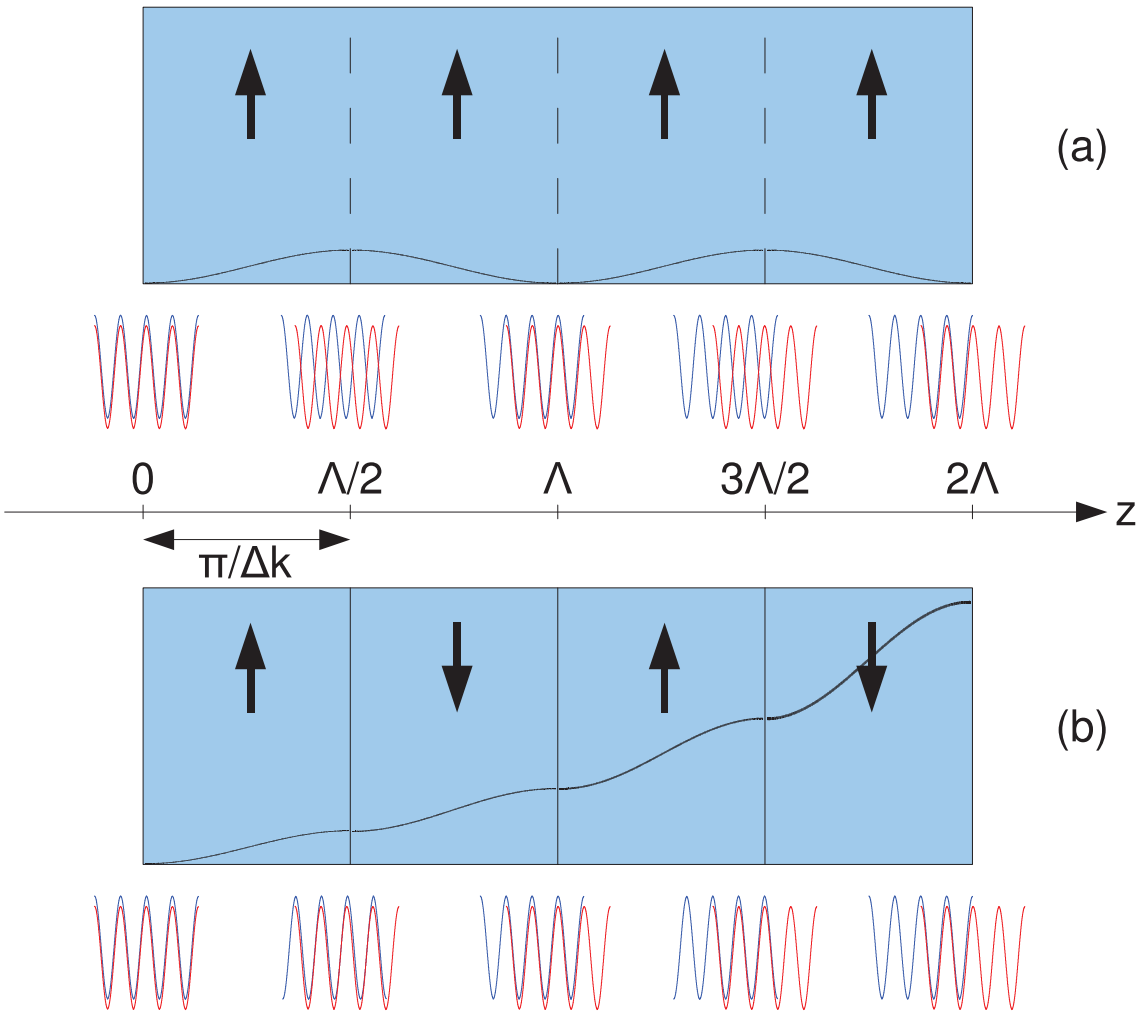

Figure 1.6: The idea of quasi–phase–matching. (a) shows the situation of a phase mismatch in a bulk crystal — after a short propagation path ($\Lambda/2$) the newly generated field has an opposite phase to the newly generated one (equal to the fundamental) which is equivalent to subtracting it from the previously generated one, rather than adding it. The idea shown in part (b) is to change artificially the phase (effectively the sign of d_{ijk}) of the next created portion of the path, after the process becomes un–matched. It may be as simple as inverting the crystal domain orientation. The local intensities of the second harmonic are shown schematically inside the crystals.

changing the physical orientation of the crystal, effectively replacing the P_{NL} by $-P_{\mathrm{NL}}$.

The early techniques used to implement the required inversion were: using stacks of separately oriented plates [1.29, 1.30], alternating a bias voltage while the crystal was grown [1.31, 1.32] or by the careful choice of periodically poled single–crystal fibres [1.33, 1.34]. Nowadays practically the inversion is routinely

done by electrical poling of the crystal with a high voltage after an initial single–domain crystal is grown [1.35, 1.25, 1.26]. The material must be ferroelectric for this purpose, but despite this limitation several suitable media can be found.

If the birefringence is no longer used, the restriction put on the polarisations of all the waves involved is now released and this is the source of a twofold advantage: first, the lateral walkoff can be avoided and second — the direction in the crystal promising the highest nonlinearity d_{ijk} may be chosen.

A very thorough review of the quasi–matching theory and tuning possibilities is presented in [1.36].

1.2.7 Third order effects

When the third order susceptibility $\chi^{(3)}$ is taken into account, new processes involving four waves are introduced. If the $\chi^{(2)}$–related and higher than third–order phenomena are neglected, the polarisation becomes:

$$P = \varepsilon_0 \left(\chi^{(1)} E + \chi^{(3)} E^3 \right), \tag{1.38}$$

and a nonlinear refractive index may be defined:

$$\begin{aligned} P &= \varepsilon_0 \underbrace{\left(\chi^{(1)} + \chi^{(3)} E^2 \right)}_{\chi_{\mathrm{EFF}}} E \\ n_{\mathrm{EFF}} &= \sqrt{1 + \chi_{\mathrm{EFF}}} \approx n_{\mathrm{L}} + \frac{\chi^{(3)}}{2 n_0} E^2. \end{aligned} \tag{1.39}$$

Expressing the field amplitude E as intensity with the relation $I = n_0 c \varepsilon_0 |E|^2 / 2$ gives the formula for the intensity–dependent nonlinear refractive index caused by the third–order polarisation and responsible for the optical Kerr effect:

$$n = n_{\mathrm{L}} + \underbrace{\left(\frac{\chi^{(3)}}{n_0^2 c \varepsilon_0} \right)}_{n_{\mathrm{NL}}} I. \tag{1.40}$$

The existence of this fact manifests itself in spatial and temporal effects. Self–focusing is the spatial effect caused by the nonuniform intensity distribution across the beam. The higher intensity near the beam centre sees a different refractive index than the weaker parts and the wavefronts become distorted. If $n_{\mathrm{NL}} > 0$ (the predominant effect in common materials), phase retardation occurs in the centre of the beam and a focusing effect occurs.

A light pulse can also exhibit a varying temporal intensity: it is stronger in the centre than in the edges. The phase becomes modulated by the $n_{\mathrm{NL}}I$ term (self–phase modulation — SPM), ultimately leading to pulse breakup. New frequencies are created by SPM and can lead to substantial broadening of the pulse spectral bandwidth.

1.2.8 Nonlinear evolution of the pulse shape

The nonlinear evolution of the pulse shape in the medium is described by the nonlinear Schrödinger equation:

$$i\frac{\partial E}{\partial z} = \frac{\beta_2}{2}\frac{\partial^2 E}{\partial t^2} - \gamma|E|^2 E, \tag{1.41}$$

where β_2 is the linear dispersion coefficient (group velocity dispersion per unit length) and γ is the nonlinear coefficient. The term $\gamma|E|^2E$ will create new frequencies.

When the nonlinear term is neglected ($\gamma = 0$), the linear regime is valid and the only phenomenon present is dispersion; the evolution is linear as presented in section 1.1. When the nonlinearity is included ($\gamma \neq 0$), the nonlinear potential–like term results in self–phase modulation which is the process depending on the third power of the field amplitude.

During propagation, the phase accumulated due to the self–phase modulation after propagation over a distance z is:

$$\varphi_{\mathrm{SPM}}(z,t) = \gamma\,|E(0,t)|^2\,z \tag{1.42}$$

and the related frequency chirp becomes:

$$\omega(z,t) = -\frac{\partial\varphi_{\mathrm{SPM}}(z,t)}{\partial t} = -\gamma z\frac{\partial\,|E(0,t)|^2}{\partial t}, \tag{1.43}$$

which corresponds to pulse spectral broadening during propagation.

Stable solutions of the nonlinear Schrödinger equation have the form:

$$E(x,t) = A\frac{1}{\cosh(x)}e^{i\omega t} = A\mathrm{sech}(x)e^{i\omega t}, \tag{1.44}$$

and are referred to as temporal solitons [1.37]. They maintain their pulse shape during propagation due to the balance between dispersion (a compressive effect in a negative dispersion regime) and self–phase modulation. This requires a certain finite pulse energy as the SPM is a function of the electric field amplitude.

If the pulse sees gain in the medium, an additional term in the Schrödinger equation must be included:

$$i\frac{\partial E}{\partial z} = i\frac{g}{2}E + \frac{\beta_2}{2}\frac{\partial^2 E}{\partial t^2} - \gamma|E|^2 E, \tag{1.45}$$

where g is the gain coefficient. Under these conditions stable solutions of this equation still exist but now they have some specific (parabolic) shapes [1.38,1.39]:

$$E(t) = E_0\sqrt{1-\left(\frac{t}{t_0}\right)^2}e^{i\varphi}, \tag{1.46}$$

which possess the very interesting property of a purely linear chirp which is easy to remove after the pulse generation, making them readily compressible.

1.2.9 Materials suitable for nonlinear interactions

The first material used as a nonlinear medium in laser experiments was crystalline quartz (in second harmonic generation [1.3]). Despite its relatively low nonlinearity and lack of phase matching a doubled frequency was recorded.

In the early years of laser science the only material suitable for the birefringently phase–matched nonlinear processes was KDP (KH_2PO_4), but its nonlinearity was not very impressive [1.40]. Later on new materials were identified and now several notable families are available.

Lithium compounds, $LiNbO_3$, $LiIO_3$ and $LiTaO_3$ are very common choice for periodic poling or electro–optic modulators due to their ferroelectricity and high nonlinearity for extraordinary rays [1.41]. They suffer from photorefractive damage and to prevent this are commonly heated to ~100°C, but currently MgO doping is a very popular modification, which decreases this unwanted effect without the need for heating.

Another group suitable for periodic poling is titanyl phosphates and arsenates [1.42]: KTP ($KTiOPO_4$), KTA ($KTiOAsO_4$) and RTA ($RbTiAsPO_4$). Arsenates have extended mid–IR transmission in comparison with the phosphates.

Various borates are available: BBO (β–BaB_2O_4), LBO (LiB_3O_4), BIBO (BiB_3O_6) and many more [1.43, 1.44, 1.45]. They have quite a high nonlinearity and are phase–matchable through birefringence in a broad range of frequencies, working very well in noncollinear parametric amplifiers or as frequency doublers.

A very high nonlinearity and a wide mid–IR tranparency range make ZGP ($ZnGeP_2$) material suitable for OPO construction and doubling of CO_2 laser frequency [1.46].

For the construction of a quasi–phase matched device a standard choice now is MgO:PPLN (MgO–doped periodically poled $LiNbO_3$), which is widely available commercially and can be grown to lengths of almost 10 cm with a high optical quality. The growth and poling technology is very well established, and still improving, so recently thicker crystals became available offering apertures greater than the previous limit of 0.5 mm. Typically several poled patterns are incorporated beside each other into one crystal, so it may act as a frequency converter easily switchable between several phase–matching conditions by translating the crystal relative to the input beam. These crystals are manufactured for the normal incidence of the beam and are orientated so all the interacting beams are extraordinary waves, exploiting the highest nonlinear coefficient available for this crystal. Anti–reflective coatings are applied to end surfaces.

1.3 Femtosecond pulse measurement

In many ultrafast optics–related experiments it is very important to know the shape and exact length of laser pulses used. As no electronic devices can process the information quick enough to show the envelope of femtosecond pulses, physicists decided to use intrinsic properties of the intense light to develop optical methods of ultrashort pulses measurement. All current methods of pulse characterisation on the femtosecond timescale rely on nonlinear optical phenomena – the general fact that we can see effects whose strength is modulated by the presence of light's electric field in the medium.

Two widely used complete ways of characterising femtosecond pulses are frequency–resolved optical gating (FROG) [1.47] and spectral phase interferometry for direct electric–field reconstruction (SPIDER) [1.48]. A simpler alternative is the autocorrelation measurement, however at a cost of losing some information.

1.3.1 Autocorrelation functions

The temporal autocorrelation is the simplest tool for obtaining an estimate of pulse durations. It also allows easy characterisation and control of pulse durations in a system as the width of the autocorrelation function scales with the pulse duration, and the residual chirp at the point of the measurement can be easily minimised if there is a compression line in the system.

The autocorrelation function is the correlation of the electric field with itself [1.49]:

$$g_2(\tau) = \frac{\int_{-\infty}^{+\infty} \left|[E(t) + E(t-\tau)]^2\right|^2 dt}{2\int_{-\infty}^{+\infty} \left|[E(t)]^2\right|^2 dt} \tag{1.47}$$

and requires two identical pulse replicas with a variable delay τ between them. The common experimental arrangement is a Michelson interferometer with one arm of a variable length (Fig.1.7). Experimentally it is the second–order autocorrelation function which must be recorded so a nonlinear effect ($\sim E^2$) in a crystal

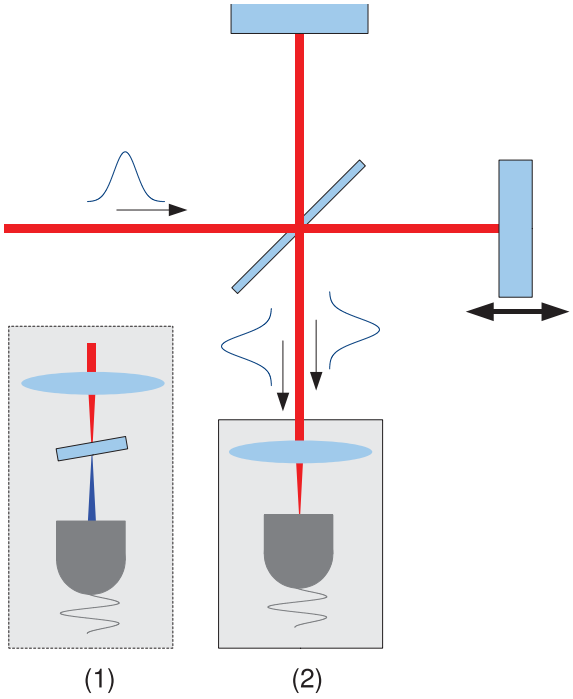

Figure 1.7: The setup for the measurement of the autocorrelation function. Scanning the arm of the Michelson interferometer gives the variable delay. The second–order signal is either detected by a two–photon photodiode (2) or by the single–photon photodiode and the second harmonic generated in a nonlinear crystal (1).

is necessary or a two–photon absorption in a photodiode. An ideal "interferometric" autocorrelation function of a Gaussian pulse without chirp is shown with the blue line in Fig. 1.8.

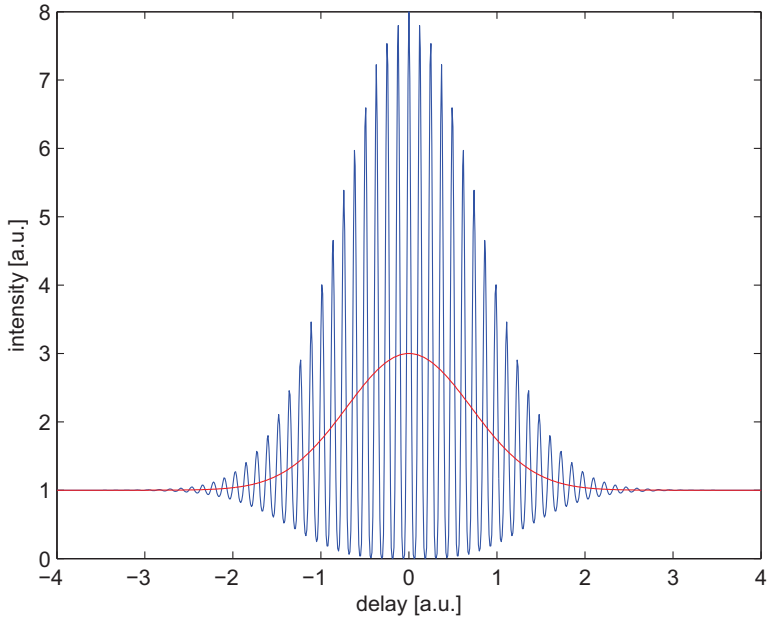

Figure 1.8: The second order functions of autocorrelation of an unchirped Gaussian pulse. The blue line — the interferometric function. The red line — the intensity profile for a measurement without sufficient bandwidth.

It is not always possible to resolve the fringes in the autocorrelation function. When the detection device is too slow to do this, the averaged result is the intensity autocorrelation (the red line in Fig. 1.8):

$$S(\tau) = 1 + \frac{2\int_{-\infty}^{+\infty} I(t)I(t-\tau)dt}{\int_{-\infty}^{+\infty} I^2 dt} \tag{1.48}$$

It is not possible to determine the pulse duration exactly from the autocorrelation function unless the pulse shape is known. The autocorrelation FWHM is proportional to the pulse FWHM but the proportionality factor is pulse–shape dependent, so it is necessary to assume one of the standard shapes. For the Gaussian pulse it is $\sqrt{2}$ and for the sech^2(t) it is 1.543.

1.3.2 Frequency–Resolved Optical Gating (FROG)

A technique allowing for the complete pulse characterisation is frequency–resolved optical gating. The apparatus required is very similar to the one employed in the autocorrelation measurement with the nonlinear crystal (Fig. 1.7 (1)), however the optical nonlinear signal is subsequently spectrally resolved, i.e. for each delay the spectrum must be measured instead of only intensity. This gives a matrix of points which is then processed by an iterative phase–retrieval algorithm. The algorithm processing time can be a major problem in this method, however sub-Hz rates of the pulse shape retrieval were presented [1.50, 1.51] at the expense of a complicated setup. In a standard application the FROG trace is captured and then the pulse is retrieved using a separate program.

Many nonlinear processes can be used as sources for the FROG trace: second harmonic generation [1.52], third harmonic generation [1.53], self–diffraction [1.47] and polarisation gating [1.54] are typical. The second harmonic–based version is the most sensitive due to the second–order nonlinearity but suffers from the ambiguity of time–reversal due to the inherent symmetry of the trace. The functional dependencies of the FROG trace from the measured pulse field are as follows:

$$\begin{aligned}
&\textbf{second harmonic} && S^{\mathrm{SHG}}_{\mathrm{FROG}}(\omega,\tau) = \left|\int_{-\infty}^{+\infty} E(t)E(t-\tau)e^{-i\omega t}dt\right|^2 \\
&\textbf{third harmonic} && S^{\mathrm{THG}}_{\mathrm{FROG}}(\omega,\tau) = \left|\int_{-\infty}^{+\infty} E(t)E^2(t-\tau)e^{-i\omega t}dt\right|^2 \\
&\textbf{self–diffraction} && S^{\mathrm{SD}}_{\mathrm{FROG}}(\omega,\tau) = \left|\int_{-\infty}^{+\infty} E^2(t)E^*(t-\tau)e^{-i\omega t}dt\right|^2, \\
&\textbf{polarisation–gating} && S^{\mathrm{PG}}_{\mathrm{FROG}}(\omega,\tau) = \left|\int_{-\infty}^{+\infty} E(t)\,|E(t-\tau)|^2\,e^{-i\omega t}dt\right|^2.
\end{aligned} \tag{1.49}$$

The retrieval algorithm is iterative. There are several slightly different approaches, but in the programs I have used later in this thesis the principal component generalised projections method was employed [1.55]. It is quite straightforward and is based on some fundamental algebraic observations. After guessing the initial probe and gate vectors P and G, respectively, the computations necessary to perform in each iteration step are the following:

1. Calculate the FROG trace from the vectors P and G according to the equation suitable for the experimental method used, thus applying the *nonlinear constraint*. For the SHG–FROG it means:

- take the outer product of the probe and gate which are essentially the same pulse in this case, so $O = P^T G + G^T P$,
- find the time–domain representation of the FROG trace by shifting each row of the O matrix by its number decreased by 1, this way introducing the delay,
- Fourier–transform each column of O from time to frequency, yielding the matrix $O(\tau, \omega)$,
- the new FROG trace is $|O|^2$, however O is more convenient for further calculations.

2. After determining the new FROG trace, apply the *experimental constraint*, replacing the amplitude of the calculated trace with the measured one: $O = \sqrt{S_{\mathrm{FROG}}} \cdot \exp(i \angle O)$.

3. Return to the outer product form by inverse Fourier transformation column–wise and removing the delay by shifting each row by its number decreased by 1 in the opposite direction to the one applied in step 1.

4. Perform SVD decomposition into matrices $U \times W \times V^T$, where columns of U are candidate probe vectors, rows of V are candidate gate vectors and diagonal elements of W are their relative weights in contributing to the formation of O.

5. Find the biggest weight W_{ii} (the *principal component*) and the corresponding pair of E_i and G_i which are this iteration's results.

6. Find the RMS error for this iteration, defined as:

$$\delta = \sqrt{\frac{1}{N^2} \sum_{i=1}^{N} \sum_{j=1}^{N} \left[S_{\mathrm{FROG}}(\omega_i, \tau_j) - |O(\omega_i, \tau_j)|^2 \right]^2}. \tag{1.50}$$

This algorithm, implemented on a modern computer, depending on the grid size, typically runs at the speed of 0.1–10 iterations per second and for not very exotic pulses converges after several tens of iterations. Once the error is below the target threshold value, the current E vector is accepted as the pulse electric field in time $E(t)$. Generally, the algorithm will not converge if the measurement was not performed properly, so the fact of convergence is a test for the quality

of the experimental data. Subsequently a check is routinely performed to assess the quality of the retrieval itself — the Fourier transform of $E(t)$ is found and its intensity $|E(\omega)|^2$ compared to the measured spectrum, ending the procedure.

1.3.3 Cross–Correlation Frequency–Resolved Optical Gating

As was mentioned previously, the probe and gate pulses do not need to be identical. In fact there exists a version of the FROG technique which makes it possible to obtain the full amplitude and phase information about two unknown different pulses simultaneously if both interact nonlinearly in a crystal. Commonly this method is referred to as XFROG [1.56, 1.55]. This approach removes the time–reversal ambiguity:

$$S_{\mathrm{XFROG}}(\omega,\tau) = \left| \int_{-\infty}^{+\infty} E_1(t) E_2(t-\tau) e^{-i\omega t} dt \right|^2 , \tag{1.51}$$

because E_1 and E_2 cannot be freely swapped without changing the shape of the measured trace.

Sum–frequency mixing or difference–frequency mixing (modifying E_2 into E_2^*) can be used as the nonlinear process, thus increasing the flexibility of the choice of the spectral region for detecting the XFROG signal.

The principal reason for the use of this variant is the fact that the time–ambiguity is automatically removed from the retrieval process. Moreover, if two different unknown pulses are present in the experiment simultaneously, it is possible to measure them simultaneously, using one data set and still with a high reliability.

1.3.4 Spectral Phase Interferometry for Direct Electric–field Reconstruction (SPIDER)

The other, competitive technique of measuring the phase of ultrashort pulses, is SPIDER [1.48]. It relies on the fact that two pulses interfering on the spectrometer's detector produce a trace which contains information about the difference of their phases, if only some conditions are initially fulfilled.

For the full phase information to be extracted from the interference spectrum of the pulse with itself, twofold preparation is needed: the delay τ between pulse and its replica must be introduced, and, much more demanding requirement, a

spectral shear Ω must be added to one of the pulses. Then the measured interference trace is:

$$S(\omega) = I(\omega) + I(\omega + \Omega) + 2\sqrt{I(\omega)}\sqrt{I(\omega + \Omega)}\cos[\varphi(\omega) - \varphi(\omega + \Omega) + \omega\tau]. \quad (1.52)$$

The Fourier transform of this spectrum reveals three components: a constant term S_{DC}; a negative–frequency component S_-; and a positive–frequency component S_+, whose phase is equal to:

$$\angle(S_+) = \varphi(\omega) - \varphi(\omega + \Omega) + \omega\tau. \quad (1.53)$$

Now, the $\omega\tau$ part must be subtracted and then the phase difference $\varphi(\omega) - \varphi(\omega + \Omega)$ is available for concatenation, or numerical integration.

The procedure is not iterative, which is the great advantage of this method, however the relatively small amount of data needed makes it quite vulnerable to hidden experimental errors which do not demonstrate themselves so readily as in FROG. Another serious problem is the presence of two experimental constants τ and Ω, which must be known with a high accuracy. The spectral shear is quite demanding as each spectrum must be measured separately to find Ω and the delay needs to be extracted from the separate interferogram. Both quantities may be calculated based on the knowledge of the experimental details, but any error in τ raises an error in a form of linear factor in the phase difference, so as a result a false quadratic component in φ may be added to the result. An error in finding Ω introduces a shift in the data and an error in the linear phase component.

The standard experimental setup for the measurement of femtosecond pulses with the SPIDER technique consists of several sections and is quite complicated. First, the pulse is split and one part is substantially stretched, in a glass block for example. Then the other part is split again into two copies with a certain delay between them. Subsequently these two copies are mixed in a nonlinear crystal with two different (due to the delay) quasi–monochromatic portions of the stretched pulse so that the pulses being the result of this process are spectrally sheared. The final step is the measurement of the spectrum of these two up–converted pulses. The idea is based on the fact that the phase of the original pulse should be preserved in the nonlinear mixing process. The SPIDER method was not used in the work described in this thesis and so will not be discussed further.

1.4 Outline

In my thesis work I used periodically–poled lithium niobate nonlinear crystals to build sources of ultrashort pulses. The performance of the sources was characterised and possible applications tested or suggested.

In Chapter 2 the construction of an optical parametric oscillator tunable in the region of 3.3 μm is described. Combined with a novel photonic bandgap fibre guiding at these wavelengths, it was applied to methane sensing.

Chapter 3 contains the description of the construction of a long–cavity, high–energy optical parametric oscillator tunable around 1500 nm. The device was designed for the material processing, especially waveguide writing in silicon.

Finally, Chapter 4 refers a novel femtosecond pulse shaping system. It is based on a grating–engineered quasi–phasematched crystal which was designed for creating various target pulses by means of an engineered second harmonic generation process.

1.5 References

[1.1] A. L. Schawlow and C. H. Townes, "Infrared and optical masers", *Physical Review* **112** (6), p. 1940–1949, 1958.

[1.2] T. H. Maiman, "Stimulated optical radiation in ruby", *Nature* **187** (4736), p. 493–494, 1960.

[1.3] P. A. Franken, A. E. Hill, C. W. Peters and G. Weinreich, "Generation of optical harmonics", *Physical Review Letters* **7** (4), p. 118–119, 1961.

[1.4] M. Bass, P. A. Franken, A. E. Hill, C. W. Peters and G. Weinreich, "Optical mixing", *Physical Review Letters* **8** (1), p. 18, 1962.

[1.5] M. Bass, P. A. Franken, J. F. Ward and G. Weinreich, "Optical rectification", *Physical Review Letters* **9** (11), p. 446–448, 1962.

[1.6] D. E. Spence, P. N. Kean and W. Sibbett, "60–fsec pulse generation from a self–mode–locked Ti:sapphire laser", *Optics Letters* **16** (1), p. 42–44, 1991.

[1.7] R. R. Alfano and S. L. Shapiro, "Observation of self–phase modulation and small–scale filaments in crystals and glasses", *Physical Review Letters* **24** (11), p. 592–594, 1970.

[1.8] C. Lin and R. H. Stolen, "New nanosecond continuum for excited–state spectroscopy", *Applied Physics Letters* **28** (4), p. 216–218, 1976.

[1.9] J. K. Ranka, R. S. Windeler and A. J. Stentz, "Visible continuum generation in air–silica microstructure optical fibers with anomalous dispersion at 800 nm", *Optics Letters* **25** (1), p. 25–27, 2000.

[1.10] J. A. Armstrong, N. Bloembergen, J. Ducuing and P. S. Pershan, "Interactions between light waves in a nonlinear dielectric", *Physical Review* **127** (6), p. 1918–1939, 1962.

[1.11] P. A. Franken and J. F. Ward, "Optical harmonics and nonlinear phenomena", *Reviews of Modern Physics* **35** (1), p. 23–39, 1963.

[1.12] D. T. Reid, "Engineered quasi–phase–matching for second–harmonic generation", *Journal of Optics A* **5** (4), p. S97–S102, 2003.

[1.13] U. K. Sapaev and D. T. Reid, "General second–harmonic pulse shaping in grating–engineered quasi–phase–matched nonlinear crystals", *Optics Express* **13** (9), p. 3264–3276, 2005.

[1.14] A. Yariv, *Quantum electronics*, John Wiley & Sons, 3rd ed., 1988.

[1.15] R. W. Boyd, *Nonlinear optics*, Academic Press, Inc., San Diego, 1992.

[1.16] J. C. Maxwell, *A treatise on electricity and magnetism*, Clarendon Press Series, Clarendon Press, Oxford, 1873.

[1.17] D. A. Kleinman, A. Ashkin and G. D. Boyd, "Second–harmonic generation of light by focused laser beams", *Physical Review* **145** (1), p. 338–379, 1966.

[1.18] J. A. Giordmaine and R. C. Miller, "Tunable coherent parametric oscillation in $LiNbO_3$ at optical frequencies", *Physical Review Letters* **14** (24), p. 973–976, 1965.

[1.19] K. Burneika, M. Ignatavičius, V. Kabelka, A. Piskarskas and A. Stabinis, "Parametric light amplification and oscillation in KDP with mode–locked pump", *IEEE Journal of Quantum Electronics* **QE–8**, p. 574, 1972.

[1.20] D. C. Edelstein, E. S. Wachman and C. L. Tang, "Broadly tunable high repetition rate femtosecond optical parametric oscillator", *Applied Physics Letters* **54** (18), p. 1728–1730, 1989.

[1.21] E. S. Wachman, W. S. Pelouch and C. L. Tang, "cw femtosecond pulses tunable in the near– and midinfrared", *Journal of Applied Physics* **70** (3), p. 1893–1895, 1991.

[1.22] E. S. Wachman, D. C. Edelstein and C. L. Tang, "Continuous–wave mode–locked and dispersion–compensated femtosecond optical parametric oscillator", *Optics Letters* **15** (2), p. 136–138, 1990.

[1.23] W. S. Pelouch, P. E. Powers and C. L. Tang, "Ti:sapphire–pumped, high–repetition–rate femtosecond optical parametric oscillator", *Optics Letters* **17** (15), p. 1070–1072, 1992.

[1.24] Q. Fu, G. Mak and H. M. van Driel, "High–power, 62–fs infrared optical parametric oscillator synchronously pumped by a 76–MHz Ti:sapphire laser", *Optics Letters* **17** (14), p. 1006–1008, 1992.

[1.25] M. Yamada, N. Nada, M. Saitoh and K. Watanabe, "First–order quasi–phase matched $LiNbO_3$ waveguide periodically poled by applying an external field for efficient blue second–harmonic generation", *Applied Physics Letters* **62** (5), p. 435–436, 1993.

[1.26] W. K. Burns, W. McElhanon and L. Goldberg, "Second harmonic generation in field poled, quasi–phase–matched, bulk $LiNbO_3$", *IEEE Photonic Technology Letters* **6** (2), p. 252–254, 1994.

[1.27] L. E. Myers, R. C. Eckardt, M. M. Fejer, R. L. Byer, W. R. Bosenberg and J. W. Pierce, "Quasi–phase–matched optical parametric oscillators in bulk periodically poled $LiNbO_3$", *Journal of the Optical Society of America B* **12** (11), p. 2102–2116, 1995.

[1.28] J. A. Giordmaine, "Mixing of light beams in crystals", *Physical Review Letters* **8** (1), p. 19–20, 1962.

[1.29] J. D. McMullen, "Optical parametric interactions in isotropic materials using a phase–corrected stack of nonlinear dielectric plates", *Journal of Applied Physics* **46** (7), p. 3076–3081, 1975.

[1.30] A. Szilagyi, A. Hordvik and H. Schlossberg, "A quasi–phase–matching technique for efficient optical mixing and frequency doubling", *Journal of Applied Physics* **47** (5), p. 2025–2032, 1976.

[1.31] D. Feng, N. B. Ming, J. F. Hong, Y. S. Yang, J. S. Zhu, Z. Yang and Y. N. Wang, "Enhancement of second–harmonic generation in $LiNbO_3$ crystals with periodic laminar ferroelectric domains", *Applied Physics Letters* **37** (7), p. 607–608, 1980.

[1.32] A. Feisst and P. Koidl, "Current induced periodic ferroelectric domain structures in $LiNbO_3$ applied for efficient nonlinear optical frequency mixing", *Applied Physics Letters* **47** (11), p. 1125–1126, 1985.

[1.33] Y. S. Luh, R. S. Feigelson, M. M. Fejer and R. L. Byer, "Ferroelectric domain structures in $LiNbO_3$ single–crystal fibers", *Journal of Crystal Growth* **78** (1), p. 135–143, 1986.

[1.34] Y. S. Luh, M. M. Fejer, R. L. Byer and R. S. Feigelson, "Stoichiometric $LiNbO_3$ single–crystal fibers for nonlinear optical applications", *Journal of Crystal Growth* **85** (1–2), p. 264–269, 1987.

[1.35] E. J. Lim, M. M. Fejer and R. L. Byer, "Second–harmonic generation of green light in periodically poled planar lithium niobate waveguide", *Electronics Letters* **25** (3), p. 174–175, 1989.

[1.36] M. M. Fejer, G. A. Magel, D. H. Jundt and R. L. Byer, "Quasi–phase–matched second harmonic generation: Tuning and tolerances", *IEEE Journal of Quantum Electronics* **28** (11), p. 2631–2654, 1992.

[1.37] L. F. Mollenauer, R. H. Stolen and J. P. Gordon, "Experimental observation of picosecond pulse narrowing and solitons in optical fibers", *Physical Review Letters* **45** (13), p. 1095–1098, 1980.

[1.38] D. Anderson, M. Desaix, M. Karlsson, M. Lisak and M. L. Quiroga-Teixeiro, "Wave–breaking–free pulses in nonlinear–optical fibers", *Journal of the Optical Society of America B* **10** (7), p. 1185–1190, 1993.

[1.39] M. E. Fermann, V. I. Kruglov, B. C. Thomsen, J. M. Dudley and J. D. Harvey, "Self–similar propagation and amplification of parabolic pulses in optical fibers", *Physical Review Letters* **84** (26), p. 6010–6013, 2000.

[1.40] R. Craxton, S. Jacobs, J. Rizzo and R. Boni, "Basic properties of KDP related to the frequency conversion of 1 μm laser radiation", *IEEE Journal of Quantum Electronics* **17** (9), p. 1782–1786, 1981.

[1.41] R. C. Eckardt, H. Masuda, Y. X. Fan and R. L. Byer, "Absolute and relative nonlinear optical coefficients of KDP, KD^*P, BaB_2O_4, $LiIO_3$, MgO:$LiNbO_3$, and KTP measured by phase–matched second–harmonic generation", *IEEE Journal of Quantum Electronics* **26** (5), p. 922–933, 1990.

[1.42] J. D. Bierlein and H. Vanherzeele, "Potassium titanyl phosphate: properties and new applications", *Journal of the Optical Society of America B* **6** (4), p. 622–633, 1989.

[1.43] D. N. Nikogosyan, "Lithium triborate (LBO)", *Applied Physics A* **58** (3), p. 181–190, 1994.

[1.44] D. N. Nikogosyan, "Beta barium borate (BBO)", *Applied Physics A* **52** (6), p. 359–368, 1991.

[1.45] M. Ghotbi and M. Ebrahim-Zadeh, "Optical second harmonic generation properties of BiB_3O_6", *Optics Express* **12** (24), p. 6001–6019, 2004.

[1.46] S. Das, G. C. Bhar, S. Gangopadhyay and C. Ghosh, "Linear and nonlinear optical properties of $zngep_2$ crystal for infrared laser device applications: revisited", *Applied Optics* **42** (21), p. 4335–4340, 2003.

[1.47] D. J. Kane and R. Trebino, "Characterization of arbitrary femtosecond pulses using frequency–resolved optical gating", *IEEE Journal of Quantum Electronics* **29** (2), p. 571–579, 1993.

[1.48] C. Iaconis and I. A. Walmsley, "Self–referencing spectral interferometry for measuring ultrashort optical pulses", *IEEE Journal of Quantum Electronics* **35** (4), p. 501–509, 1999.

[1.49] J. C. M. Diels, J. J. Fontaine, I. C. McMichael and F. Simoni, "Control and measurement of ultrashort pulse shapes (in amplitude and phase) with femtosecond accuracy", *Applied Optics* **24** (9), p. 1270–1282, 1985.

[1.50] J. Garduño–Mejía, E. Ramsay, A. Greenaway and D. T. Reid, "Real time femtosecond optical pulse measurement using a video–rate frequency–resolved optical gating system", *Review of Scientific Instruments* **74** (8), p. 3624–3627, 2003.

[1.51] D. J. Kane, J. Weston and K. J. Chu, "Real–time inversion of polarization gate frequency-resolved optical gating spectrograms", *Applied Optics* **42** (6), p. 1140–1144, 2003.

[1.52] K. W. DeLong, R. Trebino, J. Hunter and W. E. White, "Frequency–resolved optical gating with the use of second–harmonic generation", *Journal of the Optical Society of America B* **11** (11), p. 2206–2215, 1994.

[1.53] T. Tsang, M. A. Krumbügel, K. W. DeLong, D. N. Fittinghoff and R. Trebino, "Frequency–resolved optical–gating measurements of ultrashort pulses using surface third–harmonic generation", *Optics Letters* **21** (17), p. 1381–1383, 1996.

[1.54] D. J. Kane and R. Trebino, "Single–shot measurement of the intensity and phase of an arbitrary ultrashort pulse by using frequency–resolved optical gating", *Optics Letters* **18** (10), p. 823–825, 1993.

[1.55] D. J. Kane, G. Rodriguez, A. J. Taylor and T. S. Clement, "Simultaneous measurement of two ultrashort laser pulses from a single spectrogram in a single shot", *Journal of the Optical Society of America B* **14** (4), p. 935–943, 1997.

[1.56] K. W. DeLong, R. Trebino and W. E. White, "Simultaneous recovery of two ultrashort laser pulses from a single spectrogram", *Journal of the Optical Society of America B* **12** (12), p. 2463–2466, 1995.

Chapter 2

Methane detection using an optical parametric oscillator and photonic bandgap fibre

2.1 Motivation and background — methane sensing

Methane (CH_4) is a gas commonly present in many industrial environments and, as a component of natural gas, in domestic installations. It is not toxic but can be dangerous when the concentration level in air exceeds 5% — then it may explode. Also methane displaces oxygen from inadequately ventilated areas and causes a risk of asphyxia. It is colourless and odourless so detection must be performed with indirect physical means. The known physical effects which can be used to build a practical sensing device are: surface conductivity variations of semiconductor oxides caused by exposure to changing atmospheres and infrared (IR) light absorption by methane molecular vibrations.

Use of semiconductor oxides is not very convenient as they require high working temperatures (e.g. 800°C in tin dioxide [2.1] or 250°C in zinc dioxide [2.2]) and complicated, not well explored additions of other materials (e.g. zeolitic films [2.3]), to be selective and to prevent long–term drift. Moreover, the minimal time response reported is of the order of tens of seconds. Quick, sensitive and non–degradable semiconductor oxides–based methane detectors are still the subject of active development.

Optical detection schemes may additionally benefit from incorporating them into fibre–based apparatus. Fibre can be used to deliver a beam into remote environments (possibly hazardous or not accessible otherwise) or to enhance detection efficiency if the entire length of the fibre is made sensitive, while still the size and weight of the device remain relatively small. Other advantages are: electromagnetic immunity — any ambient electronic noise does not contribute to optical signal propagating in the core; no need for electric power in the place of detection, so removing a risk of ignition; a capability for multiplexing, so one fibre can carry information gathered using different wavelengths [2.4].

A separate class of sensing applications emerged with the invention of photonic crystal fibres [2.5]. Their characteristics and some working examples will be briefly discussed in the Section 2.7. This particular technique was a vital part of my experiment, in which I demonstrated an optical detection of methane present in the core of a hollow fibre.

2.2 The origin of methane IR absorption spectra

Practically the only type of commercially available and reliable methane detectors are those exploiting IR absorption measurement. This technique relies on the existence of a so–called *molecular "fingerprint" region*, which is a range of wavelengths including sets of spectral lines uniquely identifying certain molecules or characteristic parts of bigger molecules.

The origin of these absorption spectra can be explained on the grounds of quantum mechanical description of molecular movements (see [2.6, 2.7]). The crucial quantity governing the overall molecule ability to interact with the electric field of light is a vector called the *electric dipole moment* of molecule, defined for a pair of electric charges q and $-q$ separated by a distance R as:

$$\vec{\mu} = q\vec{R}, \tag{2.1}$$

and directed from the negative charge to the positive. Generally, for every molecule whose internal charge is spread in space in a complicated way, a dipole moment can be determined and is a measure of the relative displacement of centres of total negative and positive charges in the molecule.

A molecule will absorb a portion of energy from a light beam if this energy is equal to the difference of energies between one of the available higher levels and the current level. There is one absolutely necessary condition to be fulfilled for an interaction between the beam's electric field and the molecule to happen: only those molecular movements during which a change of dipole moment occurs will be induced by the absorption of light. Otherwise there is no "handle" for the oscillating field to use in order to start this movement.

2.2.1 Rotations

The simplest activity which a molecule can be forced to perform is a rotation. The energy associated with molecular rotation is relatively small and frequencies for which pure rotation spectra are observed lie in the microwave range (tens to hundreds of GHz, wavelengths of the order of cm).

To a stationary observer, a change in dipole moment can occur in a rotating molecule only if it already has its own permanent dipole moment (as shown in Fig. 2.1). This means that homonuclear diatomic molecules (like H_2), symmetrical linear molecules (like CO_2) and molecules having all three moments of inertia equal (spherical rotors, like CH_4) can rotate, but this rotation cannot be induced by absorption of optical radiation.

In order to find energies of rotations in the molecule, we can use a simple classical model, in which

$$E_{\mathrm{ROT}} = \frac{1}{2} I \omega^2, \tag{2.2}$$

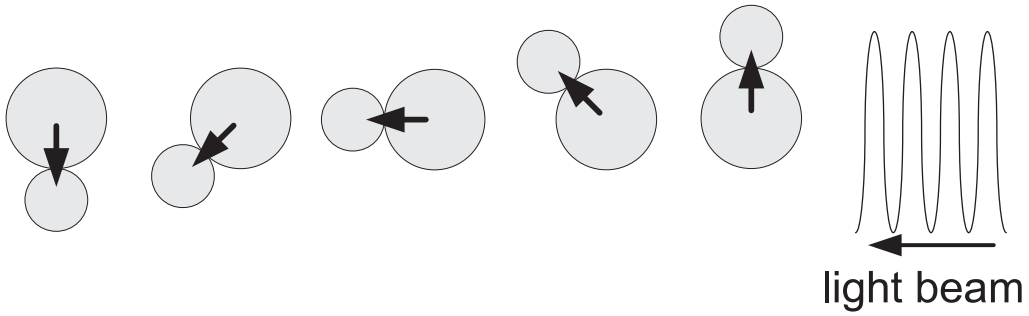

Figure 2.1: The electric dipole oscillation during rotation of the molecule. Stationary observer sees alternating projection of the dipole vector to the axis parallel to the electric field of the light beam, however the vector magnitude remains fixed.

where I is the moment of inertia and ω is the angular velocity. For the methane molecule, shown in Fig. 2.2, which is a spherical rotor, there is only one value of $I = \frac{8}{3} m_{\mathrm{H}} R^2$, where m_{H} is the mass of the hydrogen atom.

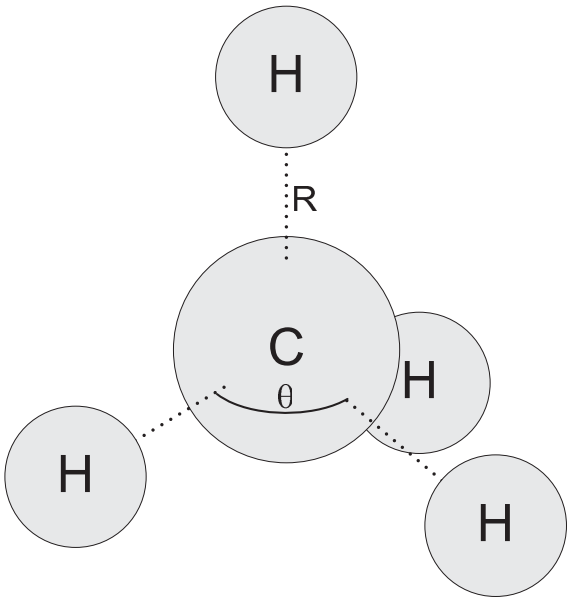

Figure 2.2: The tetrahedral structure of the methane molecule. The central carbon atom is surrounded by four hydrogen atoms. R is the length of the molecular bond (distance between C and H atoms) equal to 77 pm and θ is the angle between bonds equal to 109°28′.

The magnitude of the angular momentum is:

$$|\vec{J}| = I\omega, \tag{2.3}$$

so energy can be rewritten as:

$$E_{\mathrm{ROT}} = \frac{J^2}{2I}. \tag{2.4}$$

According to the rules of quantization, in the expression for the rotational energy of the molecule, J^2 must be replaced by $J(J+1)\hbar^2$, so energy becomes:

$$E_{\mathrm{J}} = \frac{\hbar^2}{2I} J(J+1), \tag{2.5}$$

and J is a number of the rotational state, $J = 0, 1, 2, \ldots$ The energy acquired by the molecule during the absorption of one photon is then equal to:

$$\begin{aligned} E_{\mathrm{J}+1} - E_{\mathrm{J}} &= \frac{\hbar^2}{I}(J+1) \\ B &\triangleq \frac{\hbar^2}{2I} \\ \Delta E &= 2B(J+1), \end{aligned} \tag{2.6}$$

and simultaneously is equal to the energy of the photon. The distances between the rotational energy levels are increasing with increasing J and the result is the equally spaced series of transition spectral lines, as shown in Fig. 2.3.

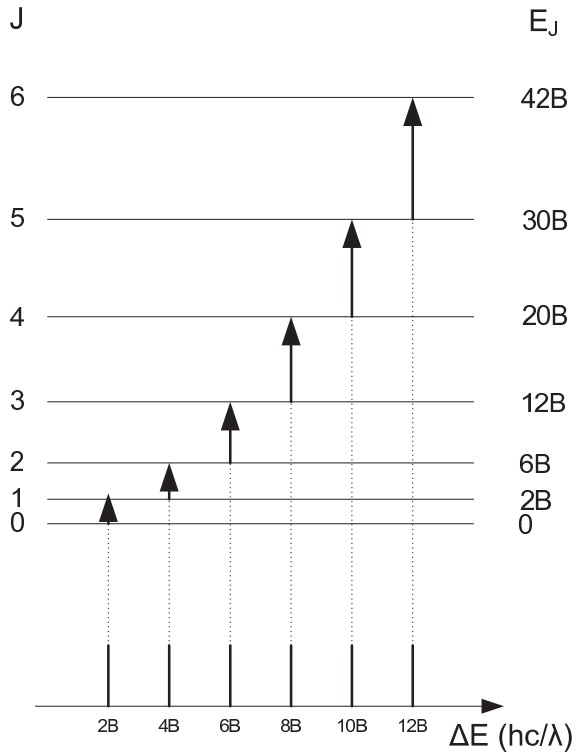

Figure 2.3: The schematic of the origin of the rotation absorption lines in the molecule. Increasing energy differences between adjacent levels are the source of equally spaced spectral lines.

2.2.2 Oscillations

The next, more complicated mode of movement for a molecule is a vibration around its equilibrium shape. There are two types of possible vibrations — the molecule can either stretch or bend its bonds. Schematic examples of these different modes for a relatively simple CO_2 molecule are shown in Fig. 2.4. The energies associated with the oscillation are higher than those in the case of rotations and the vibrational transitions may be observed as an absorption of light in the IR region (wavelengths of the order of μm). One group of molecules cannot be forced to vibrate by optical absorption due to the lack of the "handle", as there is no change of dipole moment during the transition — these are homonuclear diatomic molecules, like N_2. These oscillations are called *optically inactive*. How-

ever, not all vibrations in even more complex molecules are optically active. If there is no change of the dipole moment during the transition from the ground state, there is no absorption of light, too, as it is in the case of the symmetric stretching CO_2 mode of oscillation shown in Fig. 2.4(a).

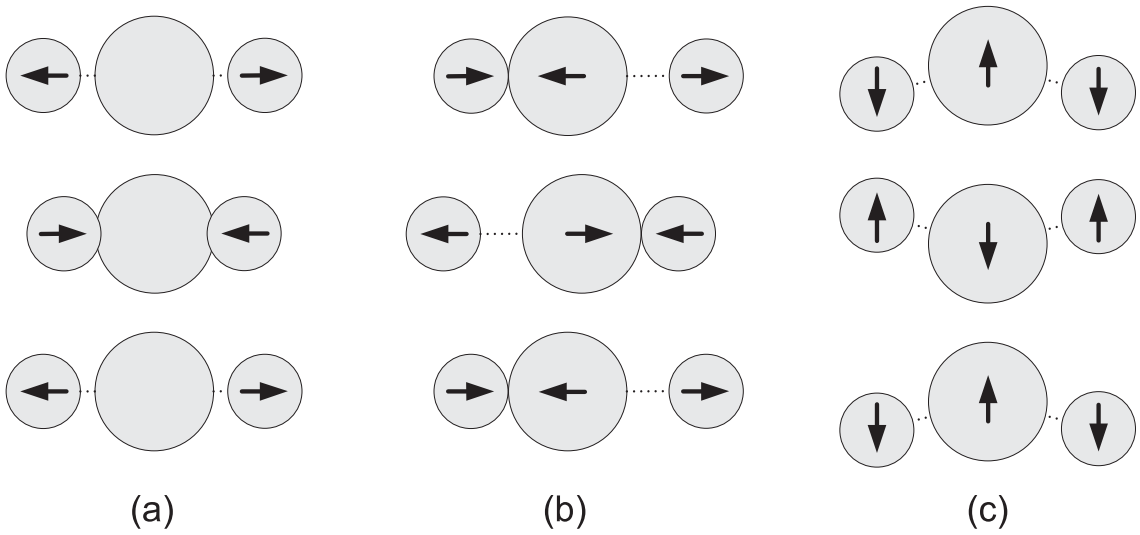

Figure 2.4: The complete set of CO_2 molecule oscillation modes. The molecule in equilibrium has zero dipole moment and it does not change during the type (a) oscillation (symmetric stretching) — the transition to this oscillation is optically not active. Type (b) oscillation (asymmetric stretching) and type (c) (bending) introduce non–zero dipole moment and these can be observed as absorption of mid–IR radiation.

The oscillation around the equilibrium is very accurately described with an idea of the harmonic oscillator, which assumes a parabolic shape of the potential curve:

$$V = \frac{k}{2}(R - R_0)^2, \tag{2.7}$$

that in turn leads to the quantum mechanic solution for energies in this potential being equally spaced levels:

$$E_v = \hbar\omega\left(v + \frac{1}{2}\right), \tag{2.8}$$

where $v = 0, 1, 2, \ldots$ and ω is a frequency of the classical oscillator, related to the strength of the bond k and the reduced mass in this oscillation μ:

$$\omega = \sqrt{\frac{k}{\mu}}. \tag{2.9}$$

Again, as in the case of the rotational transitions, there is a *selection rule* for oscillation transitions. In a quantum mechanical description, states of the molecule are identified with wavefunctions and the probabilities of the transitions between these states may be expressed as integrals being *the transition dipole moments*:

$$\vec{\mu}_{\mathrm{I}\to\mathrm{F}} = -e \int \psi_{\mathrm{F}}^{*}\, \vec{r}\, \psi_{\mathrm{I}}\, dt. \tag{2.10}$$

If the transition dipole moment is zero, the transition does not occur (is *forbidden*). It is just a strict quantum mechanical expression for the requirement that the electric dipole $\vec{\mu}$ must change during the transition. If the harmonic oscillator model is assumed, the analytic solutions for the wavefunctions corresponding to v values are known. From their properties it can be shown that only the transitions for which

$$\Delta v = \pm 1 \tag{2.11}$$

will appear as for these combinations of the wavefunctions $|\vec{\mu}|^2 \neq 0$.

There are no pure vibration absorption spectra. When there is enough energy available from the absorbed light for a vibration, rotations and vibrations co–exist and the excited molecule performs its stretching or bending oscillations simultaneously with rotating. If there are several rotational modes available, in a group of molecules there will be populations excited to different rotation–vibration modes and this will manifest itself by absorption of slightly different energies from the incident radiation — more than one absorption line will be observed. The general schematic explaining the vibration–rotation spectra is shown in Fig. 2.5. The selection rules $\Delta v = \pm 1$ and $\Delta J = \pm 1$ say that for each transition the energy absorbed must be equal to the difference between neighbouring vibration levels ($\hbar\omega$) increased or decreased by a multiple of $2B$, separation between rotational levels.

The harmonic oscillator model, however useful for deriving general results, is not exactly accurate in the case of a molecular bond. The potential well is not an infinite parabola due to the dissociation for large separations. It is necessary to introduce corrections which make the assumptions more realistic. The modification of the shape of the potential curve causes the modification in the shape of the wavefunctions. Two notable consequences of anharmonicity are: unequal spacing of vibration levels and the fact that the selection rule of the form of $\Delta v = \pm 1$ giving the only one absorption energy $E_1 = \hbar\omega$ does not hold strictly any longer.

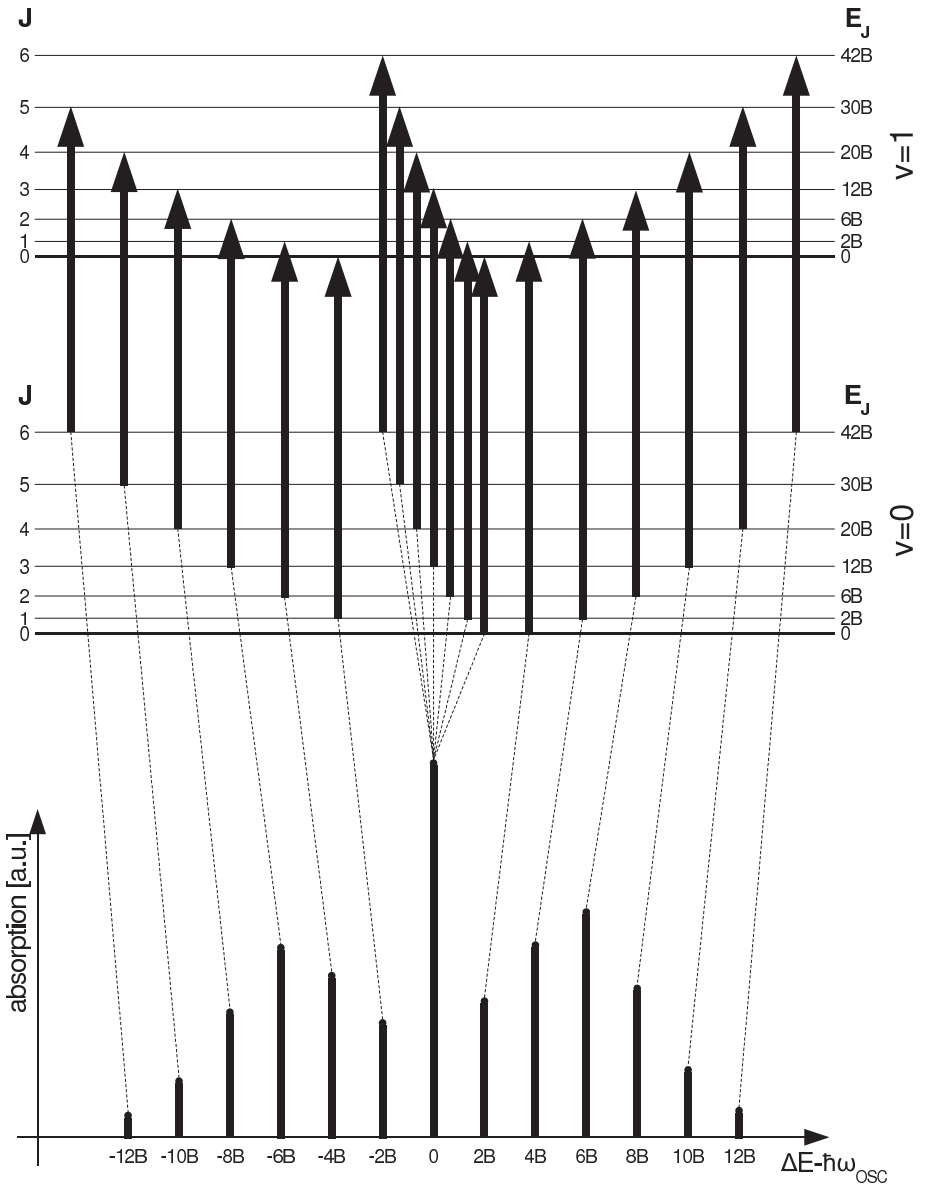

Figure 2.5: The chart shows the formation of the structure of the vibration–rotation molecular absorption spectra. For all the lines $\Delta v = 1$. The central feature is a *Q–branch* and denotes to the situation when the $\Delta J = 0$. The left, smaller–frequency *P–branch* is the result of $\Delta J = -1$ transitions, the right, higher–frequency *R–branch* is the result of $\Delta J = 1$ transitions.

These are the reasons for the appearance of *the overtones*, which are just absorption bands similar to the fundamental one, but surrounding the transitions for $\Delta v = 2, 3, \ldots$ centred at the energies close to the harmonics: $E_2 \approx 2\hbar\omega, E_3 \approx 3\hbar\omega \ldots$ Apart from these overtones, deviations from the purely harmonic oscillations lead to the occurrence of combination vibrations possible to be detected by the absorption of sum frequencies of light: $E_{1+2} = E_1 + E_2, \ldots$

The methane molecule has $3 \cdot 5 - 6$ vibrational degrees of freedom so there exist 9 modes of oscillation. They form four groups having different energies, however in two of these groups the electric dipole moment does not occur so they are optically inactive (see Fig 2.6). The result of this analysis is the observation that

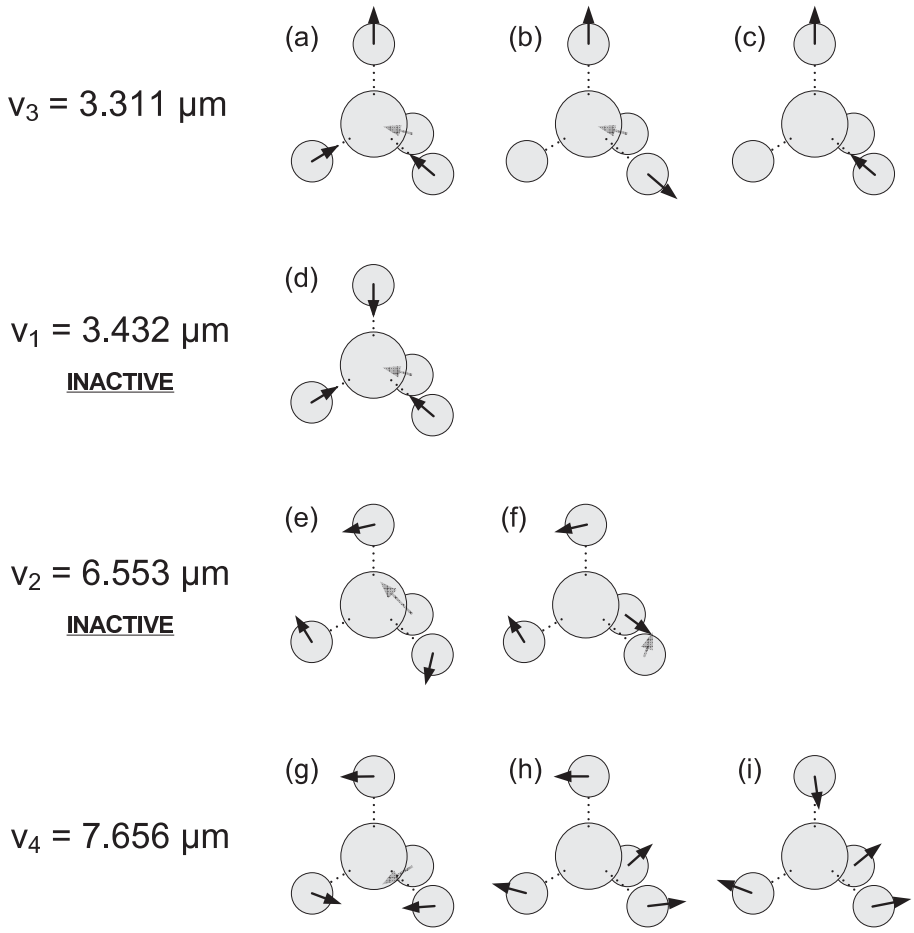

Figure 2.6: All the vibration modes of the methane molecule, grouped by the common oscillation frequencies. For historical reasons they are called ν_1, ν_2, ν_3 and ν_4. ν_1 and ν_2 are optically inactive because $\vec{\mu}$ does not change during these oscillations. Small–energy oscillations ν_4 are bending of all four C–H bonds: three base atoms move towards the centre of the base and the top atom moves either towards one of the base atoms, like (g) and (h) or towards the central point on the side of the base (i). The inactive (e) and (f) at energy ν_2 is bending the bonds in pairs towards each other. ν_1 is also inactive and it is so called "breathing mode" — all three atoms stretch their bonds in phase. ν_3 is also a stretching mode: in (a) three base bonds stretch, in (b) two, and in (c) only one of the base bonds is stretched. The top bond stretches in all the ν_3 cases. These ν_3 modes of vibration are the source of the absorption bands in my experiment.

two fundamental absorption bands are expected, and the experiment supports this: 7.656 µm and 3.311 µm lines were found in 1900's [2.8] and later interpreted as fundamental. Overtones were reported in [2.9, 2.10, 2.11].

An overview of methane spectral absorption lines which can be found in near– and mid–infrared for the wavelengths shorter than 4 µm is pictured in Fig. 2.7. The data has been taken from the HITRAN database [2.12]. In this spectral range the fundamental absorption near 3.311 µm is strongest and thus measurement techniques exploiting this wavelength region should be most sensitive, even two orders of magnitude more sensitive than those using the strongest overtone. Two overtones shown are the second harmonic of the fundamental ν_3 around 1.66 µm and the combination of two fundamental oscillations $\nu_3 + \nu_4$ around 2.35 µm. Relative transitions intensities can be seen in a logarithmic scale in Fig. 2.8.

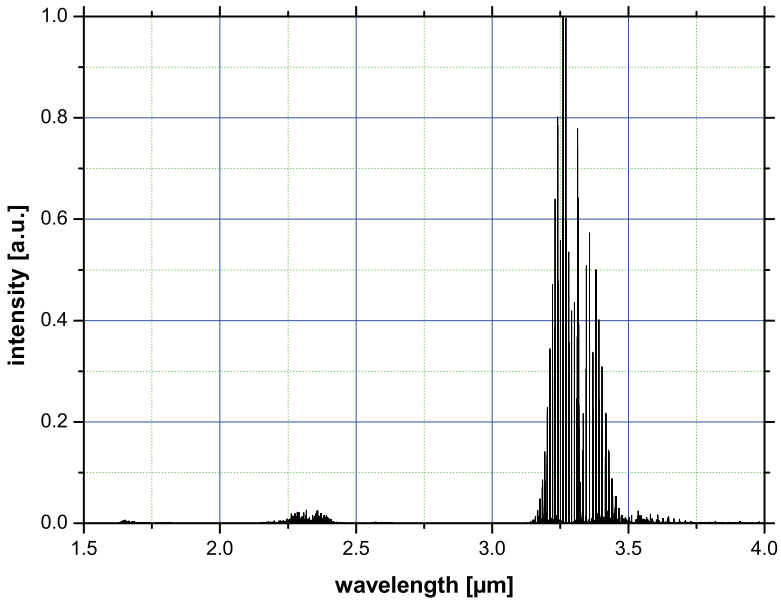

Figure 2.7: Intensities of methane absorption lines in near– and mid–infrared. The linear scale shows only fundamental transitions around 3.3 µm, overtones are almost invisible in this scale. A detection system working beyond 3 µm presents a huge, evident advantage over one trying to detect overtones.

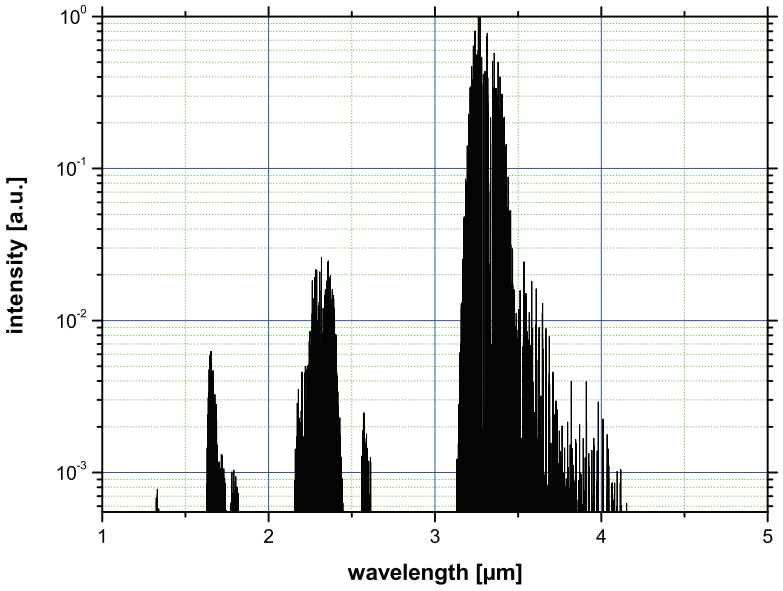

Figure 2.8: Intensities of methane absorption lines in the near– and mid–infrared. The logarithmic scale shows a comparison between the intensities of fundamental transitions and the overtones, which are around 100 times weaker. 1.66 μm is a wavelength of the first overtone (second harmonic of ν_3 at 3.31 μm fundamental frequency, often referred to as $2\nu_3$) and 2.35 μm absorption originates from a combination of ν_4 at 7.7 μm and ν_3 fundamentals, hence is commonly called $\nu_3 + \nu_4$.

2.3 Overview of methane sensing techniques

Optical absorption–based sensors in principle can use light sources emitting any wavelength which is known to be absorbed by methane molecules — either fundamental bands or one of various overtones. The ability to work in the region of fundamental absorption offers one advantage of a great importance — the sensitivity possible there is, on average, about two orders of magnitude higher than in any of the overtones. Fundamental absorption bands of methane are centred around 7.65 μm and 3.31 μm and the most frequently used overtone wavelengths for this molecule are 2.35 μm and 1.66 μm.

There are two general strategies for gas sensing when it comes to the choice of the light source class. One incorporates an extremely narrow spectral emission from a tunable source and scanning its central wavelength, this way detecting

the presence of the absorption line. The other makes use of a broadband emission of some kind (not necessarily coherent). Comparison of the spectrum after passing the analysed volume of gas with the reference spectrum should reveal the presence of the absorption lines. In the case of the narrowband emission, only a point detector for power measurement is required, in the broadband device a spectrometer is needed as the source emission must be recorded at many wavelengths simultaneously.

2.3.1 Detection methods

Gases are relatively weakly absorbing so a special effort must be taken to increase the interaction path length and the detection sensitivity. The traditional method of the signal strength enhancement is using an optical multipass cell. Several types of cells have been developed: a White cell [2.13], a Herriott cell [2.14], an astigmatic mirror cell [2.15] and Chernin matrix system [2.16], each capable of offering hundreds of passes through the analyte thus increasing the effective absorption path up to hundreds of metres.

Another method of increasing the optical path for the interaction with gas is cavity ring–down spectroscopy (CRDS) [2.17]. This method is based on measuring of the rate of absorption rather than the magnitude of absorption and is performed in an optical cavity consisting of high–reflectivity mirrors. Typically, a pulsed laser beam is coupled into the cavity through one of the mirrors and stays in the resonator for about ten thousand round–trips. The portion of the beam outcoupled through the other mirror is measured and its decay rate carries the information about the absorption of the examined sample.

Recent advances in photonic fibre technology have brought a new type of gas cell — the core of a hollow optical fibre [2.18]. The method is seen as particularly promising due to the reliability of manufacturing long optical fibres. However, for long and small core–diameter fibres there still remains the problem of introducing the gas of interest into the fibre. Forced pumping is one of the solutions [2.19], but it requires complicated pump and gas circuits not necessarily suitable for a portable gas–sensing device, so the efforts have been made to let the gas flow through the micrometre–sized holes drilled with focussed femtosecond laser pulses in the fibre wall with good results [2.20].

Photoacoustic spectroscopy is another technique for the sensitive spectroscopic measurements, however it is not a direct method — absorption of laser light occurs in a specially designed cell, but it is detected by means of the acoustic signal. A miniature microphone measures the sound wave generated by the absorption of the beam with an amplitude modulated at acoustic frequencies (for example, see [2.21]). The sound intensity changes revealing the variable absorption induced by tunable light radiation.

Frequency–modulation spectroscopy is a powerful technique exploiting the ability of laser diodes to be rapidly tuned by varying driving current. Sine–wave modulation introduces two sidebands into the light spectrum, $\omega_0 - \Omega$ and $\omega_0 + \Omega$, where ω_0 is the frequency of laser beam and Ω is the modulation frequency. If during the interaction with the gas, one of the sidebands is absorbed more strongly than the other (is positioned inside the absorption line), it becomes evident after detection as the asymmetric result will not combine back to the original shape of identically modulated signal. For an example of the technique strength, see [2.22].

2.3.2 Spectral ranges and light sources

The most convenient source in terms of operating simplicity, life time and modulation possibility is a laser diode, which falls into the narrowband category. Driven only by the applied current, it can be the part of a miniaturised sensor together with a small detector. The 1.65 μm overtone is relatively simple to reach with a popular InGaAs or GaInPAs laser diode light and can be used for methane sensing [2.21, 2.23, 2.24]. However, lower–order overtones or ideally fundamentals are more desired for sensitivity improvement. Quantum–well lasers are the examples of recent advances in the mid–IR optics technology. Quantum–well antimonide laser diodes allow for a single–wavelength operation engineerable by a careful choice of the thickness and composition of the layers. Both 2.35 μm and 3.3 μm regions were reached with this type of lasers [2.25,2.26,2.27,2.28,2.29,2.30], however not all of them were suitable for operation in room temperatures.

Another type of laser diode which can be engineered to operate in the mid–IR fundamental methane absorption bands is the lead salt–based laser diode. The difficulty in this case is the need for a cryogenic cooler, which makes it quite complicated. The operation temperatures are in the range of 15–80 K. Gas sensing

experiments were successfully performed with the use of these lasers [2.22, 2.31].

The relatively new technology of quantum cascade laser diodes gives access to 3–24 μm spectral range. Until recently it was not possible to manufacture these kind of diodes for a continuous work mode in room temperatures, but this difficulty has been removed now (for example, see [2.32]). This technology has been widely tested in the application of methane detection [2.33, 2.23, 2.34].

Recent advances in the tunable solid state lasers technology revealed promising media for mid–IR broadband emission. One example is Cr^{2+}:ZnSe, which is suitable for the construction of a femtosecond oscillator in the 2–3 μm range. A methane sensing device based on this type of laser and Fourier–transform detection method was successfully built [2.35].

The thulium–doped fibre laser capable of emitting 2.2–2.4 μm light was used to perform the methane sensing experiment based on $\nu_3 + \nu_4$ overtone [2.36].

There has been some work done on a $\Delta\nu = 2$ overtone in CO gas–based lasers. They can be tuned to the region of 3 μm and methane sensing using the CRDS technique was performed with the high sensitivity there [2.37].

The phenomenon of difference frequency generation in nonlinear crystals may be used to access some spectral regions not available by other means with lasers. The availability of periodically poled crystals which can be prepared for the quasi–phasematching in a broad range of wavelengths made possible methane sensing in fundamental absorption regions [2.38, 2.39, 2.40, 2.41].

Optical parametric oscillators are powerful tools offering relatively high output powers and tunability over wide spectral ranges. The continuously working–type was used as a tunable light source in a methane detecting device [2.42]. The broadband femtosecond version was also tested with good results in conjunction with the Fourier transform measurement technique [2.43]. My experiment relied on a femtosecond OPO as well.

Generally, laser diodes are the most attractive light sources for various gas sensing devices due to low manufacturing costs and simplicity in use but they lack tunability which could be very advantageous in some applications. A broadband femtosecond laser diode would be ideal and there are already the first signs of this technology approaching, e.g. as described in a review paper of Rafailov and co–workers [2.44] but still the solid state–based laser and parametric oscillators which are products of a well established technology offer the spectrally

broadest coherent radiation flexibly tunable within spectroscopic regions of interest. In this experiment, with a lithium niobate–based OPO, it was expected to obtain a few tens of milliwatts of light with its spectrum at least partially overlapped with one of the fundamental absorption bands of methane so it was predicted to be a suitable light source for this application, offering potentially high sensitivity.

2.3.3 Summary of detection schemes

The majority of solutions rely on using a narrow–band emitting laser tuned to one of the known absorption lines and power measurement with a photodiode after passing through the gas. Usually a laser diode is the first choice device. Typical powers are not easily detectable (of the order of µW) so a frequently adopted strategy is using the liquid nitrogen–cooled HgCdTe or similar photodiode. Detection sensitivities for this kind of sensor are well below 1 ppb level, however frequently these devices are only laboratory prototypes.

Rarely used for the reasons of complexity are broadband sources–based detectors, which record the events of absorption as changes in the spectrum transmitted through the gas cell or generally space under examination. They offer a broader image of the phenomenon of absorption as many lines are visible simultaneously and additionally the presence of several species can be tested with the same laser. In particular, femtosecond oscillators do not compromise the beam quality — unlike thermal sources — and possess the high spectral density while still covering tens or hundreds of nanometres so can be reliably used similarly to CW–lasers in the experiment and offer the rapid acquisition of data rich in spectral information. In order to obtain a satisfactory spectral resolution, the preferred technique of wavelength measurement in the mid–IR is the Fourier–transform spectroscopy, presented in detail on page 51.

The examples of methane sensing experiments described in scientific journals are presented in the table 2.1. The current trend is development of laser diodes working at fundamental absorption frequencies which, due to the fact that the technique is well known, should bring rapid improvement of results and further miniaturisation without losing sensitivity.

Table 2.1: Comparison of different optical methods of methane detection

Light source	Wavelength	Detection method	Sensitivity	Reference
CW tunable sources				
InGaAs laser diode	1.59–1.67 µm	photoacoustic	14 ppm	[2.21]
laser diode	1.65 µm	photoacoustic	0.15 ppm	[2.23]
GaInPAs laser diode	1.64–1.67 µm	multipass cell, Ge detectors	0.04 ppm	[2.24]
InAsSb laser diode	3–4 µm	multipass cell, HgCdTe detector	0.002 ppm	[2.29]
Pb–salt laser diode	8 µm	multipass cell, HgCdTe detector	0.02 ppm	[2.31]
	7.8 µm	frequency modulation, HgCdTe detector	0.000050 ppm	[2.22]
Quantum cascade laser diode	7.84 µm	multipass cell, HgCdTe detector	0.005 ppm	[2.33]
	7.85–7.90 µm	photoacoustic	0.003 ppm	[2.23]
	7.93 µm	multipass cell, HgCdTe detector	0.003 ppm	[2.34]
Tunable solid state (Cr^{2+}:ZnSe)	2.28–2.37 µm	photoacoustic	0.8 ppm	[2.35]
Difference frequency generator	3.5 µm	multipass cell, HgCdTe detector	10 ppm	[2.38]
	2.9–3.5 µm	multipass cell	0.003 ppm	[2.39]
	3.36 µm	wavelength modulation, InSb detector	0.047 ppm	[2.40]
	3.3 µm	multipass cell, HgCdTe detector	0.028 ppm	[2.41]
Optical parametric oscillator	3.2 µm	CRDS	0.00016 ppm	[2.42]
CO laser	3 µm	CRDS	0.0001 ppm	[2.37]
Supercontinuum	1.62–1.70 µm	multipass free space	8000 ppm	[2.45]
Tm^{3+}–doped fibre laser	2.2–2.4 µm	gas cell, InAs detector	150 ppm	[2.36]
Broadband sources				
fs optical parametric oscillator	3.2–3.8 µm	gas cell, PbSe detector	2 ppm	[2.43]

My experiment aimed at joining two promising techniques — photonic crystal fibre as a gas cell and a femtosecond optical parametric oscillator, both suitable for the use at the wavelengths of one of the fundamental absorption bands.

2.4 Optical parametric oscillator design

The main idea of this experiment was to examine the possibility of observing the methane absorption at one of the fundamental bands (namely 3.31 µm) using a prototype silica photonic crystal fibre having guided modes at these wavelengths, reported in [2.46]. As the maximum of the transmission for this fibre was not accurately aligned with the methane band structure, we decided to build the laser source tunable in the range of the overlap available, namely around 3.15–3.30 µm. In the previous experiments performed in our group, also related to methane spectroscopy [2.43], an OPO was used working in the same spectral region so it was decided to adopt the same approach. The requirements now were: tunability between at least 3.15–3.30 µm, and the ability to extract this mid–IR light from the OPO cavity with as small losses as possible and average power of the order of tens of milliwatts. From previous experience it was known that it should be possible to obtain this from a signal–resonant OPO built around a PPLN crystal with grating periods in the range of around 21 µm pumped by an 800 nm–centred femtosecond oscillator.

The OPO used in this experiment was designed as an X–cavity, signal–resonant device pumped by a Ti:sapphire femtosecond oscillator and the exact configuration is shown in Fig 2.9.

The pump laser was emitting ≈100 fs pulses at a wavelength around 800 nm with a repetition frequency of 105.25 MHz. The typical spectral width was 10 nm. The PPLN crystal was 12 mm–high, 0.5 mm–thick and 1 mm–long, with several grating periods, ranging from 20.5 to 22 µm. The cavity consisted of a focusing section of two concave mirrors (R=−100 mm) and two arms ending with plane mirrors. A stable cavity configuration was found using program LCAV, which calculates beam sizes along the optical axis by applying an ABCD matrix analysis, taking into account astigmatism introduced by slightly tilted mirrors. Beam clearance past the PPLN crystal required a mirror tilt angle of 4°, but this was small enough to allow stable operation. To maintain stability the distance be-

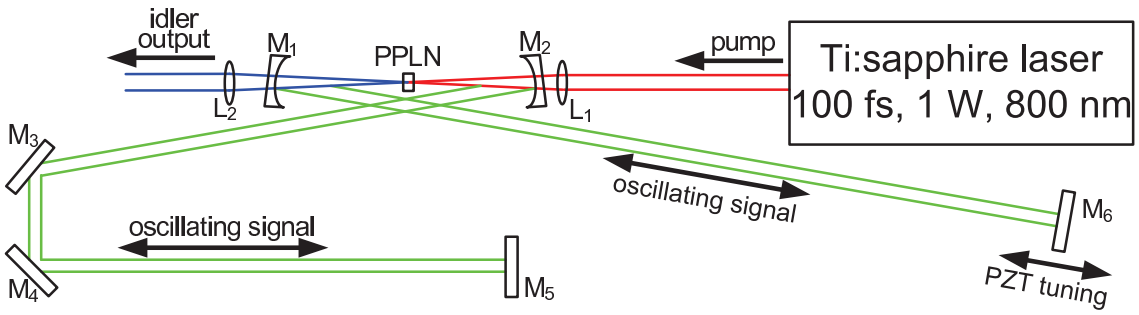

Figure 2.9: OPO cavity schematic. Ti:sapphire femtosecond oscillator working around 800 nm is the pump laser. The signal–resonant cavity consists of two curved mirrors M_1 and M_2 and plane mirrors M_3–M_6. L_1: 63 mm focal length BK7 lens for the pump beam focusing, L_2: 100 mm focal length CaF_2 lens for the idler beam collimation, M_1: R= −100 mm, CaF_2 mirror, HT (highly transmittive) for idler wavelengths (2.8–3.4 µm) and pump (750–850 µm), HR (highly reflective) for signal (950–1150 µm), M_2: R= −100 mm, BK7 mirror, HT and AR (anti–reflective) for pump (750–850 µm), HR for signal (950–1150 µm), M_3–M_6: plane, BK7 mirrors, HR for signal (950–1150 µm), PPLN: the periodically poled $LiNbO_3$ crystal formed in several gratings with periods varying from 20.5 to 22 µm. M_6 mirror position along the beam (cavity length in practice) can be adjusted by a piezo–element within the range of 9 µm.

tween the curved mirrors and crystal was set to 51 mm. The cavity arms were chosen to be symmetric, each being approximately 66 cm long.

The mirror coatings were designed as high–reflectors for signal wavelength (950–1150 nm) but not for the idler (2.8–3.4 µm) and pump wavelengths. On the contrary, these beams left the cavity through the first mirror they encountered (M_1) after interacting in the crystal. As the OPO was a synchronously pumped device, its cavity length had to match pump laser cavity length. One of the end mirrors was mounted on a translation stage to allow for precise matching of cavity round–trip time to frequency of incoming pump pulses. The lithium niobate crystal was mounted in an oven mount and kept at a temperature of 84°C to avoid photorefractive damage. The details of the mount design are shown in Figure 2.10.

To characterise the output of the oscillator and perform later absorption measurements it was essential to build a dedicated spectrometer to have a necessary

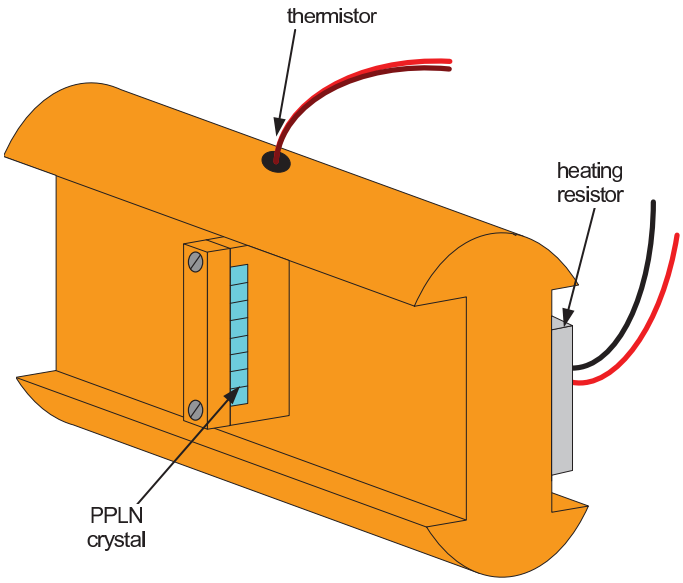

Figure 2.10: The detailed view of the OPO crystal mount. The resistor heats the mount and the thermistor detects the temperature to provide the feedback. Both electrical circuits are served by a laser diode controller. The crystal clamped in the mount is vertically split into several separate gratings what allows for adjusting different mode–locking conditions (the grating period) by sliding the entire mount in the vertical direction. The pump beam is always focused in one of the gratings. The outer diameter of the mount is 25.4 mm.

design flexibility for the setup. Prior to the construction of the experiment all the requirements and constraints were not obvious so it was desirable to be able to redesign the spectrometer itself to adapt for any new concepts. The planned use of the home–built OPO and the fibre connected to the gas installation forced the layout to be open to redesigning should any unprecedented difficulties arise. Additionally, the acquisition rate for the spectrometer had to be high enough to give reliable results even for a fluctuating OPO output, which was anticipated. In our design it was straightforward to manipulate both the acquisition frequency and the resolution of the device as we chose the build the Fourier–transform spectrometer.

2.5 Fourier transform spectrometer

Fourier transform spectroscopic techniques date back to original Michelson experiments on the speed of light and have been developed since then both exper-

imentally and theoretically. The availability of fast computers makes it a very convenient method to measure a spectrum over an extremely broad range of wavelengths. A thorough review of the fundamental principles can be found in [2.47].

2.5.1 FTIR data acquisition and processing

In general, this method is based on the Michelson interferometer (Fig. 2.11).

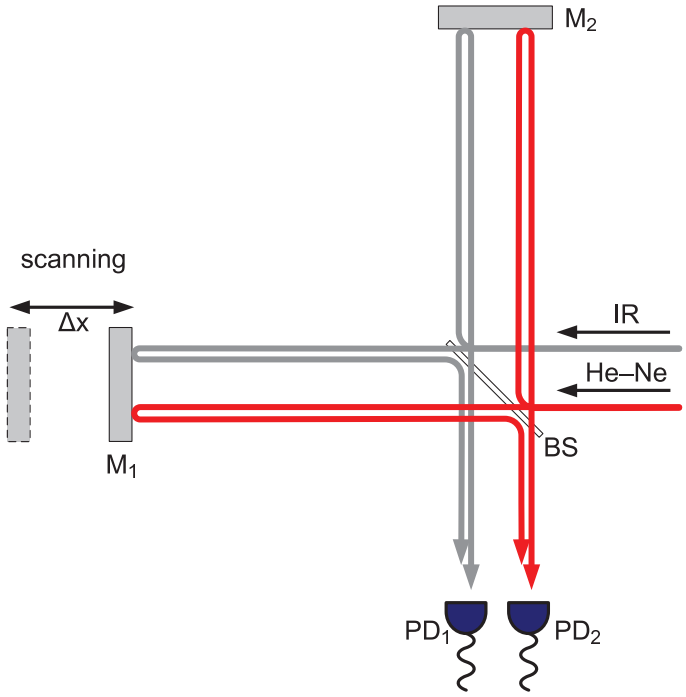

Figure 2.11: Michelson interferometer used in FTIR measurements. Gray and red arrows symbolise directions of propagation of the IR and He–Ne beams, repsectively, in both interferometer arms. BS is beamsplitter, M_1 and M_2 are mirrors, PD_1 and PD_2 are the photodiodes which record interference patterns by linear absorption of incident IR or He–Ne light, respectively. Δx is the scan amplitude, so due to the double–pass geometry the total arms length difference introduced by the scan is $2\Delta x$.

One of the arms is scanned around zero–delay and the output contains a temporal sequence of intensity fringes which can be recorded by a point detector (photodiode). An example is shown in Fig. 2.12. The signal measured by the photodiode at the output of the Michelson interferometer is called *the interfero-*

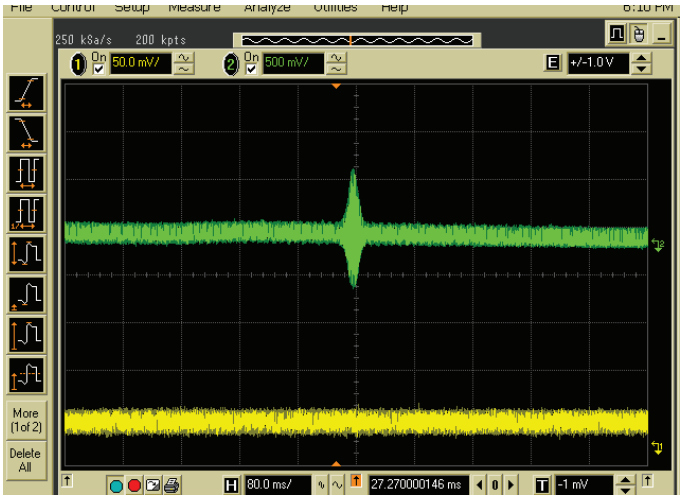

Figure 2.12: Example of the intensity fringes from the oscilloscope screen. Green trace denotes OPO idler and yellow the He–Ne laser. Scan takes 0.8 s and contains 250000 points.

gram and can be expressed using input electric field values $E(t)$ as:

$$I_{\mathrm{OUT}}(\tau) = \int_{-\infty}^{\infty} |E(t-\tau) + E(t)|^2 \, dt. \tag{2.12}$$

Further manipulation reveals the intuitive separation of the negative–, zero– and positive–frequency terms in the Fourier transform of the interferogram:

$$\begin{aligned} I_{\mathrm{OUT}}(\tau) &= \int_{-\infty}^{\infty} 2I(t)dt + \int_{-\infty}^{\infty} [E(t)E^*(t-\tau) + E^*(t)E(t-\tau)]\, dt \\ &= \underbrace{\mathrm{const}(\tau)}_{\omega=0} + \underbrace{\mathcal{F}^{-1}[I(\omega)]}_{+\omega} + \underbrace{\mathcal{F}^{-1}[I(-\omega)]}_{-\omega}, \end{aligned} \tag{2.13}$$

where $\mathcal{F}^{-1}$ is the inverse Fourier transform operator.

Isolating the positive frequency component and applying the Fourier transform to it leaves us with the complex spectrum

$$I(\omega) = |I(\omega)| \cdot e^{i\Delta\varphi}, \tag{2.14}$$

where $|I(\omega)|$ is the spectrum and $\Delta\varphi$ is the phase difference between two interferometer arms which can be discarded in the spectrum measurements. The figure 2.13 shows schematically the data manipulation process.

A separate problem presents itself in obtaining the frequency (or eventually wavelength) scale which depends on the temporal distance between the data points in the interferogram. A very accurate way of calibrating this acquisition

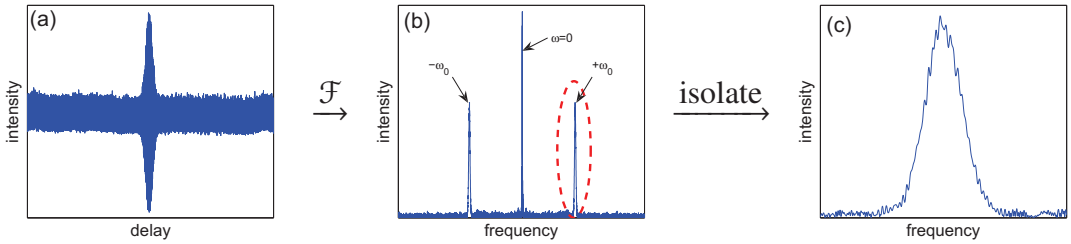

Figure 2.13: The schematic of the FTIR data processing. Graph (a) shows the raw interferogram captured from the oscilloscope, represented by eq. 2.12. Fourier transform applied to this data gives the (b) data set in frequency domain. Negative–, zero– and positive–frequency components become visible then according to the eq. 2.13. The absolute value of the positive frequency peak is the spectrum intensity, shown isolated in the figure (c). The proper frequency scale is extracted separately from the He–Ne interferogram.

step is using a He–Ne laser in the same interferometer and recording its interferogram with a separate detector, yielding a sine–wave. It is known that one period corresponds to the distance of one wavelength which is determined accurately to be 632.8 nm. The He–Ne interferogram is recorded for entire length of the scan for the main signal, so at each point of the signal interferogram there is a local "ruler" made from fringes arranged in 632.8 nm intervals. The extra feature is the possibility of expanding the working distance for the scan even beyond the linear regime, as the He–Ne fringes always preserve the local distance measure so there is no need to assume the same distance between data points in the entire set. After extracting the position scale from the He–Ne fringes, it is possible to rescale the signal interferogram to the delay units by the simple relationship $\tau = x/c$, where τ is the delay, x is the position and c is the velocity of light. After these manipulations, real frequency units appear naturally in the Fourier–transforming process. According to needs, the spectrum can be shown in wavelength units, using $\lambda = c/\nu$ relationship, where ν is the original frequency scale and λ is the wavelength scale.

As the He–Ne interferogram is not always of excellent quality, a fringes–thresholding and counting computer algorithm was employed as a crucial part of the data–processing software.

2.5.2 Experimental details of the FTIR spectrometer

The actual scanning device in our spectrometer was a loudspeaker which allowed for a simple scanning frequency adjustment. It was driven by a standard sine–wave signal generator and an audio amplifier. There was a silver mirror attached to the moving part of the speaker. The practical scan distance was limited to about 6 mm due to the properties of the speaker. The idler wavelength–dedicated PbSe detector was unfortunately too slow to resolve the interference fringes for scan frequencies higher than 1 Hz. The other arm was built from the mirror mounted on a translation stage so the zero–delay position could be accurately found.

The Infrasil beamsplitter was not optimised for 50/50 operation at 3.3 μm wavelength but still it was working sufficiently well (60/30 with 10% absorption). At the He–Ne wavelength of 632.8 nm the splitting was 82/14 but the interference fringes were visible.

2.5.3 Sampling and resolution criteria

The classic paper of Shannon [2.48] contains the rigorous proof of the fact that in order to accurately and uniquely sample a continuous, bandwidth–limited signal it is necessary to probe it more frequently than two times per the shortest period corresponding to the highest frequency f_{MAX}:

$$\begin{aligned} f_{\mathrm{S}} &> 2f_{\mathrm{MAX}} \Rightarrow \\ \delta t_{\mathrm{S}} &< \frac{1}{2f_{\mathrm{MAX}}}, \end{aligned} \tag{2.15}$$

what is known as *the Nyquist criterion*. δt_{S} is a temporal distance between points in the sampled signal and f_{S} is the sampling frequency.

When applied to the conditions of my experiment, the Nyquist criterion requires more than two samples per a He–Ne period as this laser possesses the shortest wavelength used in the measurements so the corresponding temporal variations in the signal are the quickest ones for this laser. The experimental limit was the number of points in the memory of the oscilloscope but it was quite high and equal to 250000. This fixed number of points could be used to sample a certain number of He–Ne interference fringes and there is an upper limit to this number — with 250000 points not more than 125000 periods can be uniquely

sampled. It puts the limit to the amplitude of the scan Δx:

$$\begin{aligned} 2\Delta x &< 125000 \cdot 632.8\text{nm} \\ \Delta x &< 39\text{mm}, \end{aligned} \tag{2.16}$$

and the reason for $2\Delta x$ multiplication is that in the Michelson interferometer modifying the length of one arm by Δx causes the modification of the overall optical path in this arm by $2\Delta x$ due to the double pass geometry.

The Fourier transform properties say that the distance between points in one of the domains is tightly related to the span in the other domain, so for example in the case of the distance between points in the spectrum (effectively spectral resolution) depends on the signal recorded in time:

$$\delta\nu = \frac{1}{\Delta t}, \tag{2.17}$$

which means that the increase of the spectral resolution can be obtained by recording longer temporal sequences of the signal. In my experiment the available temporal sequence is strictly limited by the oscillation amplitude of the speaker, which could not be higher than 2 mm and the eventually used cropped optical path scan was 3 mm, implying the resolution of about 3.6 nm. Simultaneously it means that the sampling rate was sufficient as the limit of 39 mm was much higher than the actual amplitude.

Another parameter which was limited in the experiment was the scan speed. In principle it should be as high as possible to minimise the sensitivity to the OPO temporal instability. In practice the upper limit was caused by the PbSe detector speed and in order to record the vertically symmetrical trace it was essential not to increase the scan frequency above 1 Hz. To safely reject the scan turning points which were the regions where the interference fringes were not readable, the temporal window was cropped to 0.8 s and this number can be defined as the duration of a single measurement.

2.6 Optical parametric oscillator characterisation

The OPO was designed exclusively with the use of non–resonant idler in mind so there was no output coupler for resonating signal wavelengths and no measurements of the signal were performed, however, to show the versatility of this device, I measured its spectrum in the visible and the near–IR, and this is shown in

Fig. 2.14. The signal peak, which should be present in the area of 1000–1100 nm, is not visible due to lack of output coupling because this wavelength did not leave the cavity. Instead, a very strong peak of the second harmonic of the signal is clearly visible. The cavity mirrors were transparent at these wavelengths and this $2\omega_S$ was a useful monitor of the OPO operation. The ≈500–550 nm–centred peak of a bright green–orange light was initially a clear indication of the oscillation and was helpful during the alignment process. In later measurements the spectrum of $2\omega_S$ was monitored and its position was used as an indirect measure of the repeatability and stability of the idler central wavelength.

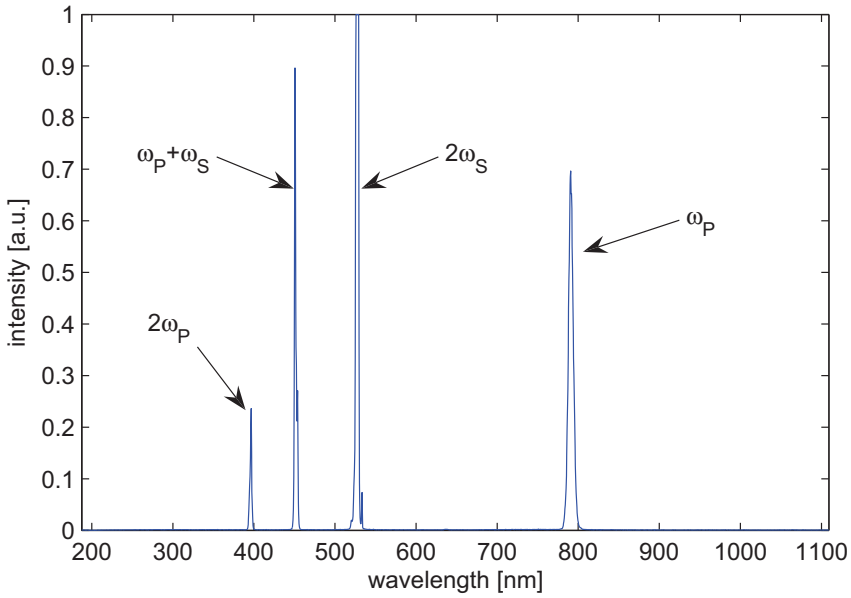

Figure 2.14: OPO spectrum in the visible and near–IR. ω_P is the pump frequency, but other frequencies are generated in the OPO crystal in non–phase–matched processes: $2\omega_P$ is the second harmonic of the pump, $\omega_P + \omega_S$ is the pump mixed with the signal and $2\omega_S$ is the second harmonic of the signal.

The idler tunability was examined for different pump wavelengths (Fig. 2.15). It is clearly visible that the OPO emits idler wavelengths in the spectral region where methane absorption is expected (3.2–3.5 μm) only for a carefully set pump central wavelength and this pump–wavelength sensitivity is caused by the phase–matching conditions which relate the pump and the idler wavelengths to each other. The central wavelength of 801.5 nm was chosen in the experiment as the optimal pump alignment giving the longest idler wavelength at a usable power level.

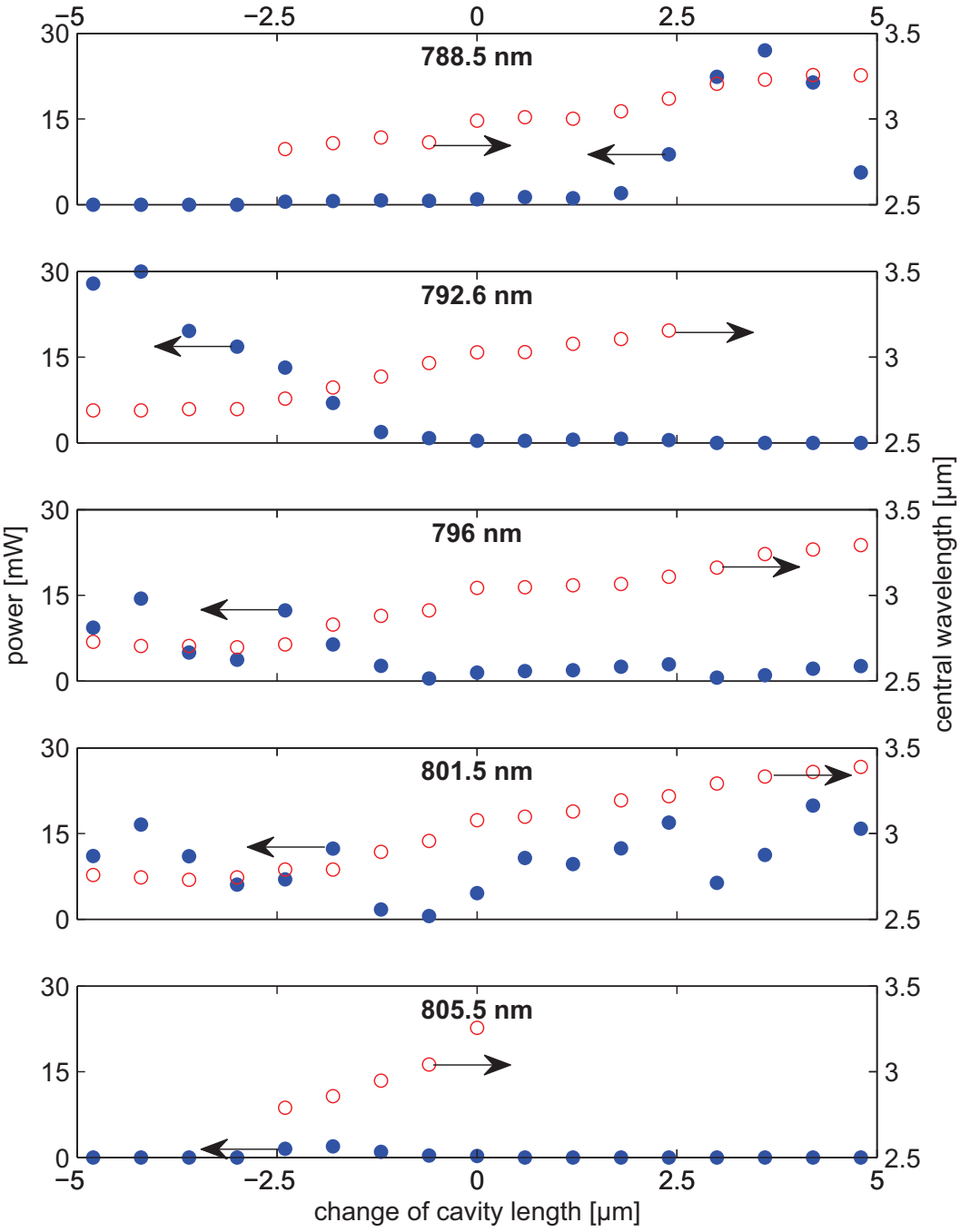

Figure 2.15: OPO idler power and central wavelength as a function of pump wavelength (shown in the top part of each graph) and cavity length. The pump wavelength of 801.5 nm gives the longest idler wavelength for a considerable (≈15 mW) output power and this setting was chosen as the optimal working condition in the experiment.

Additionally, the idler output power as a function of the cavity length for different pump central wavelengths was measured. It is presented in Fig. 2.15 together with the idler tunability. The cavity length window (10 µm) is equal to the total range of the piezo stack. Even though there were still oscillations for shorter cavity length at some settings of the pump wavelength (792.6 nm, 796 nm, and 801.5 nm) they are not acquired due to the fact that there the device emitted wavelengths too short for the experiment. Concatenation of two sets of data for different cavity lengths was not reliably possible so it was decided to record the data for the central wavelengths which were close to the working conditions used later in the experiment.

The typical spectral shapes obtained with the OPO are shown in Fig. 2.16. Two distinctive modes of operation are highlighted: one in the short wavelengths, in the area of 2.7 µm which is not used later in the experiment, and the methane absorption range, in the region of 3.2 µm.

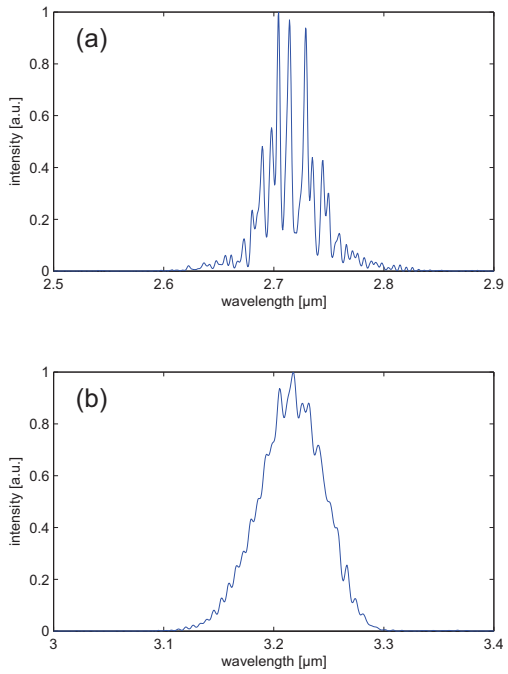

Figure 2.16: OPO example spectra. (a) is for the short–wavelength mode of operation in the region of 2.7 µm, where the water vapour presence causes the absorption lines to appear. (b) is a typical spectrum in the range useful for methane absorption experiment.

2.7 Photonic bandgap fibre as a gas cell

Photonic bandgap fibres utilise a unique idea of using photonic crystals to guide light in a special way, even though the refractive index of a core may be smaller than the one of a cladding. Photonic bandgap structures are media possessing a suitable spectral periodicity of refractive index changes allowing for macroscopic constructive or destructive interference due to multiple reflections, as it happens in the case of reflection from multi–layer stacks of highly–reflective dielectric coatings routinely used as high–reflectivity mirrors. Such mirrors are an example of a 1D photonic bandgap structure and at optical wavelengths the periodicity required is of the order of hundreds of nanometres. For mirror coatings, sputtering and evaporation techniques can be used to deposit dielectric layers of the correct thickness and index, however photonic bandgap fibres involve creating a bandgap in 2D, so the periodic structure required is more sophisticated than simple alternating layers. Using the well–established technique of "fibre–drawing" it is possible to create nano–structured fibres with the correct spatial periodicity needed to achieve a photonic bandgap. The simplified comparison between 1D– and 2D–bandgap structures is shown in Figs. 2.17 and 2.18.

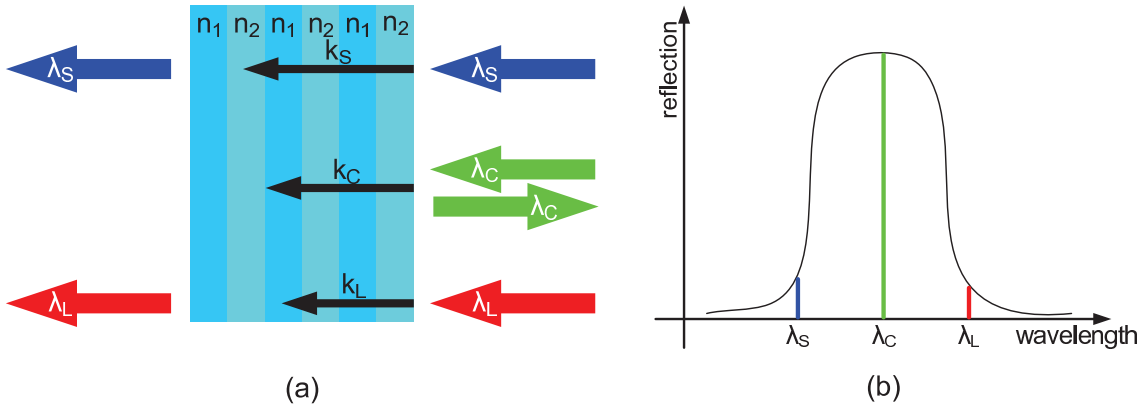

Figure 2.17: The dielectric mirror as an example of a 1D–bandgap structure principle of operation. Alternating layers of n_1 and n_2 refractive index material cause multiple backreflections which interfere destructively or constructively depending on the wavelength of the incident light. (a) shows the geometry of such a device, (b) is a typical reflectivity curve for a mirror of this type.

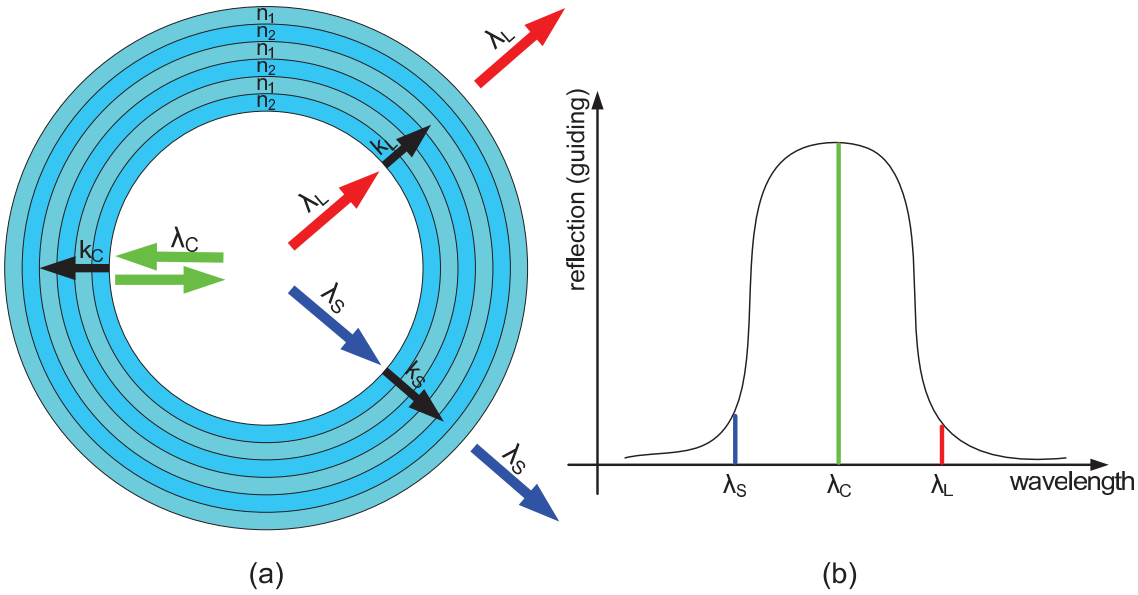

Figure 2.18: The "folded" dielectric mirror called *a Bragg fibre* as an example of a 2D–bandgap structure principle of operation. The reflectivity of the layers is similar in character to the reflectivity in 1D–structure in Fig. 2.17. (a) shows the circular geometry of a device, (b) is a reflectivity curve that simultaneously is a graph of guided wavelengths since the ones which cannot propagate in the structured cladding are forced to remain in the core.

As the principle of fibre operation (guiding) here is not a simple difference of refractive indices between the core and the cladding but the confinement of light in the core is obtained by forbidding its propagation in the cladding due to the periodicity and multiple reflections, even guiding in the air core can be easily engineered — it is the principle of operation of photonic bandgap fibres. *The bandgap* is a frequency region for which the light is forbidden to propagate in the periodic structure, so in the case of the mirror it is the high reflectivity frequency range and in fibres these are the guided frequencies — the only direction in which they are free to propagate is along the structure.

The Bragg fibre, shown in Fig. 2.18 and reported [2.49, 2.50] as scalable to guide light in the range of wavelengths 0.75–10.6 μm, is a device intuitively derived from a 1D Bragg mirror, but usually photonic fibres are manufactured using nanorods rather than nanolayers and as an example of a real structure a photonic bandgap fibre is presented in Fig. 2.19. This geometry opens the field for more flexible fibre characteristics manipulation.

The effect of replacing layers with rods in the photonic fibres is adding new

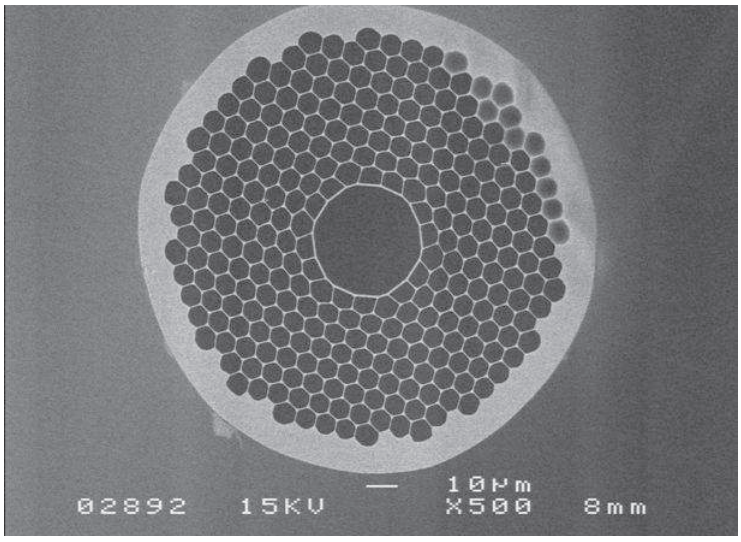

Figure 2.19: Cross–section of a photonic bandgap fibre used in this experiment.

periodicity patterns which can be used to enhance the guiding properties and more finely engineer the bandgap position. Schematically the difference is shown in Fig. 2.20.

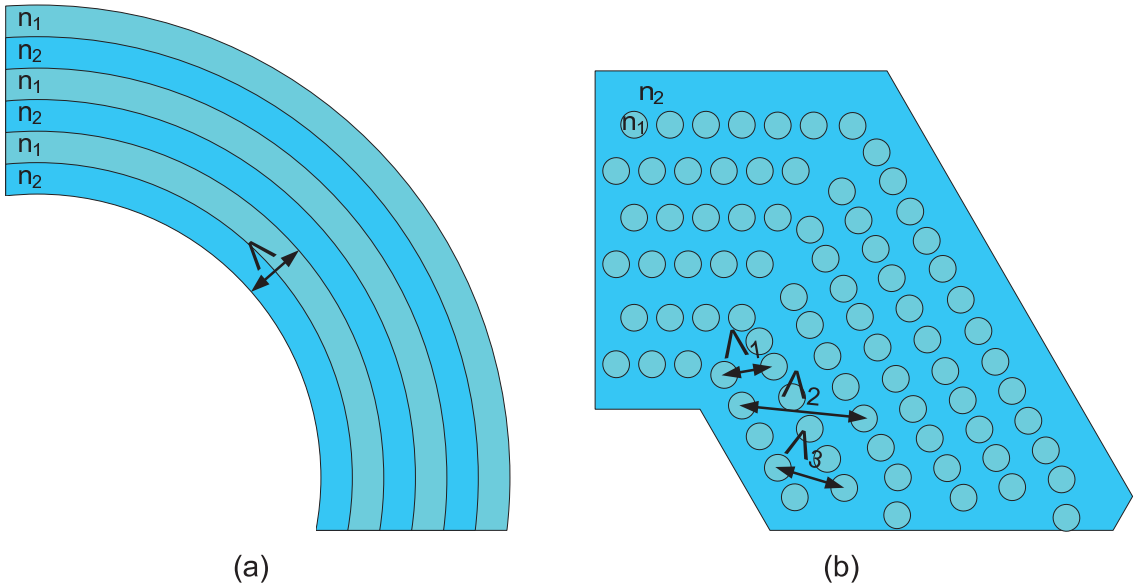

Figure 2.20: The comparison of a single–periodic Bragg fibre (a) with the period Λ and the photonic fibre (b), possessing multiple periodicities Λ_1, Λ_2, Λ_3 and many others, not shown here. This feature may introduce new bandgaps into the transmission profile of the fibre making the fibre suitable to be used in more spectral regions than the simple Bragg fibre. The rods of refractive index n_1 in (b) are very frequently left hollow.

Drawing is a technique which has commonly been applied to manufacturing ordinary optical fibres and by introducing slight modifications it has been adapted for photonic fibre production. The fabrication process consists of preform preparation, but unlike standard fibres that use a single rod of optical material, the preform is prepared as a stack of capillaries which together make a macroscopic model of the final fibre design. More details concerning computational and practical issues in photonic crystal fibres design can be found in an exhaustive review article [2.51].

There are two general types of optical fibres based on the photonic crystal effect — one which leaves a high–index material as a core (*"photonic crystal fibre"*, PCF) and the other whose core is made of a lower–index material, usually air (*"photonic bandgap fibre"*, PBF). The air holes pattern can be arbitrary in any of the fibre types; the only condition which must be met is periodicity. The particular choice of hole distribution determines the fibre's guiding properties, such as spectral transmission, dispersion or mode size. Solid–core fibres may be used to create conditions of high nonlinearity (when entire mode is confined in an area with diameter of the order of micron), but hollow–core fibres, on the contrary, have their modes guided in air (more than 99% of beam travels in a hollow core [2.52]) so nonlinear effects may be totally eliminated or engineered to achieve some specific outcome, e.g. to efficiently deliver soliton pulses [2.53].

Photonic fibres have found many applications so far, including construction of various devices, like: an OPO [2.54], optical sensor and sample collector [2.55], all–fibre chirped pulse amplifier [2.56], pulse compressor by spectral broadening [2.57] and their general capabilities in an aspect of nonlinear optics are reviewed in [2.58].

A choice of a PBF as a gas cell is justified in detail and summarised in [2.18]. The general idea is very simple — the hollow core may be filled with any gas; the propagating light mode will interact with the gas very efficiently due to excellent overlap between gas volume and mode volume. Subsequently this arrangement may be exploited to performing experiments with nonlinear properties of gases (like Raman scattering), locking of lasers to molecular lines or analysing the core contents for the presence of substances of interest. There has been methane sensing with a PBF connected to a vacuum chamber [2.19] and drilled PBF [2.20] performed at overtone wavelengths, but in our experiments it was planned to use a

novel fibre with its bandgap (guided wavelengths region) centred around 3.2 µm, similar to the one described in [2.46] and supplied by Photonics and Photonic Materials Group at the Department of Physics, University of Bath. We planned to use this fibre in the region of fundamental methane absorption around 3.2 µm, where the spectroscopic analysis can be performed potentially with the best sensitivity and where we expected our OPO light source to be emitting sufficient amount of power.

2.8 Characterisation of candidate fibres

As even small environmental variations during the process of photonic fibre drawing may cause the bandgap to be shifted and generally distorted with respect to the theoretical design, we were supplied with several fibres, originating from different fabrication processes. I measured their spectral transmission and compared it with the known position of the methane absorption lines to achieve optimal overlap, taking into account the constraint of the limited OPO tuning abilities. The testing methodology was not complicated and involved measuring the spectrum of OPO pulses coming straight from the oscillator and their subsequent spectrum transmitted through the fibre. These quantities are related to each other in the following way:

$$S_{\mathrm{T}}(\lambda) = S_{\mathrm{IN}}(\lambda) \cdot T_{\mathrm{PBF}}(\lambda), \tag{2.18}$$

where S_{T} is transmitted spectrum, S_{IN} is spectrum measured before the fibre and T_{PBF} is fibre's spectral transmission.

We chose to measure the spectrum with an FTIR method, described before in the section 2.5. The entire optical system consisting of the OPO, FTIR spectrometer components and fibre is visible in Fig. 2.21. A single measurement leading to the spectrum retrieval was always the same, whether it involved fibre or not. Two detectors were used for measuring the interferograms — a Si photodiode recorded the He–Ne trace and a PbSe photodetector recorded the OPO idler. The data acquisition lasted 0.8 s and just before it was started, the spectrum of the second harmonic of the OPO signal was recorded for the reference. The interferograms data was saved to text files and the optical setup was modified to transmit the idler light through the fibre. Then, again just before the measurement was

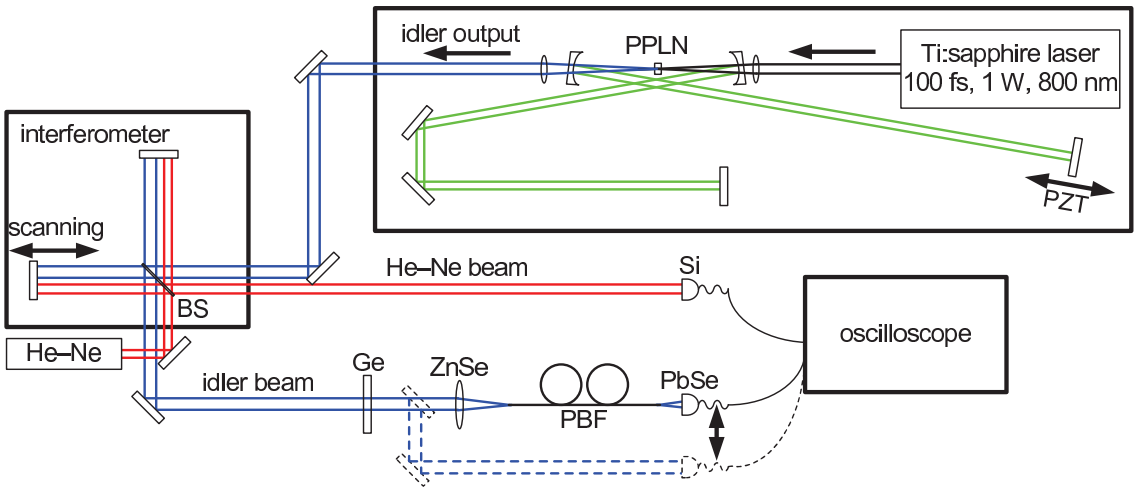

Figure 2.21: Complete measurement setup including pump laser, OPO cavity, Michelson interferometer, He–Ne laser, detectors and fibre. The dashed line shows the beam when the reference measurement (without the fibre) was performed.

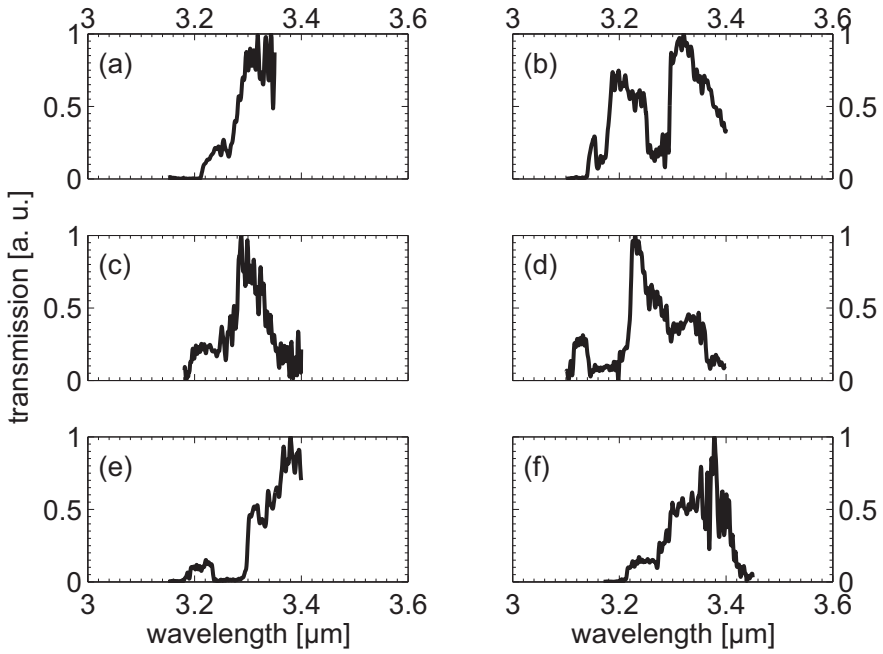

Figure 2.22: Transmissions of six photonic bandgap fibres. At the time of performing this check the OPO was not tunable beyond 3.4 µm so the long–wavelength part of the transmission profile was not always known. After taking into account the available OPO idler spectrum, methane absorption and each fibre's transmission, fibre (b) was chosen as the most suitable for being a gas cell in this experiment.

started, the OPO cavity length was finely tuned with the PZT piezo controller (lead zirconate titanate, $Pb[Zr_xTi_{1-x}]O_3$) so the spectrum of the second harmonic matched the previously recorded one. The overall set of data necessary to obtain the fibre transmission for a single OPO tuning position included four text files: two idler interferograms (the green one in Fig. 2.12) and two corresponding He–Ne traces (the yellow one in the same figure). From each pair of interferograms a spectrum was retrieved with the method described in Section 2.5.1. Then, according to the eq. 2.18, the transmission was calculated. The transmission curves usually extended over a broader range than the idler bandwidth, so the measurements were repeated for other idler central wavelengths and then concatenated to create a continuous transmission profile of the fibre. Six fibres were checked in terms of their transmission around the centre wavelength of the fundamental methane absorption and the results are shown in Fig. 2.22.

2.9 Methane sensing experiment

After choosing the particular fibre with the most suitable transmission properties it was adapted to be a gas cell by terminating it with two mini–cells containing CaF_2 windows for high mid–infrared transmission. The detailed schematic of a terminator is shown in Fig. 2.23. The gas installation was a closed circuit with the added facility of evacuating it or filling with a methane:nitrogen mixture or nitrogen only. The full schematic is shown in Fig. 2.24.

The measurement protocol was as follows: we first acquired the spectrum of the beam propagating in the fibre filled with pure nitrogen where no absorption was expected, then refilled the fibre with a methane:nitrogen mixture and re–measured the spectrum. The two spectra obtained are related to each other in a way similar to the previous transmission formula (2.18):

$$S_{N_2:CH_4}(\lambda) = S_{N_2}(\lambda) \cdot T_{CH_4}(\lambda), \tag{2.19}$$

where $S_{N_2:CH_4}$ is a spectrum after methane and nitrogen absorption, S_{N_2} is a pure OPO spectrum transmitted through the fibre containing nitrogen only and T_{CH_4} is the methane transmission which translates to the absorption shown in Fig. 2.7 in a simple manner, namely:

$$A_{CH_4}(\lambda) = 1 - T_{CH_4}(\lambda), \tag{2.20}$$

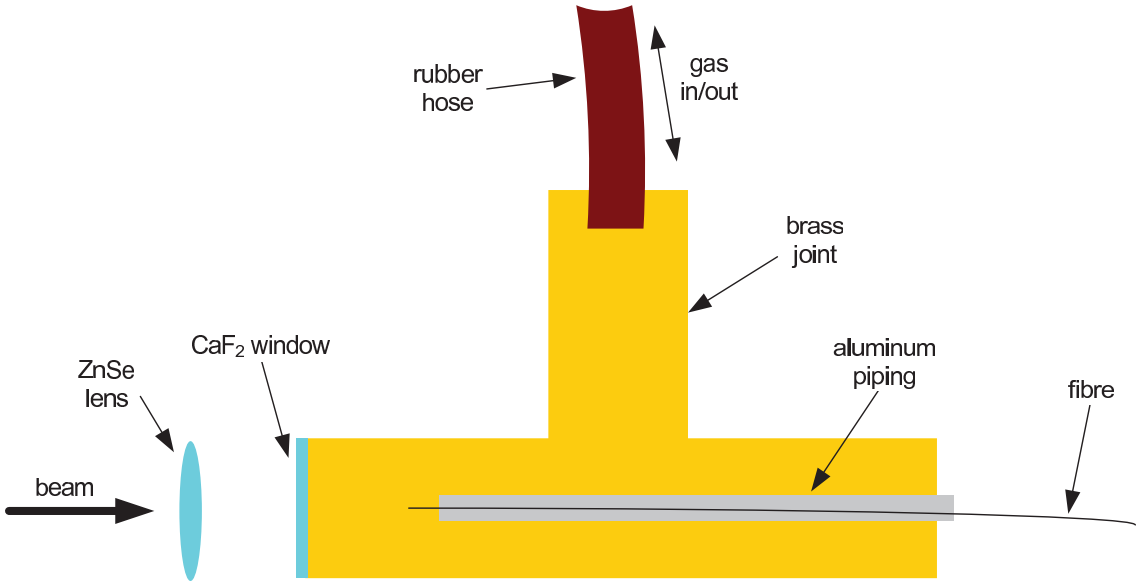

Figure 2.23: One of the fibre terminators. The end of the fibre is sealed with silicon into a brass joint (right port). The left port is a sealed CaF_2 window, ready for coupling the OPO idler into the fibre. The top port of the joint is a sealed rubber hose serving as a gas inlet/outlet.

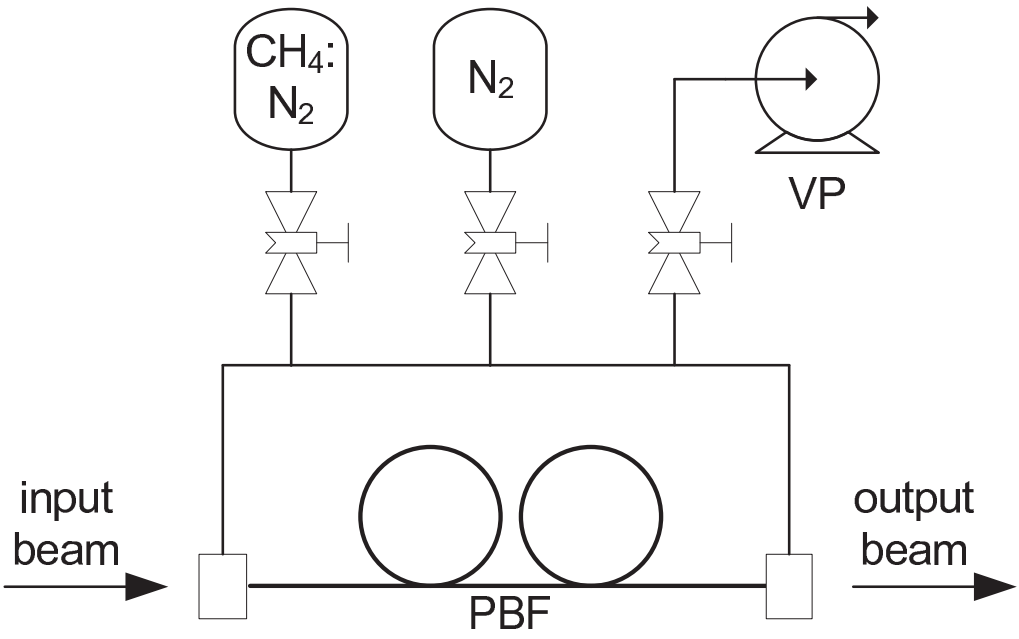

Figure 2.24: Schematic of gas installation used in the experiment. Only one of the valves is open each time: evacuating the circuit with vacuum pump (VP), filling it with methane:nitrogen mixture (CH_4:N_2) or nitrogen only (N_2). PBF is photonic bandgap fibre which transmits both light and gas. The beam goes through both terminators (rectangles) and the fibre.

where A_{CH_4} is methane absorption. Two representative examples of interferograms are shown in Fig. 2.25.

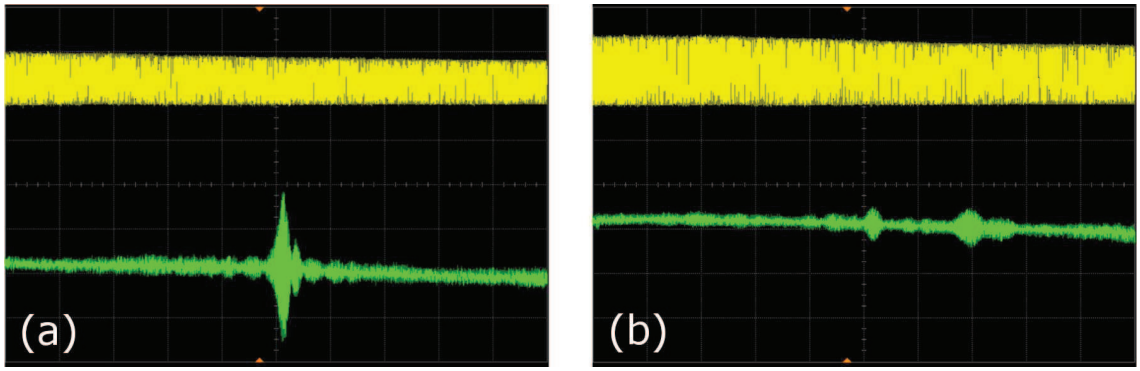

Figure 2.25: Comparison of typical interferograms as seen on an oscilloscope screen. Trace (a) refers to situation without methane in the fibre, so without high–frequency modulations in the spectrum. Trace (b) has substantial portion of high–frequency components what means that spectrum is strongly modulated — contains absorption lines.

The OPO central wavelength was not ideally stable and was vulnerable to environmental changes and this was causing problems during measurements. This behaviour was greatly minimised by the construction of an acrylic glass box surrounding the OPO cavity and covering it from the top, leaving only small holes in the sides for the pump beam, idler output beam and the micrometre screw for rough tuning of the OPO. The only available way of eliminating this completely was manual tuning by modifying cavity length with a precise PZT controller using as a feedback some other OPO–related directly measured spectrum. The second–harmonic of the signal was quite simple to observe after leaving the cavity and was used to monitor OPO tuning changes. The spectrum was recorded once and then before every measurement the cavity length was adjusted so that the currently observed spectrum matched the reference one. However, we did not have any means to introduce such modifications continuously in the sub–second scale of data acquisition so it was not possible to control the idler central wavelength during the scan. This was the most serious source of noise in the main results.

A full set of data, being a result of one measurement at 5% concentration, is presented in Fig. 2.26. It includes a spectrum with and without methane absorp-

tion, calculated absorption and theoretically predicted absorption lines with the best resolution available from the database, of the order of 3 pm.

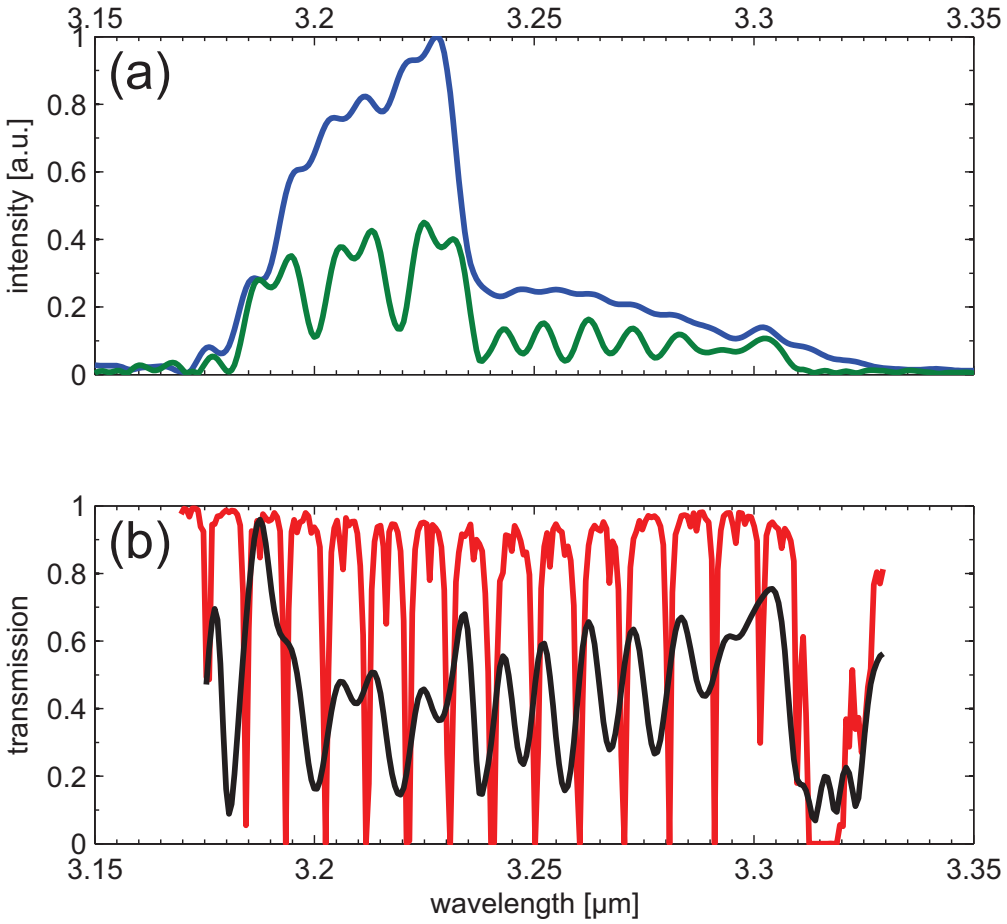

Figure 2.26: Result of 5% concentration measurement. (a) shows spectra obtained by Fourier–transforming of raw interferograms. Blue denotes a spectrum transmitted through a fibre, green is after absorption by methane present in the core. (b) shows transmissions — inferred from measurement (data given in (a)) with a black line and data from HITRAN database with a red line. The constant shift of the experimental results with respect to the theory is apparent.

2.9.1 Spectrum calibration

The lines derived from the measurement appear to be shifted with respect to the reference data by 2.5 nm. This indicates the intrinsic error in calibration which is very likely in a delay–scanning system. It originates from a small noncollinear-

ity between the beams present in the scanned–length arm. The non–zero angle between these causes the reference He–Ne trace to have a different effectively recorded wavelength than it really has (Fig. 2.27). This misalignment is very difficult to eliminate, however the error itself is quite simple to remove with a measurement of a well–known spectrum, e.g. methane absorption lines. As a result of a changed effective He–Ne wavelength, the acquired data will be shifted in wavelengths by a constant, giving the effect visible in the comparison of the raw data without the calibration correction and the spectrum taken from a database (Fig. 2.26). The calibration then aims to remove the shift by adjusting the effective He–Ne wavelength so the absorption lines from both data sets overlap. In my case the new effective calibration wavelength was 632.3 nm, which is different from the real used wavelength by 0.5 nm, indicating the noncollinearity of $\alpha = 0.5°$. Subsequently this wavelength was used in the numerical retrieval of the idler spectra from the measured interferograms.

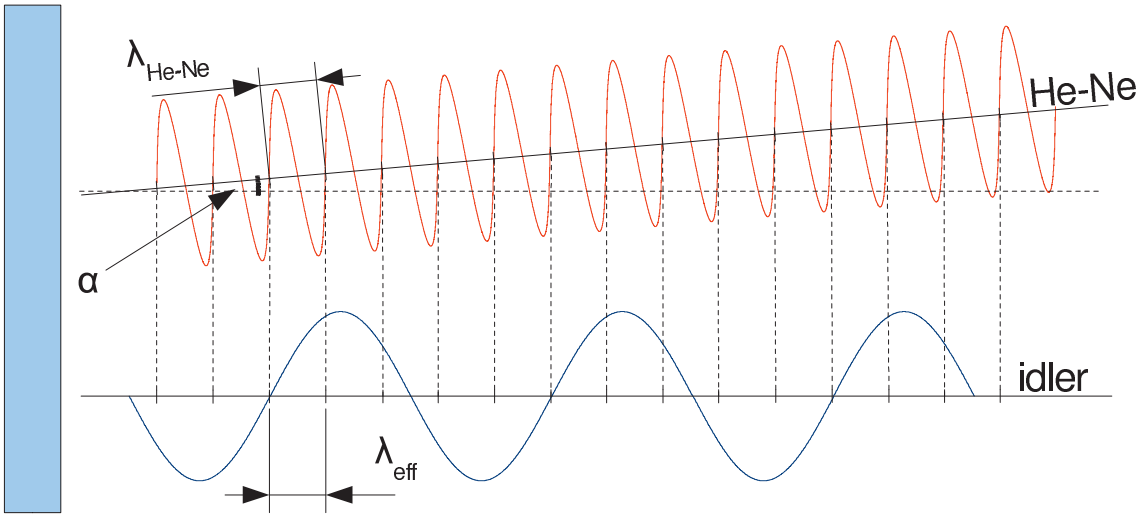

Figure 2.27: The effect of shortening of the calibration wavelength. The non–zero value of the angle between the beams in the interferometer α modifies the effective recorded reference wavelength to $\lambda_{\mathrm{EFF}} = \lambda_{\mathrm{He-Ne}} \times \cos(\alpha)$.

The absorption curve for the 5% results using the wavelength scale corrected for the noncollinearity effect is presented in Fig. 2.28.

Further measurements were taken for four methane concentrations in nitrogen, namely 5%, 1%, 0.5% and 0.1%. The results for all concentrations tested are shown together in Fig. 2.29. It is clear that the noise present in the IR beam, both in terms of spectrum centring and power fluctuations, makes it difficult to ex-

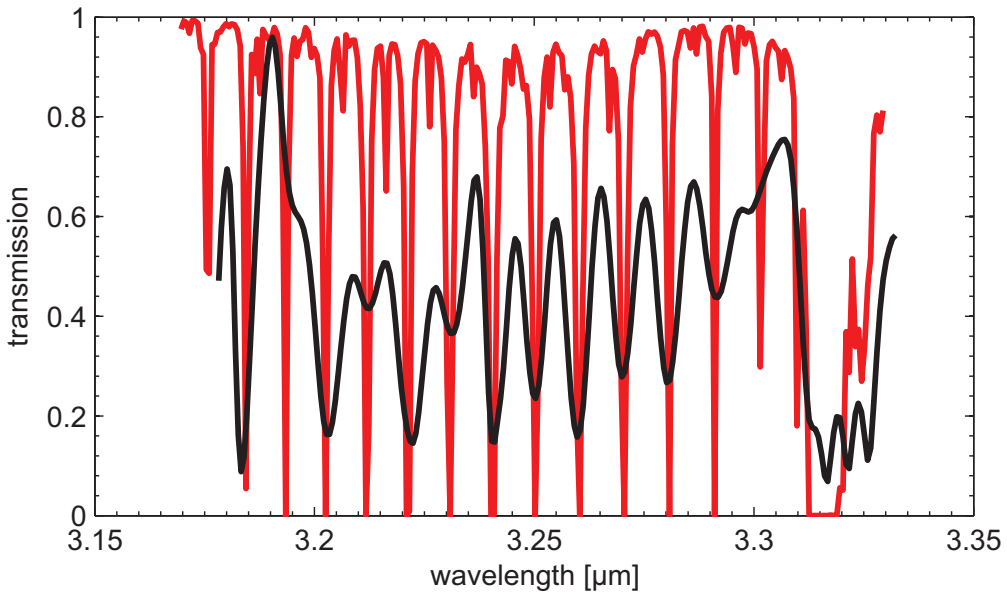

Figure 2.28: The calibrated result of 5% concentration measurement. The wavelength shift caused by the noncollinearity between the beams has been removed.

tend the applicability of the device to lower methane concentrations. The lack of simultaneously captured data from a reference channel introduces artifacts and washes out the absorption lines, even if in comparison with a simulated data, shown in Fig. 2.29, it is possible to find main features of the predicted curve. The Q–branch is well recognisable and corresponds to the theoretical shape down to 0.5% measurement.

The general assessment of the device performance based on the results would be that the sensitivity available is sufficient to measure even lower methane concentrations than 0.1% (especially taking into account the short fibre length applied), but the noise must be removed to make it possible. A similar detection scheme, but based on $2\nu_3$, was proposed recently [2.59] and the detection limit estimated there was 10 ppm (0.001%), but a 5 m–long fibre and a low–noise laser diode were used, so after employing longer fibre and decreasing noise in my experiment detectability of the order of 1 ppm should be possible due to the strong fundamental absorption.

Results were published in two journal articles [2.60,2.61] and presented at the CLEO 2007 conference [2.62].

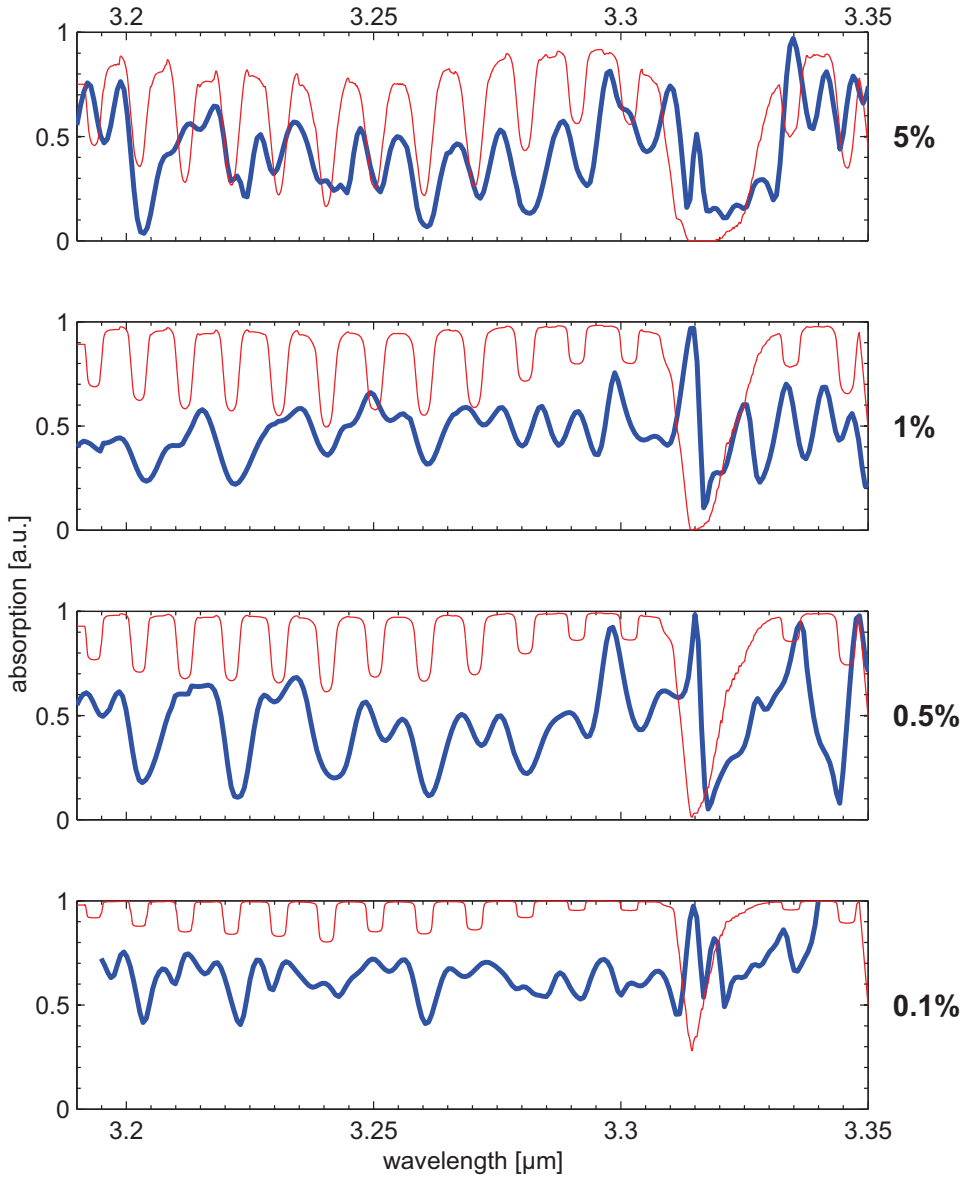

Figure 2.29: Comparison of methane absorption for different methane concentrations (numbers shown in the right side of each graph) are shown with the thick blue line. The thin red line shows the HITRAN data with the applied simulated resolution of 3.6 nm, equal to the estimated minimum resolution in the experiment.

2.10 Conclusions

This feasibility study experiment has shown the sensitivity of the apparatus and potential of methane sensing using the strongest fundamental absorption lines. The main sources of errors and noise were identified and solution is proposed.

The heavily structured spectral transmission profiles for the fibres we had available made the measurements very vulnerable to OPO detuning during data acquisition. The comparison of spectra after passing through nitrogen and methane assumes that incoming spectrum is constant and if it is not the case, the result may be very noisy due to the presence of small features and steep slopes in the fibre's transmission.

The OPO instability was caused principally by environmental changes that need to be controlled. This can be very difficult to achieve due to the required interferometric accuracy in the cavity length which is ruined by air currents which introduce into the beam path a medium containing both temporal and spatial variations of refractive index, which depends on temperature.

It is possible to eliminate both these sources of errors by a common mode rejection approach, and a sufficient solution would be to rebuild the detection system in a way shown in Fig. 2.30. A complicated spectral transmission profile would not be an issue any more since it is present in both idler traces and thus is automatically erased. OPO central wavelength fluctuations would be not important as well because the scan speed is common for both reference and sample fibres, so any uncontrolled detuning would happen at the same moment in both fibres, being rejected without any experimental effort.

Additionally, resolution in this home–built FTIR spectrometer was definitely not satisfactory. The lines were visible but enormously broadened. It was a proof–of–principle experiment, but there exist commercial solutions which could be applied on the next stage of development. However, even the home–built device could be improved if a longer scanning range was possible, which would immediately increase the resolution. There is still much to do in this particular issue as the theoretical derivation of the sampling requirements limits the scan amplitude to 39 mm while the loudspeaker allowed for only 2 mm amplitude. Additionally, the signal–to–noise ratio in the interferograms could be slightly increased

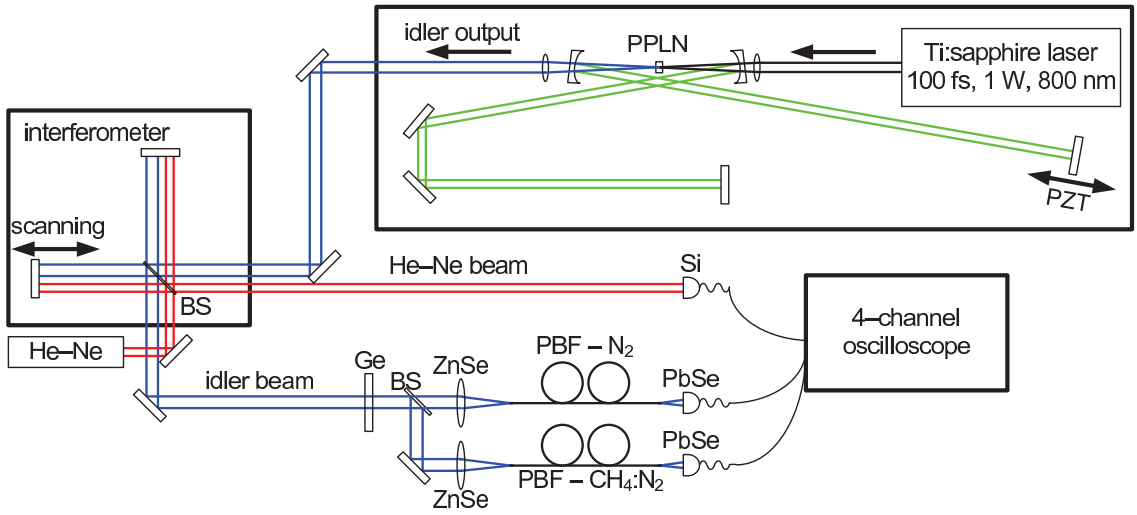

Figure 2.30: Suggested measurement setup which benefits from a common mode rejection. Two identical photodiodes detect the idler beam which was split into two and each copy is coupled into identical length of the same type of fibre. The only difference will be the cores' contents: the reference fibre contains nitrogen and the sample one is filled with appropriate methane mixture.

if the visibility of the fringes were better, and this could be achieved by using a beamsplitter dedicated for the idler wavelengths.

This technique can be potentially extended to other gases as the only modifications required would be tuning the light source into other wavelengths (however, e.g. in the case of ammonia it is already in the region of absorption) and preparing the fibre guiding this beam, which is generally possible as the knowledge about PBF modelling and engineering is developed very quickly in many centres across the world. Additionally, another aspect of this approach is valuable — the beam delivery to distant, possibly hazardous and inaccessible places. Not necessarily the entire length of the fibre has to be gas–sensitive, so for example one proposition would be to couple the light efficiently into the fibre and in the middle of its length arrange some means of sensing (possibly holes drilled in the cladding down to the core), depositing this ventilated section in the place of interest. However, the applicability of this depends on the availability of low–loss fibres operating at the spectral region of interest. A careful prediction would envisage the future of gas sensing devices in the marriage of broadband fem-

tosecond laser diodes and photonic bandgap fibres or alternatively Bragg fibres if these prove to have better characteristics for this purpose.

2.11 References

[2.1] K. Wiesner, H. Knozinger, M. Fleischer and H. Meixner, "Working mechanism of an ethanol filter for selective high–temperature methane gas sensors", *IEEE Sensors Journal* **2** (4), p. 354–359, 2002.

[2.2] P. Bhattacharyya, P. K. Basu, H. Saha and S. Basu, "Fast response methane sensor using nanocrystalline zinc oxide thin films derived by sol–gel method", *Sensors and Actuators B* **124**, p. 62–67, 2007.

[2.3] M. Vilaseca, J. Coronas, A. Cirera, A. Cornet, J. R. Morante and J. Santamaría, "Use of zeolite films to improve the selectivity of reactive gas sensors", *Catalysis Today* **82** (1–4), p. 179–185, 2003.

[2.4] E. Achaerandio, S. Jarabe, S. Abad and M. Lopez-Amo, "New WDM amplified network for optical sensor multiplexing", *IEEE Photonic Technology Letters* **11** (12), p. 1644–1646, 1999.

[2.5] P. S. J. Russell, "Photonic crystal fibers", *Science* **299** (5605), p. 358–362, 2003.

[2.6] P. W. Atkins, *Physical chemistry*, Oxford University Press, 3rd ed., 1987.

[2.7] H. Haken and H. C. Wolf, *Molecular physics and elements of quantum chemistry*, Springer–Verlag, 1995.

[2.8] W. W. Coblentz, *Investigations of infra–red spectra*, Carnegie Institution of Washington, 1905, p. 39.

[2.9] J. P. Cooley, "The infra–red absorption bands of methane", *Astrophysical Journal* **LXII** (2), p. 73–83, 1925.

[2.10] J. G. Moorhead, "The near infrared absorption spectrum of methane", *Physical Review* **39**, p. 83–88, 1932.

[2.11] R. C. Nelson, E. K. Plyler and W. S. Benedict, "Absorption spectra of methane in the near infrared", *Journal of Research of the National Bureau of Standards* **41** (RP1944), p. 615–621, 1948.

[2.12] L. S. Rothman, D. Jacquemart, A. Barbe, D. Chris Benner, M. Birk, L. R. Brown, M. R. Carleer, C. Chackerian Jr., K. Chance, L. H. Coudert, V. Dana, V. M. Devi, J.-M. Flaud, R. R. Gamache, A. Goldman, J.-M. Hartmann, K. W. Jucks, A. Maki, J.-Y. Mandin, S. T. Massie, J. Orphal, A. Perrin, C. P. Rinsland, M. A. H. Smith, J. Tennyson, R. N. Tolchenov, R. A. Toth, J. Vander Auwera, P. Varanasi and G. Wagner, "The HITRAN 2004 molecular spectroscopic database", *Journal of Quantitative Spectroscopy & Radiative Transfer* **96**, p. 139–204, 2005.

[2.13] J. U. White, "Long optical paths of large aperture", *Journal of the Optical Society of America* **32** (5), p. 285–288, 1942.

[2.14] D. Herriott, H. Kogelnik and R. Kompfner, "Off–axis paths in spherical mirror interferometers", *Applied Optics* **3** (4), p. 523–526, 1964.

[2.15] J. B. McManus, P. L. Kebabian and M. S. Zahniser, "Astigmatic mirror multipass absorption cells for long–path–lengths spectroscopy", *Applied Optics* **34** (18), p. 3336–3348, 1995.

[2.16] S. M. Chernin and E. G. Barskaya, "Optical multipass matrix systems", *Applied Optics* **30** (1), p. 51–58, 1991.

[2.17] A. O'Keefe and D. A. G. Deacon, "Cavity ring–down optical spectrometer for absorption measurements using pulsed laser sources", *Review of Scientific Instruments* **59** (12), p. 2544–2551, 1988.

[2.18] F. Benabid, F. Couny, J. C. Knight, T. A. Birks and P. S. J. Russell, "Compact, stable and efficient all–fibre gas cells using hollow–core photonic crystal fibres", *Nature* **434**, p. 488–491, March 2005.

[2.19] T. Ritari, J. Tuominen, H. Ludvigsen, J. C. Petersen, T. Sørensen, T. P. Hansen and H. R. Simonsen, "Gas sensing using air–guiding photonic bandgap fibers", *Optics Express* **12** (17), p. 4080–4087, 2004.

[2.20] C. J. Hensley, D. H. Broaddus, C. B. Schaffer and A. L. Gaeta, "Photonic band–gap fiber gas cell fabricated using femtosecond micromachining", *Optics Express* **15** (11), p. 6690–6695, 2007.

[2.21] A. Boschetti, D. Bassi, E. Iacob, S. Ianotta, L. Ricci and M. Scotoni, "Resonant photoacoustic simultaneous detection of methane and ethylene by means of a 1.63-μm diode laser", *Applied Physics B* **74** (3), p. 273–278, 2002.

[2.22] P. Werle and R. Kormann, "Fast chemical sensor for eddy–correlation measurements of methane emissions from rice paddy fields", *Applied Optics* **40** (6), p. 846–858, 2001.

[2.23] A. Grossel, V. Zeninari, L. Joly, B. Parvitte, D. Coourtois and G. Durry, "New improvements in methane detection using a Helmholtz resonant photoacoustic laser sensor: A comparison between near–IR diode lasers and mid–IR quantum cascade lasers", *Spectrochimica Acta Part A* **63** (5), p. 1021–1028, 2006.

[2.24] A. Nadezhdinskii, A. Berezin, O. Chernin, O. Ershov and V. Kutnyak, "High sensitivity methane analyzer based on tuned near infrared diode laser", *Spectrochimica Acta Part A* **55** (10), p. 2083–2089, 1999.

[2.25] M. Grau, C. Lin, O. Dier, C. Lauer and M.-C. Amann, "Room–temperature operation of 3.26 μm GaSb–based type–I lasers with quinternary AlGaInAsSb barriers", *Applied Physics Letters* **87** (24), p. 241104, 2005.

[2.26] C. Lin, M. Grau, O. Dier and M.-C. Amann, "Low threshold room–temperature continuous–wave operation of 2.24–3.04 μm GaInAsSb/AlGaAsSb quantum–well lasers", *Applied Physics Letters* **84** (25), p. 5088–5090, 2004.

[2.27] M. Aydaraliev, N. V. Zotova, S. A. Karandashov, B. A. Matveev, M. A. Remennyi, N. M. Stus, N. Talalakin, W. W. Bewley, J. R. Lindle and J. R. Meyer, "6 W InGaAsSb(Gd)/InAsSbP double–heterostructure diode lasers emitting at λ=3.3 μm", *Applied Physics Letters* **81** (7), p. 1166, 2002.

[2.28] A. Wilk, M. El Gazouli, M. El Skouri, P. Christol, P. Grech, A. N. Baranov and A. Joullié, "Type–II InAsSb/InAs strained quantum–well laser diodes emitting at 3.5 μm", *Applied Physics Letters* **77** (15), p. 2298, 2000.

[2.29] P. Werle and A. Popov, "Application of antimonide lasers for gas sensing in the 3–4-μm range", *Applied Optics* **38** (9), p. 1494–1501, 1999.

[2.30] D. Barat, J. Angellier, A. Vicet, Y. Roulliard, L. Le Gratiet, S. Guilet, A. Martinez and A. Ramdane, "Antimonide–based lasers and DFB laser diodes in the 2–2.7 µm wavelength range for absorption spectroscopy", *Applied Physics B* **90** (2), p. 201–204, 2008.

[2.31] C. R. Webster, R. D. May, C. A. Trimble, R. G. Chave and J. Kendall, "Aircraft (ER–2) laser infrared absorption spectrometer (ALIAS) for in–situ stratospheric measurements of HCl, N_2O, CH_4, NO_2, and HNO_3", *Applied Optics* **33** (3), p. 454–472, 1994.

[2.32] K. Fujita, S. Furuta, A. Sugiyama, T. Ochiai, T. Edamura, N. Akikusa, M. Yamanishi and H. Kan, "Room temperature, continuous–wave operation of quantum cascade lasers with single phonon resonance–continuum depopulation structures grown by metal organic vapor–phase epitaxy", *Applied Physics Letters* **91** (14), p. 141121, 2007.

[2.33] K. G. Hay, S. Wright, G. Duxbury and N. Langford, "In–flight measurements of ambient methane, nitrous oxide and water using a quantum cascade laser based spectrometer", *Applied Physics B* **90** (2), p. 329–337, 2008.

[2.34] C. R. Webster, G. J. Flesch, D. C. Scott, J. E. Swanson, R. D. May, W. S. Woodward, C. Gmachl, F. Capasso, D. L. Sivco, J. N. Baillargeon, A. L. Hutchinson and A. Y. Cho, "Quantum–cascade laser measurements of stratospheric methane and nitrous oxide", *Applied Optics* **40** (3), p. 321–326, 2001.

[2.35] C. Fischer, E. Sorokin, I. T. Sorokina and M. W. Sigrist, "Photoacoustic monitoring of gases using a novel laser source tunable around 2.5 µm", *Optics and Lasers in Engineering* **43** (3–5), p. 573–582, 2005.

[2.36] F. J. McAleavey, J. O'Gorman, J. F. Donegan, B. D. MacCraith, J. Hegarty and G. Mazé, "Narrow linewidth, tunable Tm^{3+}–doped fluoride fiber laser for optical–based hydrocarbon gas sensing", *IEEE Journal of Selected Topics in Quantum Electronics* **3** (4), p. 1103–1111, 1997.

[2.37] M. Murtz, D. Kleine, S. Stry, H. Dahnke, P. Hering, J. Lauterbach, K. Kleinermanns, W. Urban, H. Ehlers and D. Ristau, "Ultra–sensitive trace gas monitoring with a CW ring–down spectrometer", *Environmental Science and Pollution Research* (4), p. 61–67, 2002.

[2.38] D. G. Lancaster, D. Richter, R. F. Curl and F. K. Tittel, "Real–time measurements of trace gases using a compact difference–frequency–based sensor operating at 3.5 µm", *Applied Physics B* **67** (3), p. 339–345, 1998.

[2.39] P. Maddaloni, P. Malara, G. Gagliardi and P. De Natale, "Two–tone frequency modulation spectroscopy for ambient–air trace gas detection using a portable difference–frequency source around 3 µm", *Applied Physics B* **85** (2–3), p. 219–222, 2006.

[2.40] H. Y. Clark, L. Corner, W. Denzer, G. Hancock, A. Hutchinson, M. Islam, R. Peverall and G. A. D. Ritchie, "Difference frequency generation in periodically poled lithium niobate and its use in the detection of atmosphere methane", *Chemical Physics Letters* **399** (1–3), p. 102–108, 2004.

[2.41] D. G. Lancaster, R. Weidner, D. Richter, F. K. Tittel and J. Limpert, "Compact CH_4 sensor based on difference frequency mixing of diode lasers in quasi–phasematched $LiNbO_3$", *Optics Communications* **175** (4–6), p. 461–468, 2000.

[2.42] A. K. Y. Ngai, S. T. Persijn, G. von Basum and F. J. M. Harren, "Automatically tunable continuous–wave optical parametric oscillator for high–resolution spectroscopy and sensitive trace–gas detection", *Applied Physics B* **85** (2–3), p. 173–180, 2006.

[2.43] K. A. Tillman, R. R. J. Maier, D. T. Reid and E. D. McNaghten, "Mid–infrared absorption spectroscopy of methane using a broadband femtosecond optical parametric oscillator based on aperiodically poled lithium niobate", *Journal of Optics A* **7**, p. S408–S414, 2005.

[2.44] E. U. Rafailov, M. A. Cataluna and W. Sibbett, "Mode–locked quantum–dot lasers", *Nature Photonics* **1** (7), p. 395–401, 2007.

[2.45] R. R. Alfano and S. L. Shapiro, "Observation of self–phase modulation and small–scale filaments in crystals and glasses", *Physical Review Letters* **24** (11), p. 592–594, 1970.

[2.46] J. D. Shephard, W. N. MacPherson, R. R. J. Maier, J. D. C. Jones, D. P. Hand, M. Mohebbi, A. K. George, P. J. Roberts and J. C. Knight, "Single–mode mid–

IR guidance in a hollow–core photonic crystal fiber", *Optics Express* **13** (18), p. 7139–7144, 2005.

[2.47] E. V. Loewenstein, "The history and current status of Fourier transform spectroscopy", *Applied Optics* **5** (5), p. 845–854, 1966.

[2.48] C. E. Shannon, "Communication in the presence of noise", *Proceedings of the Institute of Radio Engineers* **37** (1), p. 10–21, 1949.

[2.49] B. Temelkuran, S. H. Hart, G. Benoit, J. D. Joannopoulos and Y. Fink, "Wavelength–scalable hollow optical fibres with large photonic bandgaps for CO_2 laser transmission", *Nature* **420**, 2002.

[2.50] K. Kuriki, O. Shapira, S. Hart, G. Benoit, Y. Kuriki, J. Viens, M. Bayindir, J. Joannopoulos and Y. Fink, "Hollow multilayer photonic bandgap fibers for NIR applications", *Optics Express* **12** (8), p. 1510–1517, 2004.

[2.51] P. S. J. Russell, "Photonic–crystal fibers", *IEEE Journal of Lightwave Technology* **24** (12), p. 4729–4749, 2006.

[2.52] P. J. Roberts, F. Couny, H. Sabert, B. J. Mangan, D. P. Williams, L. Farr, M. W. Mason, A. Tomlinson, T. A. Birks, J. C. Knight and P. S. Russell, "Ultimate low loss of hollow–core photonic crystal fibres", *Optics Express* **13** (1), p. 236–244, 2004.

[2.53] F. Luan, J. C. Knight, P. S. J. Russell, S. Campbell, D. Xiao, D. T. Reid, B. J. Mangan, D. P. Williams and P. J. Roberts, "Femtosecond soliton pulse delivery at 800 nm wavelength in hollow–core photonic bandgap fibers", *Optics Express* **12** (5), p. 835–840, 2004.

[2.54] K. Cook, C. Xiong and W. J. Wadsworth, "Enhanced four–wave mixing and parametric oscillation in photonic crystal fibre", *Journal of Optics A* **9**, p. 1095–1099, 2007.

[2.55] S. O. Konorov, A. M. Zheltikov and M. Scalora, "Photonic–crystal fiber as a multifunctional optical sensor and sample collector", *Optics Express* **13** (9), p. 3454–3459, 2005.

[2.56] J. Limpert, T. Schreiber, S. Nolte, H. Zellmer and A. Tünnermann, "All fiber chirped–pulse amplification system based on compression in air–guiding photonic bandgap fiber", *Optics Express* **11** (24), p. 3332–3337, 2003.

[2.57] M. Nisoli, S. De Silvestri and O. Svelto, "Generation of high energy 10 fs pulses by a new pulse compression technique", *Applied Physics Letters* **68** (20), p. 2793–2795, 1996.

[2.58] J. C. Knight and D. V. Skryabin, "Nonlinear waveguide optics and photonic crystal fibers", *Optics Express* **15** (23), p. 15365–15376, 2007.

[2.59] A. M. Cubillas, M. Silva-Lopez, J. M. Lazaro, O. M. Conde, M. N. Petrovich and J. M. Lopez-Higuera, "Methane detection at 1670–nm band using a hollow–core photonic bandgap fiber and a multiline algorithm", *Optics Express* **15** (26), p. 17570–17576, 2007.

[2.60] Ł. Kornaszewski, N. Gayraud, J. M. Stone, W. N. MacPherson, A. K. George, J. C. Knight, D. P. Hand and D. T. Reid, "Mid–infrared methane detection in a photonic bandgap fiber using a broadband optical parametric oscillator", *Optics Express* **15** (18), p. 11219–11224, 2007.

[2.61] N. Gayraud, Ł. W. Kornaszewski, J. M. Stone, J. C. Knight, D. T. Reid, D. P. Hand and W. N. MacPherson, "Mid-infrared gas sensing using a photonic bandgap fiber", *Applied Optics* **47** (9), p. 1269–1277, 2008.

[2.62] Ł. W. Kornaszewski, N. Gayraud, W. N. MacPherson, D. P. Hand, D. T. Reid, J. M. Stone, A. K. George and J. C. Knight, "Mid–infrared methane sensing using an optical parametric oscillator and a photonic bandgap fiber as a gas cell", in *Conference on Lasers and Electro–Optics/Quantum Electronics and Laser Science Conference and Photonic Applications Systems Technologies 2007 Technical Digest*, p. CThO3, (Optical Society of America, Washington, DC), 2007.

Chapter 3

Design and construction of a high–energy femtosecond optical parametric oscillator for silicon material processing

3.1 Motivation and background – femtosecond material processing

Micromachining using laser beams offers the capability to produce ablated features with sizes of less than 1 µm [3.1]. Especially systems offering ultrashort pulses are very suitable here because thermal effects are kept to a minimum due to the short exposure times and plasma–assisted material removal. In metals absorption of intense light delivered in the time–scale much shorter than the heat transfer mechanisms allows localised ablation of the sample in the place of the laser focus without affecting neighbouring areas. In dielectrics, this technique is even more versatile because not only the surface ablation mode by absorption of the laser beam can be used but also transparent samples may be processed by means of multi–photon (nonlinear) absorption. This technique localises the machining area to the spots smaller than the focus size and, moreover, not necessarily on the surface. Processing of bulk material in 3D geometry without modifying the surface is available and in this approach there is no material removal but only refractive index modification which is the way to direct waveguide writing.

In the early work of Hill and co–workers, fibre Bragg mirrors were fabricated with the use of an argon laser. The quality was sufficient to use such a mirror as an output coupler in the same Ar^+ laser [3.2]. However, the process responsible for the structure formation in the glass was not a result of intense focusing but rather was caused by an intensity grating created by two counter–propagating laser beams. The photosensitive material, which in that case was a Ge–doped silica fibre, was permanently inscribed with a reflective Bragg grating.

When it comes to the ablation regime, the mechanism responsible for the machining process is the plasma formation caused by a rapid excitation of the electrons at the material surface. Plasma is subsequently removed from the interaction area by evaporation. The pulse duration and the material properties dictate the conditions and the machining quality — high temperatures obtained can cause defects, melting and unwanted expansion even at the regions far from the focus. There are two general regimes: ablation in metals and dielectrics.

The first reported metal–related calculations supported by experiments date back to 1965, when microsecond– and nanosecond–scale pulses were used in testing thermal effects on several metal samples [3.3]. Pulse lengths available at the time did not allow for considering non–thermal interactions as the mean free electron–electron collision time in conductors is of the order of 10-100 fs. Pulses longer than that deposit the energy in the lattice through the heat transfer from initially excited free electrons, but if the pulse duration is shorter than hundreds of femtoseconds, then thermal diffusivity is strongly decreased due to the high electron temperature caused by high laser light intensity and electrons can leave the focal area prior to interacting with the lattice. The pulse duration must be short in order to obtain a clean cut in a metal sample because otherwise excited electrons can move freely from the focal region and either collide with other electrons exchanging energy with them, or even be replaced by cold electrons from outside and diffuse into the surrounding areas, warming up the metal and causing thermal expansion.

In dielectrics there are not many free electrons and the plasma formation relies mainly on multiphoton ionisation. Avoiding heat transfer is not that important as it is in the case of metals because excited electrons cannot freely diffuse from the plasma region and exchange energy with the surrounding areas. For example, multiphoton absorption in PTFE was shown to lead to clean edge ablation when

a femtosecond UV excimer laser was used [3.4]. However, it is not always the case that dielectrics ablation results in clean edges because no melting occurs and sometimes rough surface is left on the edges of the machined material. As another example, femtosecond dye–based oscillators were sources of short enough pulses to apply the nonlinear absorption in processing of various materials, including skin cells [3.5], cornea [3.6] and silicon [3.7].

Ti:sapphire amplifiers have become the new standard sources for machining of optically transparent materials by nonlinear processes. Early experiments included a thorough comparative analysis of different pulse durations and their corresponding mechanisms of laser breakdown in fused silica [3.8] and calcium fluoride [3.9]. Also metallic substrates were successfully machined and their behaviour under exposure to the laser beam tested, including gold [3.10] and silver [3.11].

A nonlinear absorption in transparent targets opens the path for 3D machining in the bulk material. The physical mechanism in this case is similar to surface ablation, but the evaporation of the high–temperature material is not possible. It resolidifies and subsequently can form small density or structural variation, leading to altered medium properties, for example refractive index changes. For more intense pulses the process may be more violent and cause structural damage by explosive expansion. The index modification regime is especially attractive when it comes to direct waveguide inscription in which, under favourable conditions, a track of a uniformly index–enhanced material may be created in the bulk of a sample when suitable scanning of the focal position is performed.

The first successful waveguide writing in glass by refractive index modification with a Ti:sapphire amplifier was reported in 1996 [3.12]. Subsequently femtosecond–laser inscribed media were used as waveguide host materials for signal amplification or laser action: Er:glass [3.13], Nd:YAG [3.14] and Ti:sapphire [3.15]. Additionally successful waveguide creation in highly nonlinear crystals was demonstrated: $LiNbO_3$ [3.16] and KTP [3.17,3.18].

In the high–power approach, an interesting experiment creating a waveguide by introducing a strain field between two parallel damage trenches was presented by Burghoff and co–workers [3.19], offering very clean mode shapes (Fig. 3.1). If there is only one damage field, two strain fields are created and they can guide light, however the efficiency is limited due to the edge of the cross–section, where

the guided mode partially overlaps with the damage area. If two trenches are made with a carefully chosen distance between them, the shared strain field offers a much cleaner mode and more efficient guiding. This method is planned to be tested in future with the laser system described in this chapter.

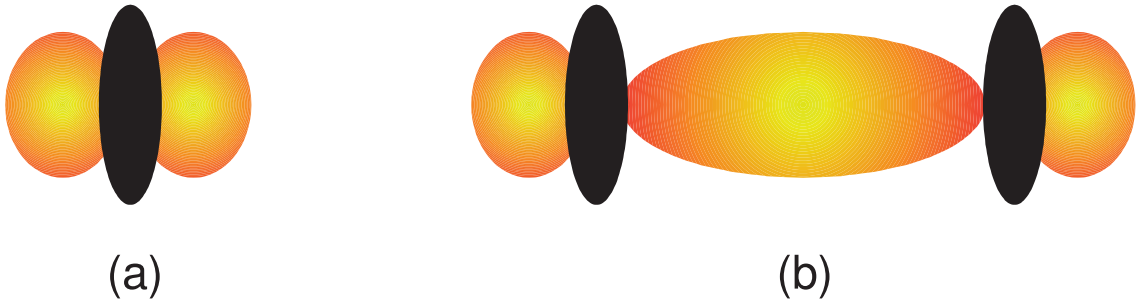

Figure 3.1: A schematic structure of a cross–section of a waveguide written by a femtosecond laser. The black fields symbolise the damage regions, which are surrounded by strain fields. The case (a) is less efficient than the case (b) due to the close neighbourhood of the damage region.

For more detailed and systematic analysis of the femtosecond machining physics and technology, see [3.20].

3.1.1 The work outline

Waveguides created in bulk silicon and in silicon–on–insulator samples are a specially attractive perspective and promise a simple integration with electronic devices. This project was planned as a construction of the powerful OPO source needed for second–order absorption experiments in silicon. The OPO was built and its performance tested. The next steps will be energy scaling via its modification to a cavity–dumped device, and systematic tests of waveguide inscription in silicon for various parameters.

To create waveguides in silicon a powerful laser working at the wavelengths longer than the absorption edge of silicon (1.1 µm) is needed. The idea behind this experiment was to use a fibre–based amplifier to pump an OPO tunable in the region of 1.3–1.5 µm corresponding to silicon's 2–photon absorption regime. The PPLN crystal was designed and purchased and used to construct an OPO based on a commercial Yb:fibre oscillator–amplifier. The pump laser was also obtained commercially and the OPO was built in the laboratory. The operating character-

istic of the OPO output were measured and additionally an OPO simulation code was developed.

3.2 Pump laser characterisation

The design of a femtosecond optical parametric oscillator requires detailed knowledge of the pump laser characteristics – both temporal and spatial. The pump pulse profile should be matched to the crystal grating structure in a way so that it can be optimally depleted and the highest output power obtained. The beam profile must also be known before designing the oscillator cavity, taking into account the pump focusing characteristics while designing the crystal and the resonator focusing around it.

The pump laser we decided to use was a commercially available sub–picosecond FemtoPower1060–10 (Fianium [3.21]) working at the central wavelength of 1064 nm. The specified average power P_{AVG} can be adjusted from 0 to 11 W, and the nominal pulse duration Δt is 7 ps but is compressible to $\approx$ 400 fs. The repetition frequency f is 15 MHz, which gives the expected values of the maximum pulse energy:

$$E_{PULSE} = \frac{P_{AVG}}{f} = \frac{11\ \mathrm{W}}{15\ \mathrm{MHz}} = 0.733\ \mu\mathrm{J} \tag{3.1}$$

and maximum peak power for these chirped pulses:

$$P_{PULSE} = \frac{E_{PULSE}}{\Delta t} = \frac{0.733\ \mu\mathrm{J}}{7\ \mathrm{ps}} = 105\ \mathrm{kW}. \tag{3.2}$$

3.2.1 Repetition frequency

The repetition frequency was measured with a photodiode and oscilloscope. Directly reading the temporal distance between intensity peaks on the oscilloscope screen gave 15.31 MHz, equivalent to 9.791 m of free–space cavity length.

An independent check was performed with a radio frequency analyser and a more precise result was obtained, namely 15.307 MHz, for which a corresponding cavity length is 9.793 m.

3.2.2 Spectra for different output powers

The pump laser is built as an amplifier using an ytterbium–doped fibre to increase the pulse bandwidth by a self-phase modulation process. This means that the spectral shape depends on the power set at the output, which is itself dependent on the amplifier gain. I measured the spectra as a function of average output power and they are shown in Figure 3.2. The heavily structured shape is the classic signature of a self–phase–modulation.

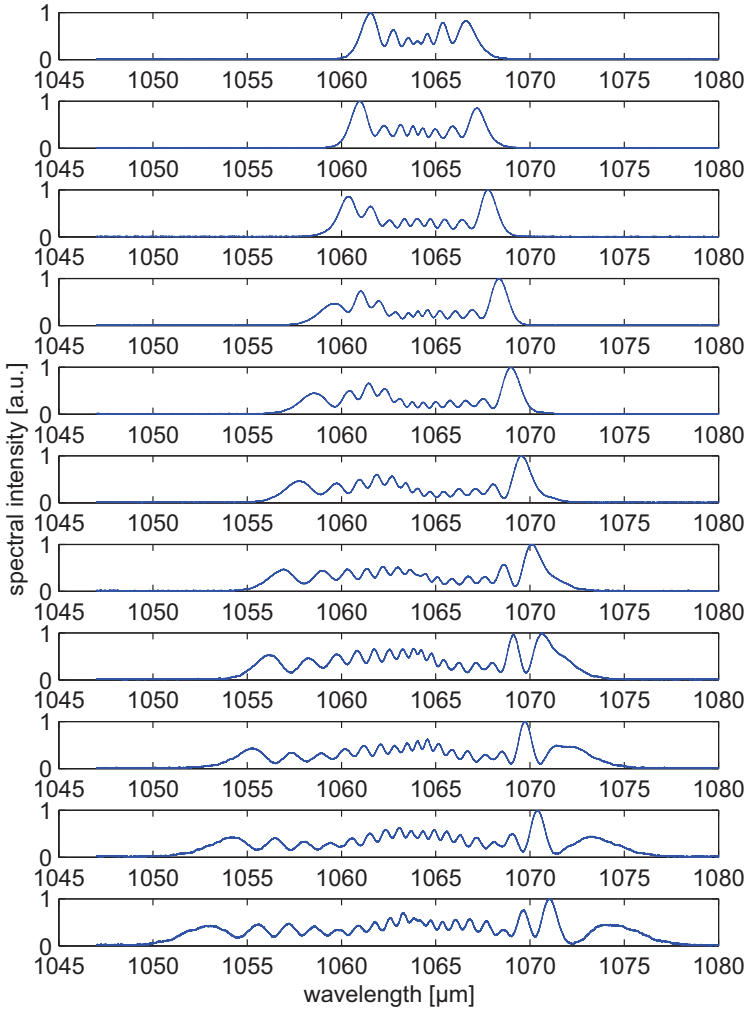

Figure 3.2: Spectra of the pump laser as a function of output power. The graphs correspond to the measured spectra for the output power in the range 1–11 W, in 1 W steps. Top graph: 1 W, bottom graph: 11 W. The width increases with the power as expected.

This spectral behaviour is unavoidable and means that the full power of the amplifier must be used whenever a broad spectrum is desired. Even if the power needed is small, it must be obtained through an attenuation of the full output power in order to ensure identical performance at all power levels.

3.2.3 Temporal characteristics and compression scheme

Generally, in a generation scheme like this, a pulse will have a different temporal structure at each different output power. Even if the intensity profile remains the same, the complex field may be unique for different spectra. To find the full electric–field values containing the optical phase, I used the FROG technique. All eleven maps are shown together in a Figure 3.3.

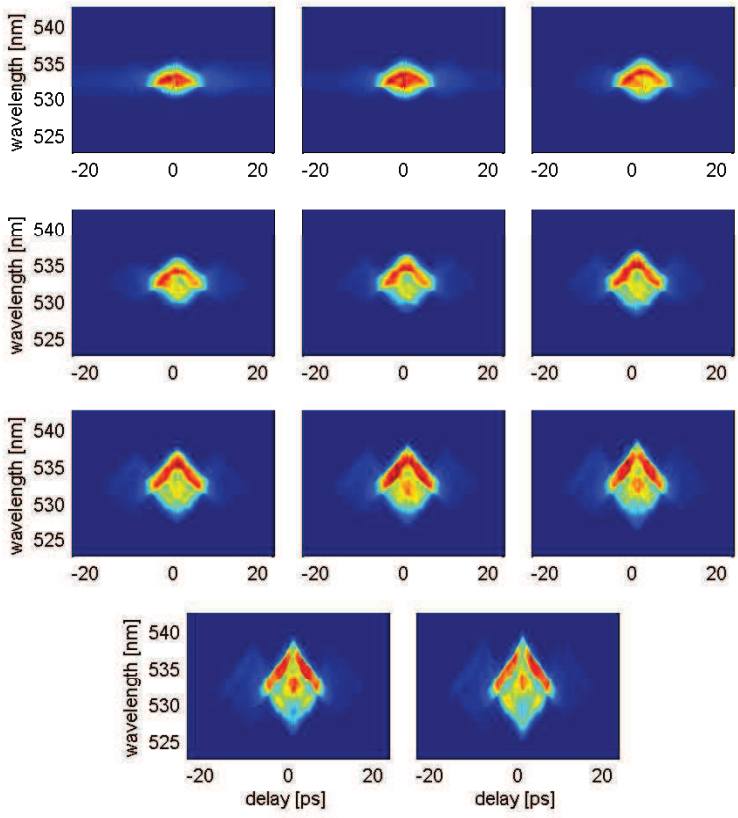

Figure 3.3: Direct results of a non–compressed pulse measurement using a SH–FROG technique. These maps span 20 nm in wavelengths and 48.3 ps in delay. Qualitatively it can be quickly estimated that pulses do not change their duration but only spectral width for different output powers.

The FROG traces were used for an attempted retrieval of the pulses, however it was difficult to find proper and reliable results due to the huge $\Delta\tau\Delta\omega$ factor and limited experimental spectral resolution. The resampling requirements caused the data matrices to be very big and the computations were time–consuming. The principal component generalised projections algorithm struggled to converge and was not stable even for the narrow spectra. Anyway, the essence of the measurement was the confirmation of the fact that the spectrum broadened for increasing power but the duration stayed the same.

The part of the future project was a test of the OPO performance for various crystals and pump pulse durations. To facilitate this, I built a compression section consisting of two fused silica transmission gratings (Ibsen Photonics [3.22]). The gratings were optimised for the central wavelength of 1064 nm, vertical light polarisation and the first diffraction order (Littrow configuration) so the transmission efficiency after a single pass of one grating was 94%. The complete double–pass system is shown in Fig. 3.4. The overall transmission of this section was measured to be 75%.

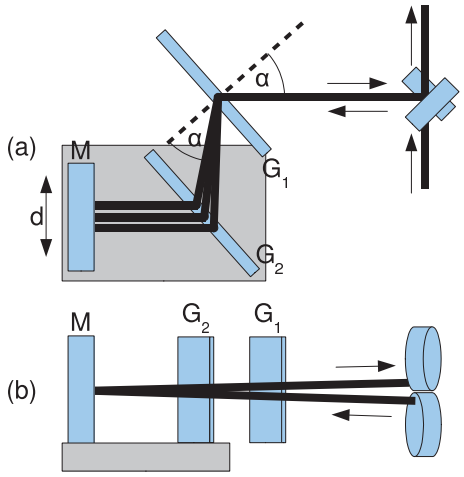

Figure 3.4: The grating compressor. (a): top view, (b): side view. The gratings were used in a Littrow configuration, i.e. when the incident angle is equal to the diffraction angle, here $\alpha = 41.7°$. G_1, G_2: fused silica transmission gratings (Ibsen Photonics), M: dielectric mirror, HR at 1064 nm. To allow variable compression the grating G_2 and the mirror M were mounted together on a translation stage (grey box) so the distance between the gratings d could be adjusted without any major disturbance of the pump beam direction. The beam height differences at the input and the output are shown.

After building the compression section, I measured the autocorrelation functions for different grating distances in steps of 2 mm to evaluate the compression ratio available with the broadest spectrum, at 11 W. The results are shown in Fig. 3.5.

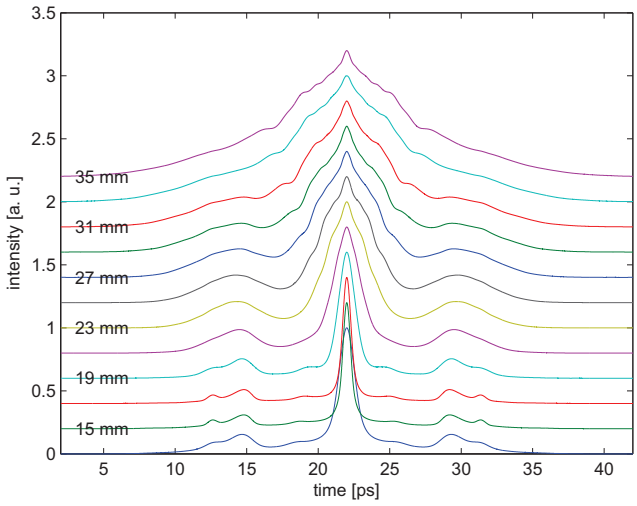

Figure 3.5: The autocorrelation functions for different grating distances (as given on the left–hand side in millimetres). The optimal compression occurred for quite a short distance of the order of 15 mm and the longer distances indicate negatively–chirped pulses.

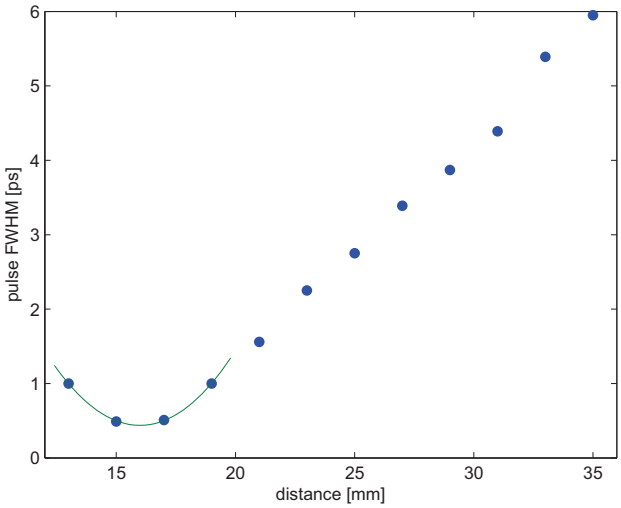

Figure 3.6: The duration of the compressed pulses with an assumption of a Gaussian pulse shape. The green curve is a 2nd degree polynomial fit to the four points around the minimum and the estimated minimum value is 437 fs.

Further analysis of the autocorrelation function FWHM, and using the Gaussian deconvolution factor of $\sqrt{2}$, led to the graph showing the estimated pulse duration as a function of the distance between gratings $\tau(l)$, presented in Fig. 3.6. Due to the mounting constraints it was not possible to achieve a better compression ratio. In the region of the minimum of the $\tau(l)$ curve the parabolic fit was done leading to an estimated minimum value of 437 fs.

3.2.4 Pump beam profile measurement

The pump beam profile was measured in order to find the complex beam parameter which could be used later in the simulations of propagation through various optical components.

The complex parameter q contains the full information about two independent values: the beam radius w, defined here as the second–order moment of the intensity distribution, and the wavefront radius of curvature R [3.23, 3.24]:

$$\frac{1}{q} = \frac{1}{R} - i\frac{\lambda M^2}{\pi w^2}. \tag{3.3}$$

The M^2 value is the measure of the beam quality. $M^2 = 1$ means that the beam is of the ideal Gaussian shape, $M^2 > 1$ means the quality is worse. The M^2 value describes the quality and size of the beam focus, which is a very important problem in the situation of the pumping of an oscillator.

The q and M^2 measurement method is based on finding the beam radius w in different points along the beam and fitting the functional dependence of the form:

$$w(z) = w_0 \sqrt{1 + \left(\frac{zM^2}{z_0}\right)^2}, \tag{3.4}$$

where z is the distance measured along the beam, z_0 is the position of the focus, and w_0 is the beam radius in the focus. After finding the w_0, the beam parameter at the focus $q(z_0)$ is known because the real term $1/R(z_0) = 0$, by definition. The M^2 value is important in any propagation simulations because a clean Gaussian beam with $M^2 = 1$ diverges less quickly than beams with $M^2 > 1$.

The standard approach for evaluating M^2 is to measure the beam width as the beam passes through a focus created using a lens of known focal length. The data used in the fitting procedure and the resulting curves fitted to Eq. 3.4 are shown in Fig. 3.7. A $f = 5$ cm lens was positioned in the beam and this was the

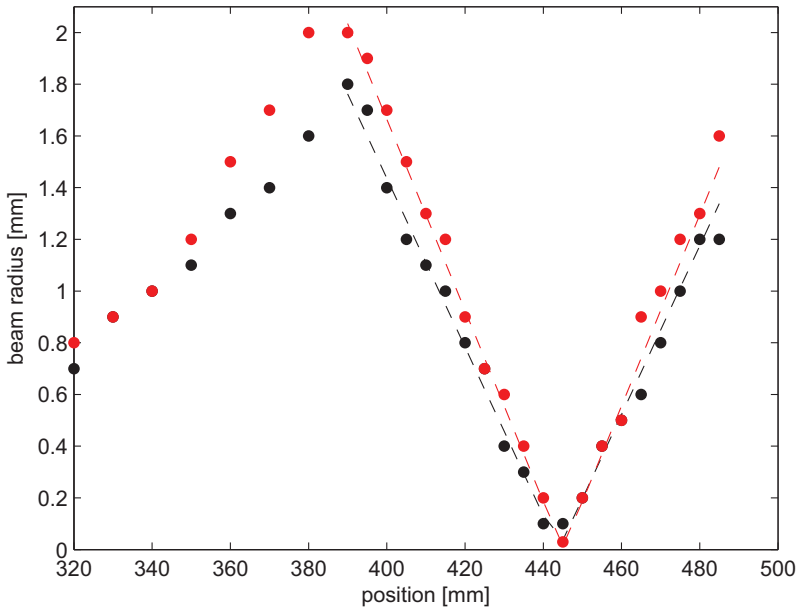

Figure 3.7: The data used to find the beam complex parameter. The beam is slightly astigmatic. The red colour corresponds to the vertical plane and the black colour to the horizontal plane. Dots indicate the measurement points and the dashed lines are the analytical curves fitted to the data collected after the $f = 5$ cm lens.

region used for the fitting procedure, rather than the laser output area. The fitting was performed with the Origin™ program. There was some uncertainty in the determination of M^2 and the focus size w_0 as these are highly dependent values, and $M^2 = 1.28$ as stated by the manufacturer was chosen to be the trusted value.

The knife–edge method of the beam radius w measurement was used. It is based on the fact that partially blocking the beam with an edge and measuring the transmitted power gives the integral value:

$$\int_{-\infty}^{+\infty} dy \int_{x_{\mathrm{CUT}}}^{+\infty} dx\, I(x,y), \tag{3.5}$$

which — when measured for a sufficiently large number of different x_{CUT} points (practically 20–30) — can be differentiated to yield the beam shape $I(x,y)$. For the purpose of this experiment I prepared an automated apparatus consisting of a Newport NewStep™ motor and an oscilloscope. The motion and data acquisition was operated from the National Instruments LabVIEW™ environment. The motor incrementally pushed the translation stage with the knife edge mounted

on it and the photodiode measured the relative total light intensity of the focused beam. For the situation of the partially blocked beam, the intensity was smaller and the signal fell to zero as more of the beam was obscured. By means of the numerical differentiation within the program, the sampled $I(x, y)$ profile was calculated and then the generalised beam radius w [3.24], defined as the second–order moment, was calculated using:

$$w = 2\sqrt{\frac{\sum(x_i - x_0)^2 \cdot I_i}{\sum I_i}}, \tag{3.6}$$

where x_0 is the centre of the beam, defined as the first–order moment of the intensity distribution:

$$x_0 = \frac{\sum (x_i \cdot I_i)}{\sum I_i}. \tag{3.7}$$

Having found the q parameter I developed a numerical model of the pump beam propagating in a free space, then transmitted through a lens and a cavity mirror to determine the available focus sizes. The model was based on the ABCD matrices formalism. The pump beam radius w evaluated in the model is shown in Fig. 3.8.

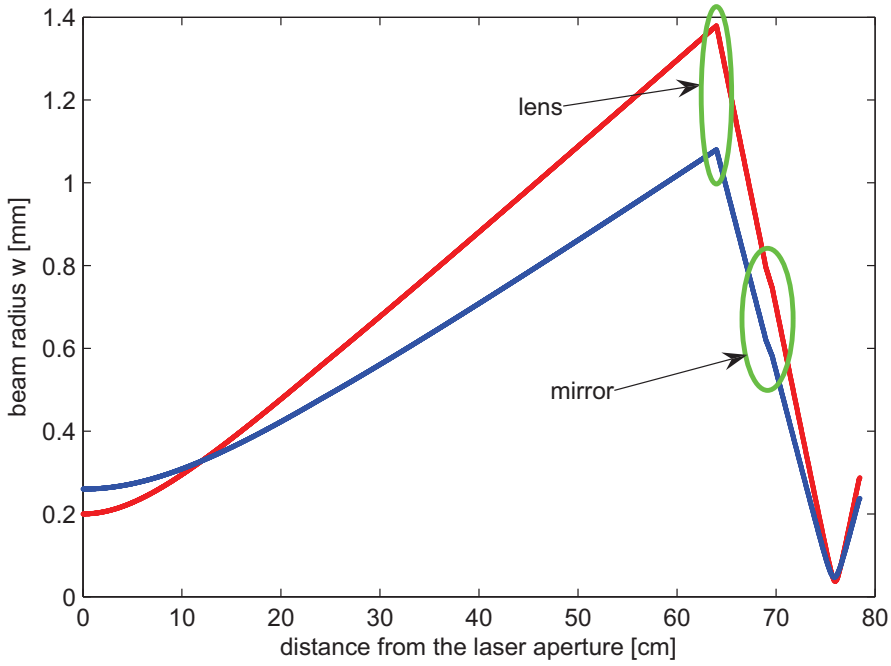

Figure 3.8: The result of calculations of the pump beam propagation through a free space, a lens and a cavity mirror. The blue line denotes the vertical plane, the red one the horizontal plane.

The model showed it was possible to manipulate the beam radius w by varying the distance between the laser output aperture and the lens, as the beam was not collimated. The value of $w = 40$ µm was chosen to be the target focus size since this was achievable in terms of the intracavity OPO focal size and was sufficiently large to minimise the risk of damage.

3.3 Crystal design

When the target signal wavelength was known, then the PPLN crystal period had to be calculated using its refractive index. The crystal was 5% MgO–doped and the temperature–dependent extraordinary refractive index equation was supplied by the manufacturer (HC Photonics [3.25]), based on their material data:

$$n_e(\lambda, T) = \frac{\sqrt{B + H \cdot X + \dfrac{C + I \cdot X}{\lambda^2 - (D + J \cdot X)^2} + \dfrac{E + K \cdot X}{\lambda^2 - F^2} - G \cdot \lambda^2}}{L - M \cdot T}, \tag{3.8}$$

where the symbols are explained in Tab. 3.1.

The standard approach of presenting the OPO theoretical tunability is to plot the process conversion efficiency as a function of the grating period and the signal wavelength. The wavevector mismatch in the collinear optical parametric oscillation process is:

$$\Delta k = 2\pi \left(\frac{n_\mathrm{P}}{\lambda_\mathrm{P}} - \frac{n_\mathrm{S}}{\lambda_\mathrm{S}} - \frac{n_\mathrm{I}}{\lambda_\mathrm{I}} - \frac{1}{\Lambda} \right), \tag{3.9}$$

where P, S, I denote the pump, signal and idler, respectively, n_P, n_S and n_I are their extraordinary refractive indices, Λ is the grating period, and λ_P, λ_S and λ_I are their wavelengths related to each other by:

$$\frac{1}{\lambda_\mathrm{P}} = \frac{1}{\lambda_\mathrm{S}} + \frac{1}{\lambda_\mathrm{I}}. \tag{3.10}$$

The efficiency of the nonlinear process depends on the wavevector mismatch Δk and the crystal length L:

$$P_\mathrm{OUT} \sim \left[\frac{\sin(\Delta k \cdot L/2)}{\Delta k \cdot L/2} \right]^2 = \mathrm{sinc}^2 \left(\frac{\Delta k \cdot L}{2} \right). \tag{3.11}$$

The plot of $\mathrm{sinc}^2(\Delta k \cdot L/2)$ for different gratings and in a broad tuning range is shown in Fig. 3.9.

Following these calculations a set of crystals was designed, and the one which was used to build the OPO is schematically presented in Fig. 3.10.

Table 3.1: Refractive index constants for MgO:PPLN as supplied by HC Photonics and used in Eq. 3.8.

λ	wavelength [µm]
T	temperature [°C]
B	5.35583
C	0.100473
D	0.20692
E	100
F	11.34927
G	0.015334
H	0.0000004629
I	0.00000003862
J	−0.0000000089
K	0.00002657
L	1.01813847
M	0.0000000813965809
X	$(T - 23.5) \cdot (T + 569.5)$

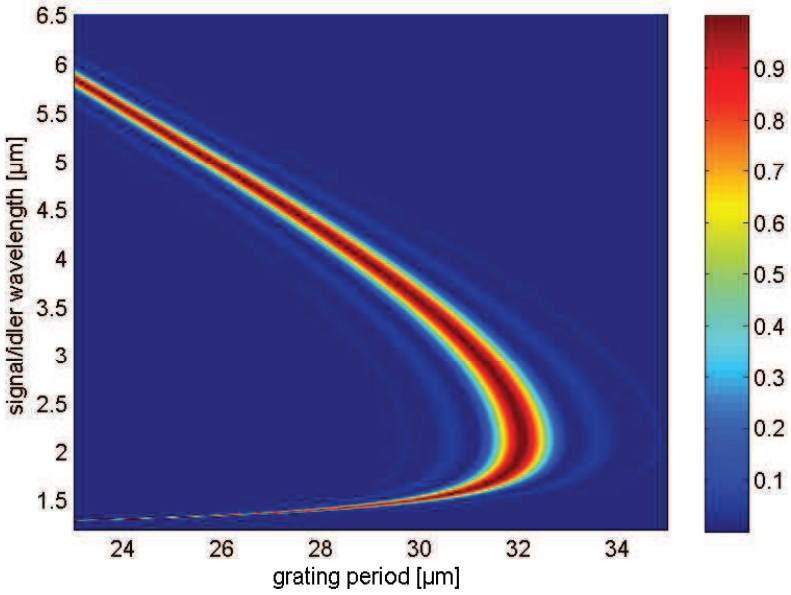

Figure 3.9: The OPO tunability range calculated using the refractive index equation for MgO:PPLN (3.8) and a 1 mm crystal length.

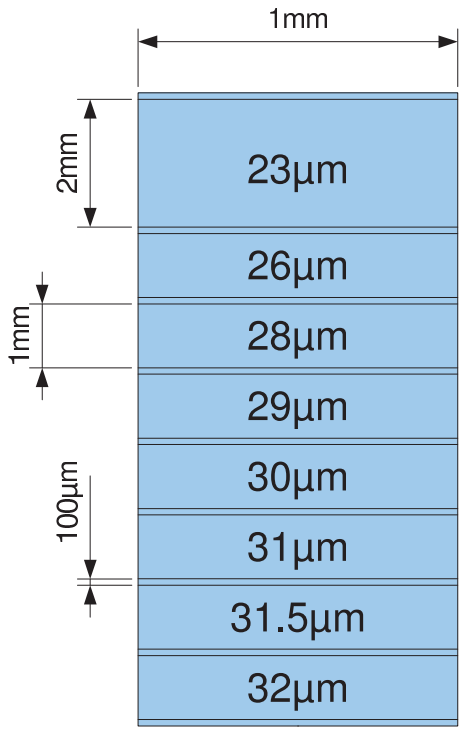

Figure 3.10: The MgO:PPLN crystal design. The numbers denote to the grating periods. The thickness was 0.5 mm.

3.4 Cavity design

The oscillator was designed as a synchronously–pumped device so the cavity length corresponded exactly to the pump laser repetition rate and equalled 9.79 m.

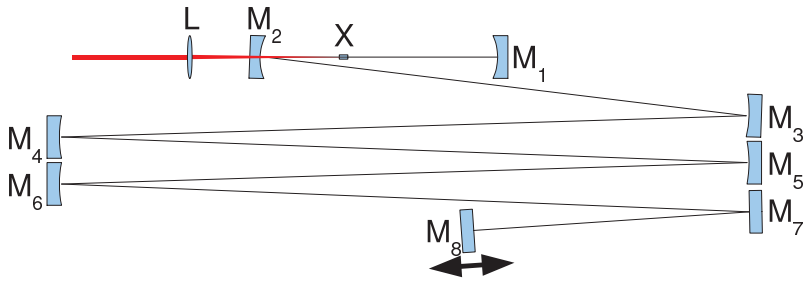

Figure 3.11: The OPO cavity design. L: AR–coated f=100 mm lens, M_1: R=300 mm mirror, M_2: R=200 mm mirror, M_3–M_6: R=2000 mm mirrors, M_7–M_8: plane mirrors. All the mirrors were HR–coated for the wavelengths 1250–1550 nm. X: 1 mm–long PPLN crystal with grating periods ranging from 23–32 µm. The red beam indicates the pump. Mirror M_8 was mounted on a translation stage for precise cavity–length adjustment, needed for the initial alignment and later tuning.

To avoid large beam sizes due to the divergence we used relay imaging. The exact layout of the cavity mirrors and the distances between them is presented in Fig. 3.11.

The OPO signal mode shape was calculated using the LCAV program which employs the ABCD matrix formalism. The expected focus size was found to be 40 µm. The signal mode with the mirror positions marked is shown in Fig. 3.12.

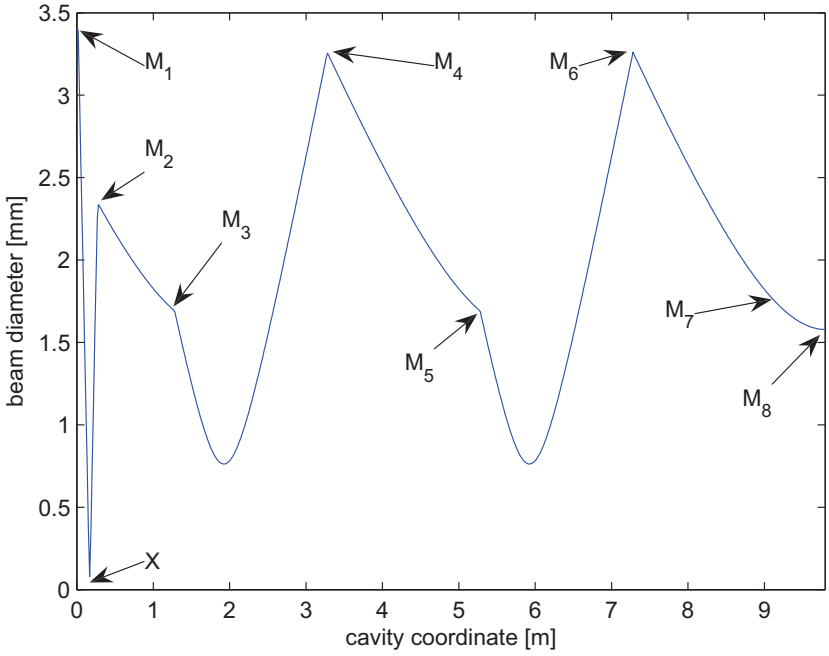

Figure 3.12: The shape of the OPO signal mode as calculated by the LCAV program with ABCD matrices. The positions of the mirrors and the crystal are marked, and the mirror numbers correspond to those in Fig. 3.11.

3.5 System characterisation

3.5.1 Slope efficiency

The pump power was freely changed from 0–7 W by means of a half–waveplate and a cube polariser. The maximum pump power used was limited to 2 W as the built–in amplifier isolator had limited isolation efficiency and the modelocking ceased after increasing power to 3W. It is expected that the application of an external isolator will remove this issue, but this has not yet been implemented.

The slope efficiency was measured for two different output couplers, namely 10% and 25% for the OPO operating at the 30 µm grating and the data are shown in Fig. 3.13.

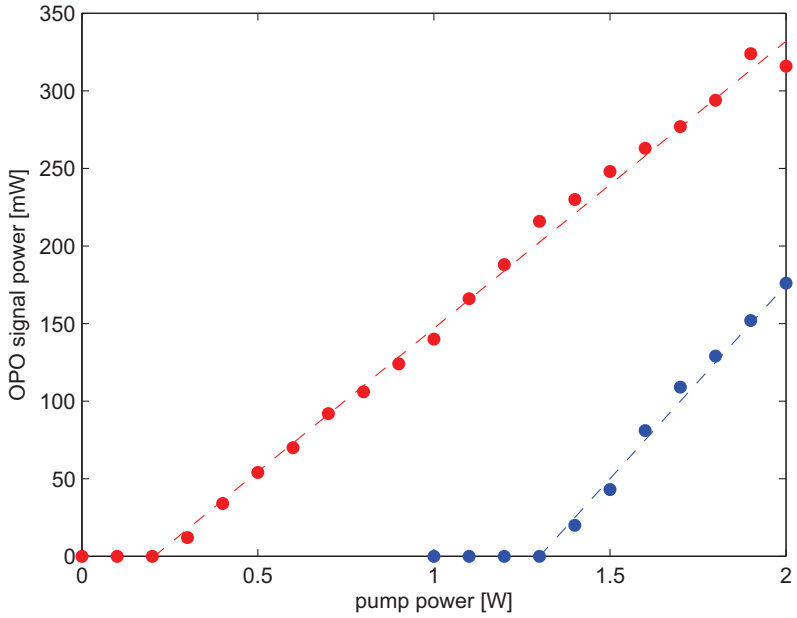

Figure 3.13: The extracted OPO power for two different output couplers. The red symbols denote 10% and the blue symbols — 25% output coupling value. The dashed lines are the linear fits. The slope efficiencies were 18.5% (10% output coupler) and 25% (25% output coupler).

To obtain the highest intracavity energy a 10% value for the output coupler transmission was studied for future operation. The threshold in these conditions was estimated as 200 mW and the slope efficiency was 18.5%. For 25% output coupling the threshold was much higher, 1.3 W, and the slope efficiency was 25%.

3.5.2 Optimal output coupling

The measurements of the output power as a function of the output coupling were performed with a microscope slide inserted into the cavity which was precisely rotated to vary the Fresnel reflection losses. The angular range between Brewster's angle and 90° was used to obtain the highest dynamic range from 0% to almost 100%. The schematic of the measurement process is shown in Fig. 3.14.

The measured powers P_1–P_5, corresponding to losses δ_1–δ_5, were measured as a function of the glass plate rotation angle. The loss δ_3 is the output coupling

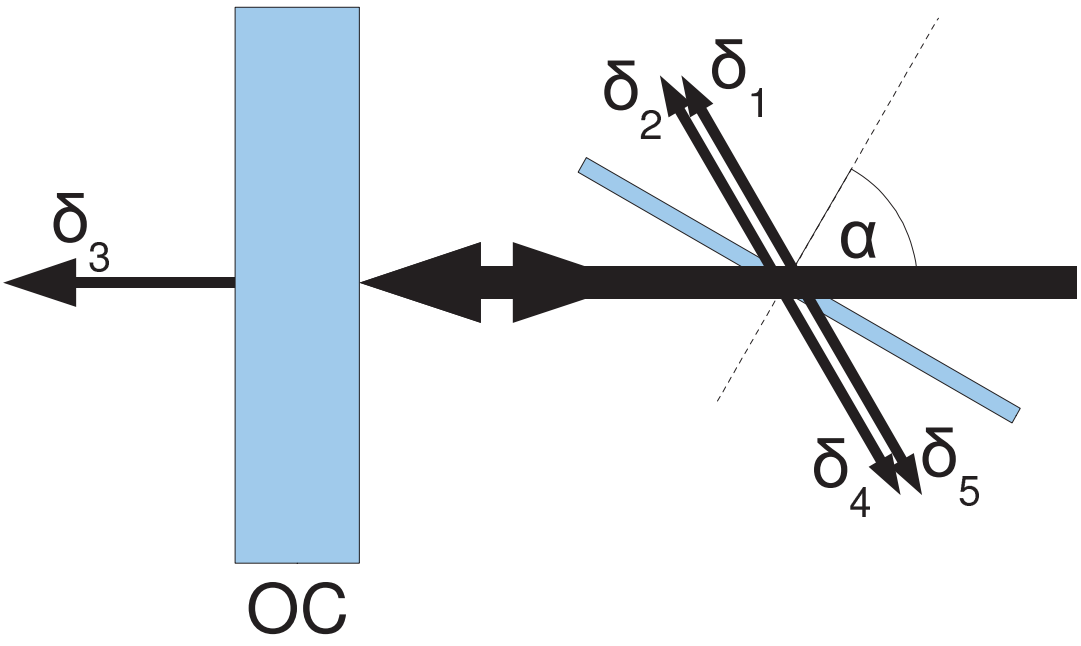

Figure 3.14: The measurement scheme of the total usable output power as a function of output coupling. The glass plate was rotated in steps of around 0.6°, and for each position the cavity alignment was optimised and all the powers corresponding to losses δ_1–δ_5 were measured.

value. In the measurements this was either 0% or 10%, and then the two sets of data were concatenated. The theory of Fresnel reflection was used to map the angle to the reflection losses δ_1–δ_2 and δ_3–δ_4:

$$\delta_{\mathrm{i}}(\alpha) = \left\{ \frac{\tan\left[\alpha - \arcsin\left(\frac{\sin(\alpha)}{n}\right)\right]}{\tan\left[\alpha + \arcsin\left(\frac{\sin(\alpha)}{n}\right)\right]} \right\}^2, \tag{3.12}$$

and then the total percentage losses giving the useful output were found for the roundtrip, taking into account the decreasing power as a result of the outcoupling:

$$\delta_{\mathrm{TOT}} = 1 - \prod_{i=1}^{i=5}(1 - \delta_{\mathrm{i}}). \tag{3.13}$$

The loss δ_{TOT} was accepted as the value of the effective output coupling and the total measured extracted power $P_{\mathrm{TOT}} = \sum_1^5 P_{\mathrm{i}}$ was plotted against δ_{TOT} in Fig. 3.15.

A theoretical fitting procedure was performed as follows. There is a known relation between the cavity constants and the output power (e.g. [3.26]) in the approximation of a small output coupling loss:

$$P_{\mathrm{OUT}} = \delta_{\mathrm{TOT}} \left(\frac{\gamma}{\delta_{\mathrm{P}} + \delta_{\mathrm{TOT}}} - 1 \right) \frac{P_{\mathrm{SAT}}}{2}, \tag{3.14}$$

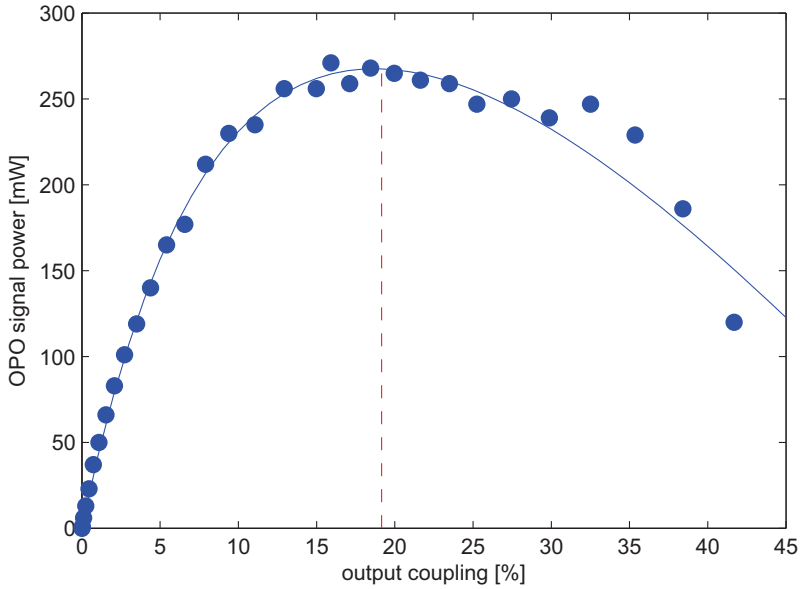

Figure 3.15: The output power as a function of output coupling. The line shows the theoretical fit using the approximation of the small output coupling, hence the less pronounced agreement in the large output coupling regime. The red line shows the position of the maximum of the curve which is the optimal output coupling value, 19%.

where γ is the gain exponential coefficient, δ_P are any uncontrolled parasitic losses inside the cavity, and P_{SAT} is the saturation power. The fit revealed the values shown in Tab. 3.2.

Table 3.2: The fit parameters for the output coupling equation (3.14) and the curve in Fig. 3.15.

γ	0.75
δ_P	17%
P_{SAT}	2.6 W

The γ coefficient translates to a linear gain value of $\exp(\gamma) = 2.1$.

It must be mentioned that the theory behind the equation (3.14) is valid only for small output coupling values (when the intra–cavity power after applying the losses does not change much) so the imperfect fit in the region of large output coupling is not a problem. Usually this approximation gives values higher than actually measured for high output coupling and generally any conclusions

should be drawn based on the small output coupling region. The behaviour of the experimental data is as expected as the output power should drop to zero for some maximal output coupling which was not actually observed due to the very quick dependence of $\delta_i(\alpha)$ in the $\alpha \lessapprox 90°$ regime, however the tendency seems to show it clearly.

3.5.3 Signal tunability

At the 2 W pump power only four gratings gave oscillations, these with the periods ranging from 28–31 µm. The output power available was 140 mW, 260 mW, 320 mW and 26 mW for the periods 28 µm, 29 µm, 30 µm and 31 µm, respectively. The average power of 320 mW translates to a pulse energy of approximately 21 nJ:

$$E = \frac{P_{\mathrm{AVG}}}{f_{\mathrm{REP}}}. \tag{3.15}$$

The OPO signal spectra were measured for each grating and are presented in the Fig. 3.16. There are some interesting features to comment in this data. The operation using grating (a) is affected by water absorption in the cavity at these wavelengths, hence the heavily structured spectra. Grating (b) gives a very broad spectrum for one of the cavity lengths. Grating (c) probably introduces double–pulsing to the OPO action which can be inferred from the regularly fringed spectra with a deep modulation. Grating (d) is free from these modulations and allows for precise tuning beyond 1530 nm.

A check of the agreement with the theoretically predicted tunability (Fig. 3.9) was made, and for each grating the tuning range was defined by the following values:

$$\lambda_{\mathrm{MIN}} = \lambda_{\mathrm{MIN}}^{\mathrm{CENTRAL}} - 2 \cdot \sigma\left(\lambda_{\mathrm{MIN}}^{\mathrm{CENTRAL}}\right) \tag{3.16}$$

$$\lambda_{\mathrm{MAX}} = \lambda_{\mathrm{MAX}}^{\mathrm{CENTRAL}} + 2 \cdot \sigma\left(\lambda_{\mathrm{MAX}}^{\mathrm{CENTRAL}}\right), \tag{3.17}$$

where $\lambda_i^{\mathrm{CENTRAL}}$ are the central wavelengths for the shortest and the longest wavelength spectrum observed at the given grating, for each spectrum calculated as the first moment of the intensity distribution and shown in Fig. 3.16:

$$\lambda_{\mathrm{CENTRAL}} = \frac{\sum\limits_{\lambda} [\lambda \cdot I(\lambda)]}{\sum\limits_{\lambda} I(\lambda)}, \tag{3.18}$$

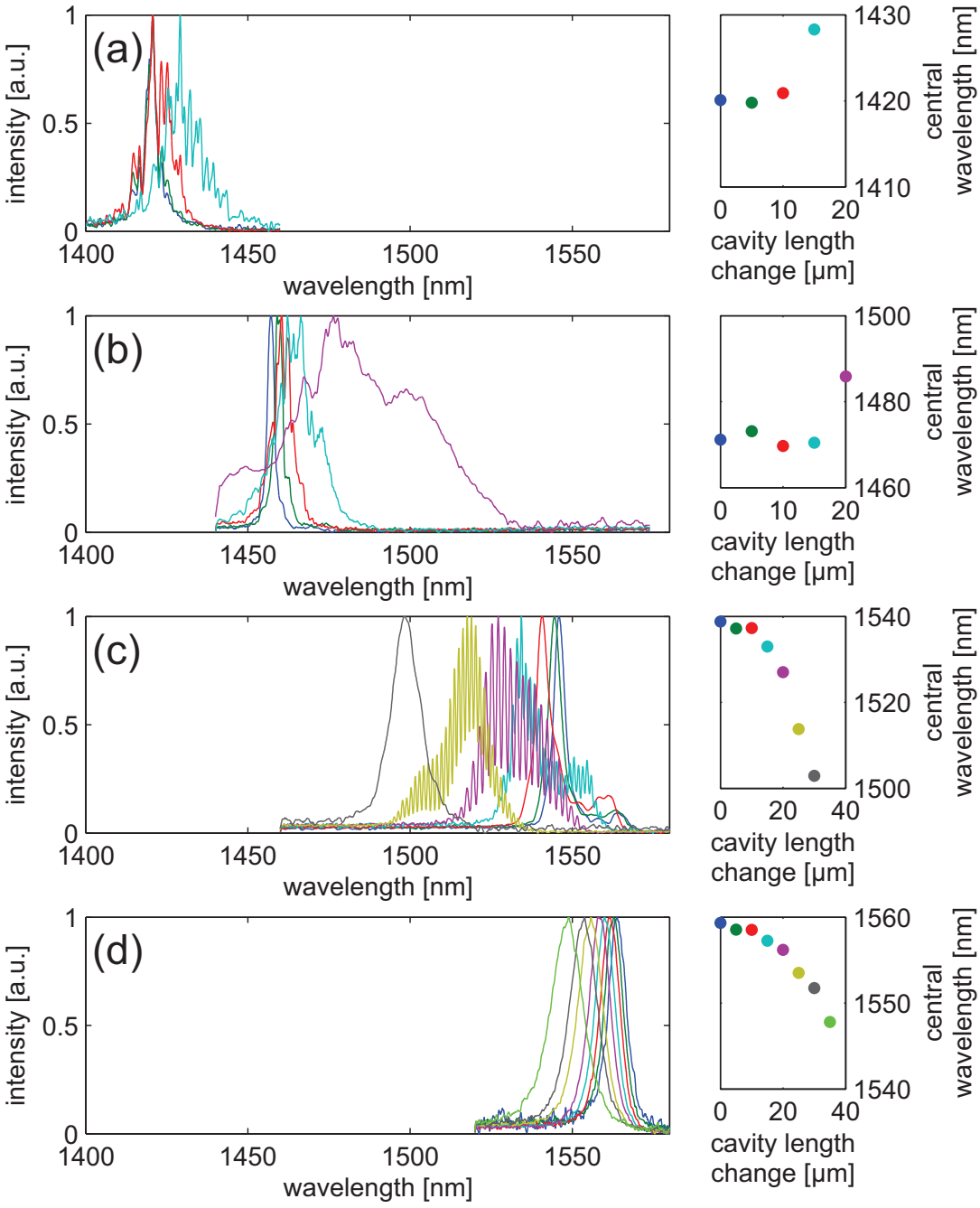

Figure 3.16: The OPO signal spectra for four gratings. (a): 28 μm, (b): 29 μm, (c): 30 μm, (d): 31 μm. Cavity length–tuned spectra obtained with any single grating are overlaid on each of the corresponding graphs (a)–(d). The cavity length adjustment step was 5 μm. The small graphs on the right–hand side show the direction of tuning for each grating.

and σ is the standard deviation of these spectra defined as the second moment of the intensity distribution:

$$\sigma\left(\lambda_{\mathrm{i}}^{\mathrm{CENTRAL}}\right) = \sqrt{\frac{\sum\limits_{\lambda}\left[\left(\lambda - \lambda_{\mathrm{i}}^{\mathrm{CENTRAL}}\right)^{2} \cdot I(\lambda)\right]}{\sum\limits_{\lambda} I(\lambda)}}. \tag{3.19}$$

The full tunability intervals for each grating were calculated and are shown in Fig. 3.17.

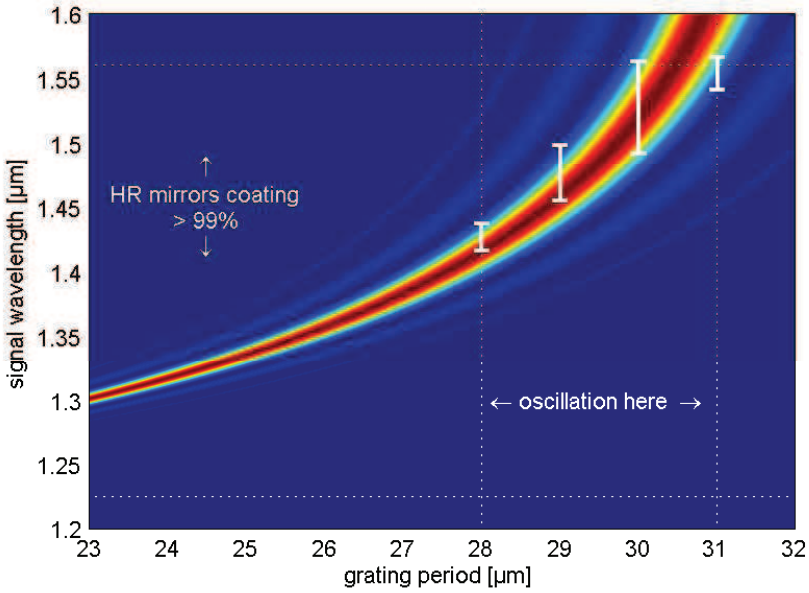

Figure 3.17: The measured tunability of the OPO. The dotted lines denote the grating periods for which oscillation occurred. The horizontal axis range spans all the grating periods incorporated in the crystal.

The general agreement with theory is good. The cutoff at the long wavelengths (> 1.55 μm) can be explained by the edge of the high reflectivity region at the cavity mirrors coating.

3.5.4 Cavity group delay dispersion

As the tunability data was available, it was possible to assess the cavity group delay dispersion. Not all the spectra had a well–defined central wavelength, so the "centre of mass" of each spectrum was found as the first moment of the intensity distribution (Eq. 3.18) and this quantity was plotted against the cavity length change. Sets of points originating from different gratings were freely shifted by

an arbitrary length as this is not a measurable value and it is a fitting parameter in the concatenation process for these data sets. Then the cavity length change coordinate ΔL was mapped to the delay coordinate τ by the relation:

$$\tau = \frac{2\Delta L}{c}. \tag{3.20}$$

The fit to the $\tau(\omega)$ was performed with a third–degree polynomial and the subsequently taken derivative, $d\tau/d\omega$, is the group delay dispersion. The data, the fit and the derived GDD are shown in Fig. 3.18.

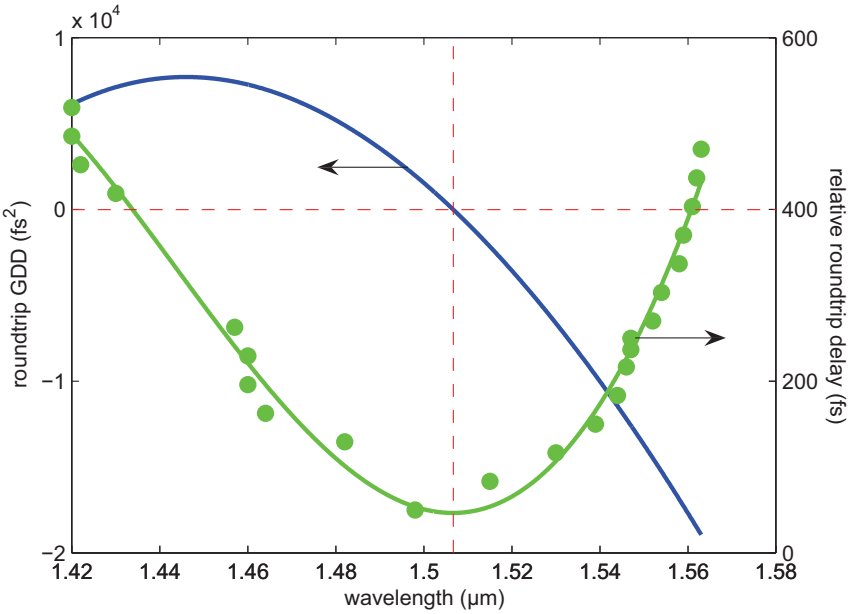

Figure 3.18: The cavity group delay dispersion. The measured delays for different wavelengths are shown with the green points. The green curve is the third–order polynomial fit to this data and the blue curve is its derivative (the GDD). The red horizontal line shows the zero value of the GDD, and the vertical one — the wavelength at which the GDD equals zero, namely 1.506 μm.

The result of this analysis is the knowledge of the zero–dispersion wavelength for this cavity. It is 1.506 μm and the OPO works in both regimes: negative– and positive–dispersion. For stability reasons an advantageous mode of operation would be in the region of negative dispersion but this requires compensation of more than 7700 fs^2 of positive GDD by a prism pair or a block of a negatively dispersive material.

3.5.5 Signal pulse measurement

The OPO signal autocorrelation functions were measured for the gratings with 28, 29 and 30 µm gratings. The 31 µm grating signal was too weak to be measured this way. The pairs of spectra and the corresponding autocorrelation functions are presented in Fig. 3.19. The pulse durations estimated basing on the FWHM of the intensity autocorrelation and assuming the sech^2 pulse shape corresponding to the presented measurements are: (a): 170 fs, (b): 287 fs, (c): 295 fs and (d): 475 fs.

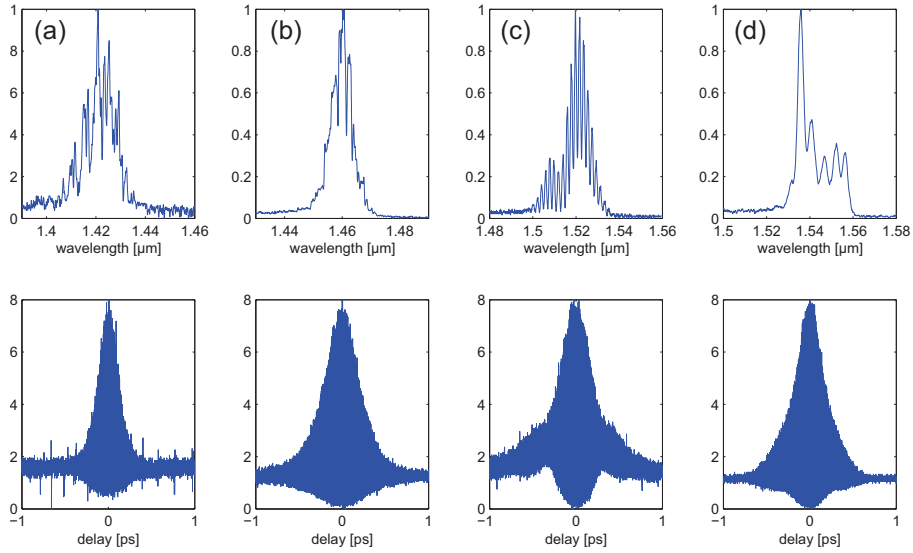

Figure 3.19: The measured spectra and autocorrelation functions for different signal tuning positions. (a): 28 µm grating, (b): 29 µm grating, (c) and (d): 30 µm grating.

3.5.6 Phase noise measurement

The measurement of the phase noise was performed using a built–in function of an Agilent N9068A Spectrum Analyzer, for both pump laser and OPO. A silicon photodiode was used as a linear detector for the pump wavelengths and an InGaAs photodiode for the OPO.

The results are shown in Fig. 3.20 and show that the phase noise is actually smaller for the OPO output than for the pump, which is not unexpected, even if the natural guess would be that the errors should accumulate and be larger

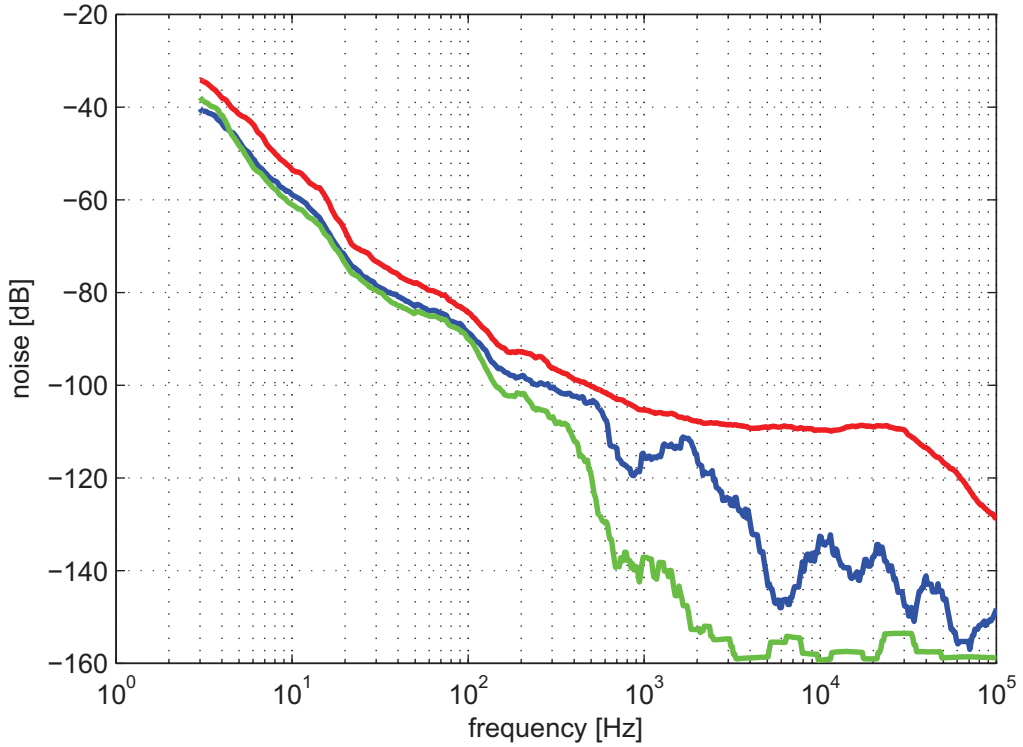

Figure 3.20: The phase noise of the OPO. The red line shows the pump noise and the blue and green lines denote OPO signal noise for the biggest (29 µm grating) and the smallest (31 µm), respectively. The noise for the signal at the 28 µm grating was not measured due to high instability. The noise for the OPO signal was always smaller than the original noise of the pump.

after the stage of the optical generation process. It seems that the OPO, being a synchronously pumped device, acts as a frequency filter for the repetition rate of the pump pulses — if the pump timing jitter is too big, the out–of–phase pulses are just not used in the generation process due to the lack of the temporal overlap with the oscillating signal. No output signal pulses exist for these misplaced pump pulses so the phase noise is not propagated through to the OPO stage. The actual effect may be some increased amplitude noise due to the unused pump pulses which missed their precisely determined moment for the interaction and did not transfer any energy to the signal beam.

3.6 Signal dynamics simulations

A numerical model was created to find the OPO signal dynamics. It was based on applying the coupled wave equations to the propagation in the PPLN crystal. The code consisted of the following steps:

1. creating the pump, signal and idler pulses in time– and spectral–domain
2. design of a PPLN crystal of a given length and grating period
3. calculation of a phase acquired after signal propagation through a small dz length of the crystal
4. calculation of the difference of delays between the pump and the signal after the propagation through the entire crystal
5. calculation of the cavity dispersion based on the fit coefficients found with the procedure described in the section 3.5.4
6. calculation of the self–phase modulation effect in the crystal
7. the oscillation loop in dz steps inside the crystal:
    - solving the coupled wave equations for the crystal propagation in dz steps
    - applying the PPLN–caused phase to the signal
    - applying the cavity–caused phase to the signal
    - applying the cavity losses
    - applying the delay so the pump and signal pulses overlap in the crystal in the next step of the loop
    - applying the self–phase modulation–caused phase to the signal

Only a preliminary check was performed — the code was run and after each 100 oscillation steps the delay between the pump and the signal was changed by a value corresponding to 5 µm of the cavity length which was the increment also used for the measurement of the tunability. The position of the maximum of the spectrum was recorded and plotted with the measured values in Fig. 3.21.

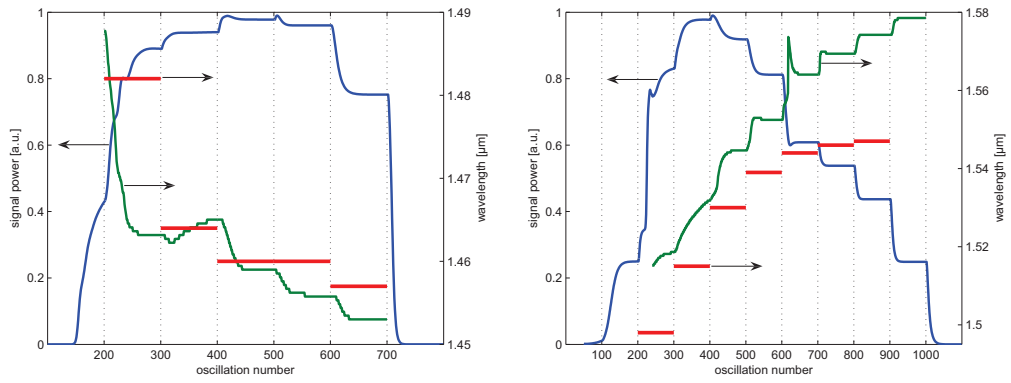

(a) (b)

Figure 3.21: The results of the OPO simulation for 29 μm (a) and 30 μm (b) gratings compared with the measured central wavelengths. The rapid change of the cavity length occurs every 100 oscillations (in the places of vertical dashed lines) and is equal to the value used in the experiment, 5 μm. The blue line shows the evolution of the OPO normalised optical power, the green one denotes the current central wavelength during the evolution and the red bars are the measured values of the central wavelength. A worse agreement in (b) may be explained by the edge of high reflectivity of cavity mirrors which was not modelled exactly in the code.

The absolute values of the experimental delay and the one used in the calculations are not identical so there is a freedom of a horizontal movement for the red bars on the Fig. 3.21 and this may introduce some disagreement, however a general tuning behaviour inferred from the model is correct. The sign of dispersion agrees (the direction of tuning) and the position of the modelled central wavelengths is not far from the measured positions, too. A better agreement is obtained for the shorter wavelengths (29 μm grating) but it may be explained by the fact that the high reflectivity region for the cavity mirror coatings does not extend beyond 1.6 μm. It was included in the model however only as a sharp edge at 1.6 μm, but actually the finite reflectivity occurs for even shorter wavelengths and it may be responsible for the fact that the OPO tuning is "repelled" from this region while in the model there is no phenomenon of this kind.

When it comes to spectral shapes, they were also qualitatively good (in terms of their FWHM), however finding in the model exactly the same spectra as in the experiment would require the more accurate inclusion of self–phase modulation

and the addition of water absorption. Temporal profiles for the shorter gratings were typically a factor of 2–3 longer than the durations estimated experimentally from the autocorrelation measurements — the duration was always at least 500 fs long.

3.7 Conclusions and outlook

A high–pulse–energy optical parametric oscillator working between 1410–1580 nm was built and characterised. The pump laser was also characterised and the pulse–compression scheme was applied to optimise the pump beam peak power and the nonlinear interaction in the OPO crystal.

The maximum average signal power at 10% output coupling was measured to be 230 mW, corresponding to 21 nJ of pulse energy. Pulse durations based on the autocorrelation measurements were in the range 170–475 fs. The cavity group delay dispersion was measured and positive– and negative GDD spectral regions were identified. Also the optimal output coupling was found to be 19%.

The planned application for this device will be silicon waveguide writing. Even more pulse energy and stability will be required for precise machining so the next steps improving the overall performance are in preparation now. These will include:

- building an acrylic glass box around the cavity mounts to eliminate the air currents and variations of its refractive index caused by temperature instability,
- active cavity length stabilisation with a piezo actuator and a spectrum–based automated feedback process,
- applying higher pump power after securing the pump laser from back–reflections which could damage the laser or make it unstable — this will probably activate the oscillations with the remaining gratings, increasing the expected tuning range down to 1.3 µm.
- cavity dumping which will give access to full intracavity power.

3.8 References

[3.1] M. Deubel, M. Wegener, S. Linden, G. von Freymann and S. John, "3D-2D-3D photonic crystal heterostructures fabricated by direct laser writing", *Optics Letters* **31** (6), p. 805–807, 2006.

[3.2] K. O. Hill, Y. Fujii, D. C. Johnson and B. S. Kawasaki, "Photosensitivity in optical fiber waveguides: Application to reflection filter fabrication", *Applied Physics Letters* **32** (10), p. 647–649, 1978.

[3.3] J. F. Ready, "Effects due to absorption of laser radiation", *Journal of Applied Physics* **36** (2), p. 462–468, 1965.

[3.4] S. Küper and M. Stuke, "Ablation of polytetrafluoroethylene (Teflon) with femtosecond UV excimer laser pulses", *Applied Physics Letters* **54** (1), p. 4–6, 1989.

[3.5] S. Watanabe, R. R. Anderson, S. Brorson, G. Dalickas, J. G. Fujimoto and T. J. Flotte, "Comparative studies of femtosecond to microsecond laser pulses on selective pigmented cell injury in skin", *Photochemistry and Photobiology* **53** (6), p. 757–762, 1991.

[3.6] D. Stern, R. W. Schoenlein, C. A. Puliafito, E. T. Dobi, B. R. and J. G. Fujimoto, "Corneal ablation by nanosecond, picosecond, and femtosecond lasers at 532 and 625 nm", *Archives of Ophtalmology* **107** (4), p. 587–592, 1989.

[3.7] C. V. Shank, R. Yen and C. Hirlimann, "Time-resolved reflectivity measurements of femtosecond–optical–pulse–induced phase transitions in silicon", *Physical Review Letters* **50** (6), p. 454–457, 1983.

[3.8] D. Du, X. Liu, G. Korn, J. Squier and G. Mourou, "Laser–induced breakdown by impact ionization in SiO_2 with pulse widths from 7 ns to 150 fs", *Applied Physics Letters* **64** (23), p. 3071–3073, 1994.

[3.9] B. C. Stuart, M. D. Feit, A. M. Rubenchik, B. W. Shore and M. D. Perry, "Laser–induced damage in dielectrics with nanosecond to subpicosecond pulses", *Physical Review Letters* **74** (12), p. 2248–2251, 1995.

[3.10] P. P. Pronko, S. K. Dutta, D. Du and R. K. Singh, "Thermophysical effects in laser processing of materials with picosecond and femtosecond pulses", *Journal of Applied Physics* **78** (10), p. 6233–6235, 1995.

[3.11] P. P. Pronko, S. K. Dutta, J. Squier, J. V. Rudd, D. Du and G. Mourou, "Machining of sub–micron holes using a femtosecond laser at 800 nm", *Optics Communications* **114** (1–2), p. 106–110, 1995.

[3.12] K. M. Davis, K. Miura, N. Sugimoto and K. Hirao, "Writing waveguides in glass with a femtosecond laser", *Optics Letters* **21** (21), p. 1729–1731, 1996.

[3.13] R. R. Thomson, H. T. Bookey, N. Psaila, S. Campbell, D. T. Reid, S. Shen, A. Jha and A. K. Kar, "Internal gain from an erbium–doped oxyfluoride–silicate glass waveguide fabricated using femtosecond waveguide inscription", *IEEE Photonic Technology Letters* **18** (14), p. 1515–1517, 2006.

[3.14] A. G. Okhrimchuk, A. V. Shestakov, I. Khrushchev and J. Mitchell, "Depressed cladding, buried waveguide laser formed in a YAG:Nd^{3+} crystal by femtosecond laser writing", *Optics Letters* **30** (17), p. 2248–2250, 2005.

[3.15] V. Apostolopoulos, L. Laversenne, T. Colomb, C. Depeursinge, R. P. Salathé, M. Pollnau, R. Osellame, G. Cerullo and P. Laporta, "Femtosecond–irradiation–induced refractive–index changes and channel waveguiding in bulk Ti^{3+}:Sapphire", *Applied Physics Letters* **85** (7), p. 1122–1124, 2004.

[3.16] R. R. Thomson, S. Campbell, I. J. Blewett, A. K. Kar and D. T. Reid, "Optical waveguide fabrication in z–cut lithium niobate ($LiNbO_3$) using femtosecond pulses in the low repetition rate regime", *Applied Physics Letters* **88** (11), p. 111109–111111, 2006.

[3.17] S. Campbell, R. R. Thomson, D. P. Hand, A. K. Kar, D. T. Reid, C. Canalias, V. Pasiskevicius and F. Laurell, "Frequency–doubling in femtosecond laser inscribed periodically–poled potassium titanyl phosphate waveguides", *Optics Express* **15** (25), p. 17146–17150, 2007.

[3.18] S. Zhang, J. Yao, W. Liu, Z. Huang, J. Wang, Y. Li, C. Tu and F. Lu, "Second harmonic generation of periodically poled potassium titanyl phosphate waveguide using femtosecond laser pulses", *Optics Express* **16** (18), p. 14180–14185, 2008.

[3.19] J. Burghoff, C. Grebing, S. Nolte and A. Tünnermann, "Efficient frequency doubling in femtosecond laser–written waveguides in lithium niobate", *Applied Physics Letters* **89** (8), p. 081108–081110, 2006.

[3.20] M. E. Fermann, A. Galvanauskas and G. Sucha, ed., *Ultrafast lasers: technology and applications*, Marcel Dekker, New York, 2003.

[3.21] `http://www.fianium.com`

[3.22] `http://www.ibsen.dk`

[3.23] H. Kogelnik and T. Li, "Laser beams and resonators", *Applied Optics* **5** (10), p. 1550–1567, 1966.

[3.24] P. A. Bélanger, "Beam propagation and the ABCD ray matrices", *Optics Letters* **16** (4), p. 196–198, 1991.

[3.25] `http://www.hcphotonics.com`

[3.26] A. E. Siegman, *Lasers*, University Science Books, 1986.

Chapter 4

Femtosecond pulse shaping with engineered quasi–phase matching of second harmonic generation in aperiodically poled lithium niobate

4.1 Motivation and background — pulse shaping

Femtosecond pulse shaping, originally pioneered in a very simple form by Heritage and co–workers [4.1], has attracted huge interest over the last few years as it is a very powerful technique allowing the creation of pulses having specific intensity envelope shapes or travelling in specially designed sequences, with limitations set only by the available spectrum. This feature is extremely important in many fields of optical physics, like the coherent control of chemical reactions [4.2, 4.3] or atomic wavefunction configurations [4.4], high–harmonic generation [4.5], sequential excitation of atoms or molecules [4.6, 4.7], femtosecond machining [4.8], optical communication encoding systems [4.9], efficient use of multiphoton processes in microscopy [4.10] and terahertz waveform generation [4.11]. The approach is suitable for general use in any experiment which needs adjustable chirp of given fixed laser pulses, usually for compensation of unwanted dispersion, for example in optical communication transmission systems [4.12] or after amplification. The chirped pulse amplification process itself

has also been enhanced by pulse shaping [4.13]. Recently a new shaper–assisted pulse measurement scheme was presented [4.14].

Two main modes of operation can be outlined — programmable and static pulse shaping. Programmable systems possess the capability to create many different output shapes from a single input one, by adjusting internal settings, which can be further enhanced by introducing the self–learning ability to the system [4.15]. Static methods, on the contrary, are designed to give a fixed output from an assumed input and are not able to be modified beyond that pre–defined application. Both versions are used and still developed as each technique possesses distinctive attractive elements: programmable shaping systems are flexible and adjustable, but complicated in alignment; static ones are usually robust and simple, however not really universal.

4.2 Programmable methods of femtosecond pulse shaping

Programmable methods usually rely on the manipulation of the signal in the Fourier domain because direct time–domain modulation is impractical. A phase is added selectively to desired spectral components and additionally, in some embodiments, spectral components can also be suitably attenuated. Such shapes can be arranged in a transmittive or reflective geometry. First, the pulse must be spectrally resolved in a zero–dispersion 4f setup and then, in a Fourier plane, the phase modification is applied. A more detailed theoretical description is presented in next sections, preceded by a short review of existing experimental techniques of femtosecond pulse shaping.

4.2.1 Liquid crystal modulators

In a transmittive geometry, a linear matrix of pixelated liquid crystals (LC) may selectively retard light in each of its discrete sections, and in this way an extra phase is added in the spectral domain [4.16]. A variable retardation is introduced by rotating crystal's axis and modifying the extraordinary refractive index as it is shown in Fig. 4.1. The use of additional polarizers before and after the liquid crystal cells makes it possible to vary the spectral amplitude of input pulses

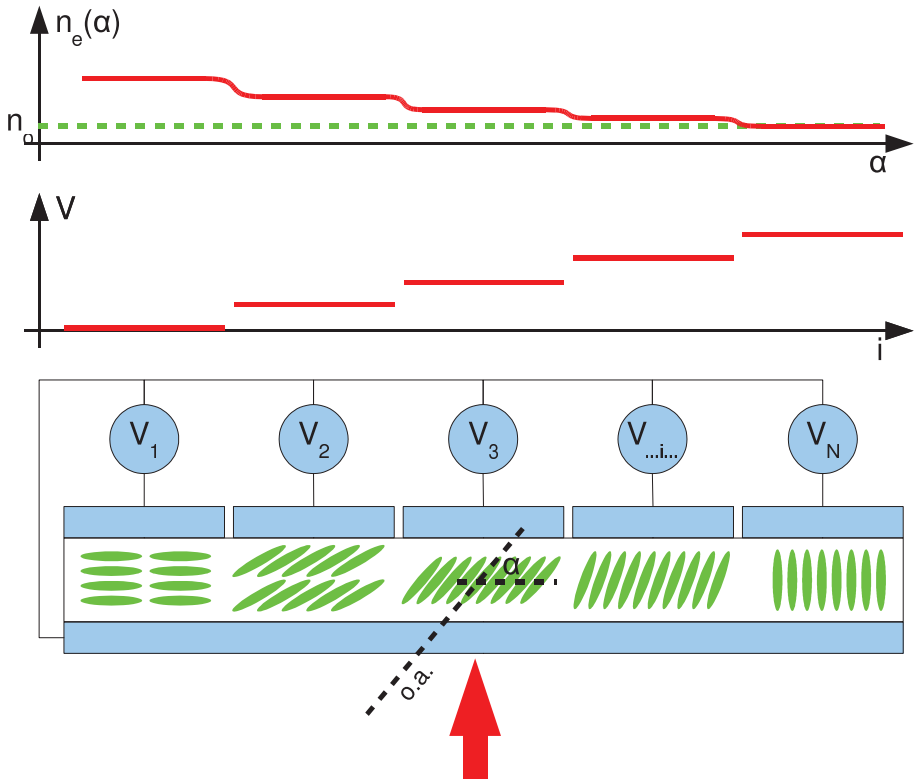

Figure 4.1: The principle of operation of the liquid crystal modulator. The voltages V_i can be independently modified to rotate the local optical axis (o.a.) of the liquid crystal in the plane of the drawing — the angle α describes the rotation. This modifies the extraordinary refractive index experienced by the light beam polarised in this plane. The electrodes are made of a transparent conductor so the device may be used in transmission or, after the suitable coating of the electrodes or attaching the mirror the reflective geometry may be used.

with a suitable attenuation. The phase–only, amplitude–only and phase–and–amplitude modulators are presented schematically in Fig. 4.2. These devices can be also used in a double–pass geometry after attaching a mirror to the back surface. The examples of successful pulse shaping experiments with the use of liquid crystal modulators are these of Weiner [4.16] and Brixner [4.17]. Commercial suppliers include CRi [4.18], Boulder Nonlinear Systems [4.19] and Forth Dimension Displays [4.20]. This electrically–addressed approach is actually an improved version of an originally static device, which employed a fixed, microlithographically etched phase mask instead of a programmable one [4.21]. Due to a huge market interest, these modulators are being continuously developed and now the Liquid Crystal on Silicon technology is widely introduced, e.g. by Hama-

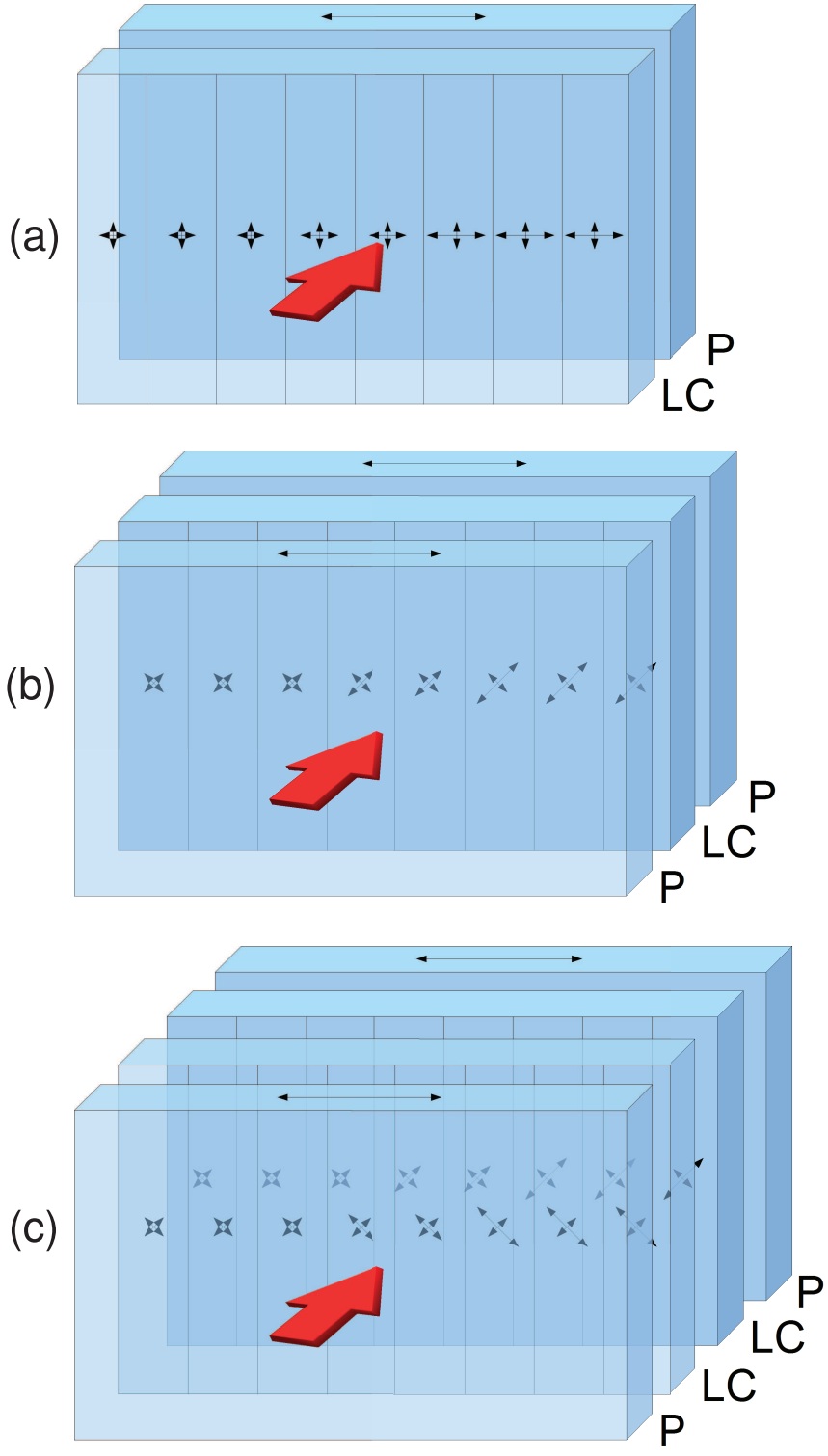

Figure 4.2: Three types of the LCM geometry: (a) is a phase modulator, (b) is the amplitude modulator, and (c) is a phase and amplitude modulator. The crossed black arrows in each of the modulator sections symbolise the refractive index value for the beam polarised along the respective direction. The ordinary index remains unchanged but the extraordinary one can be varied by the applied voltage. The red arrow schematically depicts the horizontally polarised input beam. P: polariser layers; LC: liquid crystal layers.

matsu [4.22]. There the crystal layer is deposited directly on a silicon substrate, making it suitable for combining the device with on–chip electronics.

Practically, the adjustment of the spectral phase is done by applying specific voltages to the transparent housing of the liquid crystal cells and, after suitable precalibration, the values of these voltages may be visualised on a computer screen to indicate the phase modulation in real time. Figure 4.3 shows a typical arrangement of the optical components in a transmittive shaper geometry using a liquid crystal spatial phase modulator.

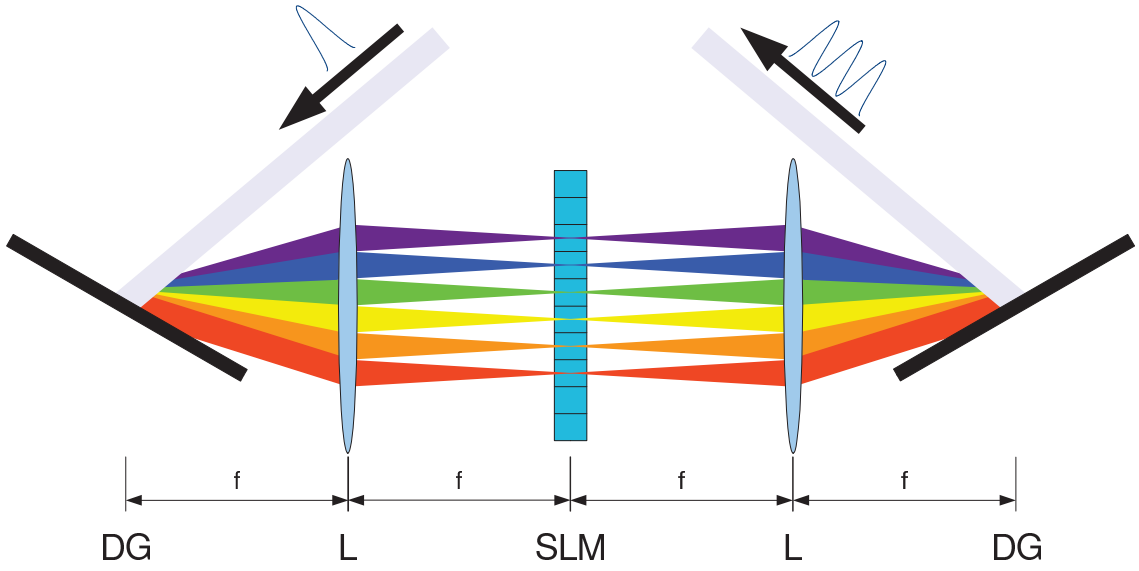

Figure 4.3: The zero–dispersion configuration of a transmittive setup realising pulse shaping with phase and/or amplitude modulation in a Fourier plane. DG: diffraction gratings, L: lenses, SLM: spatial light modulator.

In a more advanced version of this technique pixelation is removed by means of *optical addressing* [4.23], namely illuminating a transparent photoconductive layer with a spatially modulated light intensity to obtain smoothly variable resistance and the continuously variable voltage drop across the liquid crystal cell.

Liquid crystals are known to absorb a portion of incident light and thus are not always suitable for high energy applications. Also they cannot be used in certain specific spectral regions where non–negligible absorption occurs, however this solution remains the first choice femtosecond pulse shaping device and the available resolution is being continuously improved. The advantage is a small voltage required, in the order of 5 V.

4.2.2 Deformable mirrors

Instead of exploiting the retarding properties of liquid crystals one may use a purely reflective geometry method and arrange different paths in air for different spectral components by deforming a mirror's surface. The flexibility needed for this purpose is not very demanding — 2π in terms of phase delay in reflection equals half a wavelength, which usually in optical applications is less than 1 µm. More commonly, in the case of an undispersed beam, this so–called adaptive optics technology generally deals with modifying the geometry (or other properties) of the optical components in the setup to improve its transmission properties or removing the distortions introduced by the optical elements, acting directly on the wavefront shape. This idea originates from the astronomy community, where the main problem triggering this application is the fact that the atmospheric turbulence blurs the astronomical images and this effect can be efficiently removed by the means of the adaptive optics [4.24]. Medical applications are possible, too, e.g. in retinal imaging [4.25]. The adaptive optics approach with a deformable mirror proved to be useful in the optimisation of the process of femtosecond laser ablation [4.26].

Piezoelectric transducers are capable of changing their physical dimensions by several microns when a high voltage (typically of the order of 150 V) is applied. Existing devices of this kind involve attaching a thin optical substrate, polished and coated for high reflectivity, to a deformable material and addressing separately small sections corresponding to different fragments of spectrum. The designs fall into two groups: simple piezo–actuators adjustable perpendicularly to the attached mirror surface (Fig. 4.4) or a bimorph piezo–ceramic device which consists of two layers of the material capable of elongating in the parallel to the mirror surface (Fig. 4.5). Examples of successful constructions are described in [4.27] (perpendicular PZT) and [4.27,4.28] (bimorph). These constructions offer a continuous reflecting surface, so even though voltages are applied to separate pixels in the piezoceramic layer, the channels are not independent, however the surface is always smooth. The disadvantage is a high voltage required, typically 150–250 V.

Another approach is to use Coulomb forces and try to adjust the shape of a mirror by attracting the mirror's surface to the actuators. Such membrane mirrors

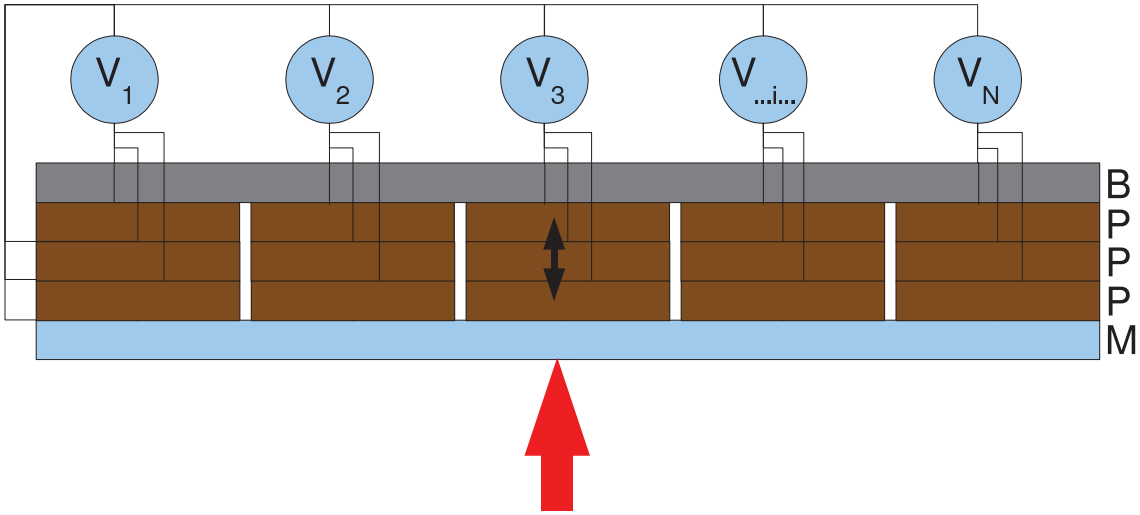

Figure 4.4: The schematic of the piezo–driven deformable mirror. Each actuator is formed of a stack of piezo–ceramic layers attached to the common mount with the voltage applied to each of them for a multiplied stretching effect. B: base mount, P: piezo ceramic, M: mirror. The black arrow shows the direction of the piezo deformation.

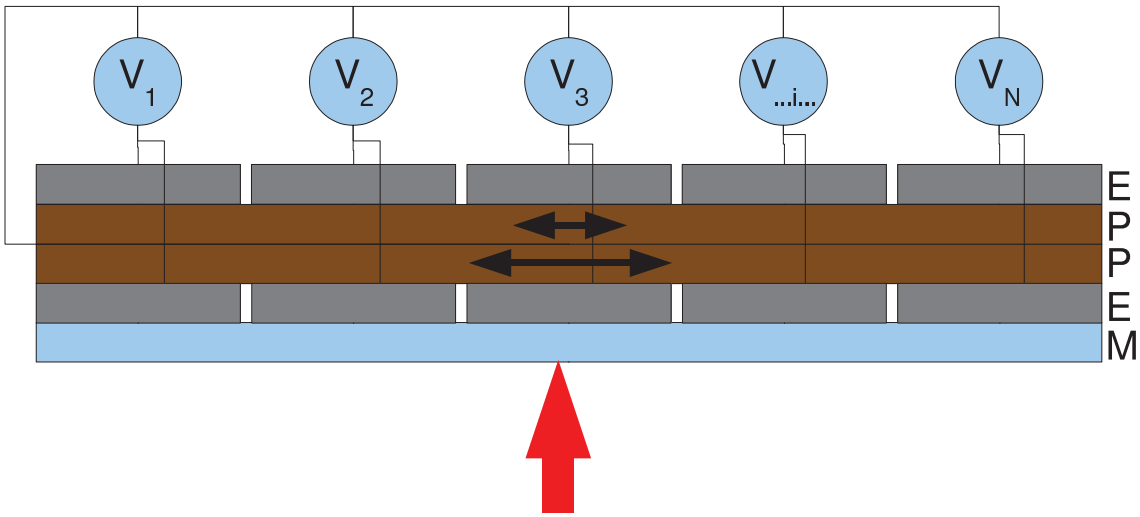

Figure 4.5: The schematic of the bimorph piezo–driven deformable mirror. Two layers of the piezo material polarised in parallel to the mirror surface can elongate and this way deform the mirror. E: electrodes, P: piezo ceramic, M: mirror. The black arrows show the direction of the piezo deformation.

are made of a thin silicon nitride (500–700 nm) or a thicker silicon layer (~100 µm) coated for high reflectivity and the series of electrodes not touching this membrane. The advantages are that the reflecting surface is continuous and the power consumption is negligible, however a voltage of the order of 200 V is essential.

The schematic is shown in Fig. 4.6. The examples of the use of commercially available devices are described in [4.29, 4.30]. The result of the further development and miniaturisation are Micro Electro–Mechanical Systems which offer separated individual piston–like micro–membranes mounted on–chip [4.31]. The diffraction losses reported are of the order of 5%.

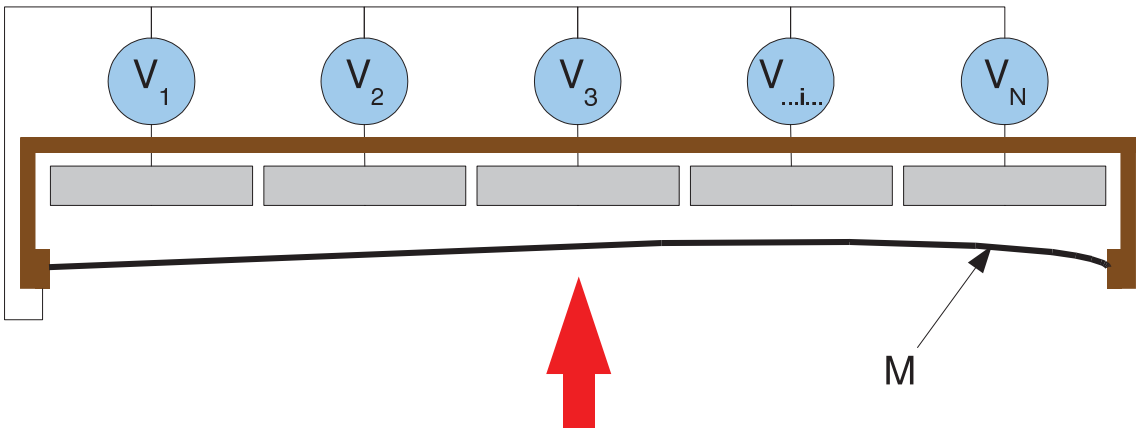

Figure 4.6: The electrostatic deformable mirror. The position of the membrane M is electrostatically actuated by variable voltages V_i. The red arrow shows the direction of the incoming beam.

Generally, the deformable mirrors form two main groups — having continuous and segmented mirror surfaces. Both have their advantages and disadvantages: the continuous surface does not introduce diffraction losses caused by the presence of gaps between the segments but there is always some degree of a crosstalk between the channels due to the physical connection. Another limitation for both types of mirrors is a lack of selective control over the light intensity — only the optical path is varied. The examples of manufacturers include OKO Technologies [4.32] and Boston Micromachines [4.33].

4.2.3 Other devices

A transmittive geometry may be also used with an acousto–optic modulator as a tool for diffracting selected spectral components in a Fourier plane [4.34]. A complicated radio frequency waveform is sent to the modulator (usually made of TeO_2) in a transverse direction so it can cause diffraction of precisely chosen spectrum fragments and the others, which are not diffracted, are rejected from the apparatus and do not take part in reconstruction of the pulse at the output

port of a 4f setup. The efficiency of diffraction depends on the RF signal power and can be varied.

Another possibility was realised in the "Dazzler" method [4.35, 4.36], now commercialised [4.37], where the acoustic waveform is launched into a $LiNbO_3$, $PbMoO_4$ or TeO_2 crystal collinearly with the light beam and forms a localised grating which can cause a phase–matched coupling of light to the other polarisation. The efficiency of the coupling depends on the acoustic power used. The big advantage is the fact that this device does not require to be placed in the Fourier plane of a zero–dispersion line but rather straight in the beam. The technique was successfully applied to amplified pulse compression [4.38], but is limited to low–repetition–rate pulses.

An excellent review article [4.39] describes all the details of pulse shaping with spatial light modulators and presents a comparison of practical aspects of using different methods.

It is worth mentioning that there exists another method which does not require decomposing the pulse into the spectral domain, but rather acts in a certain compact way to shape a pulse directly in the time domain. The use of birefringent crystals makes it possible to create simple patterns of series of identical pulses or nearly–square pulses. This technique was first proposed in [4.40] and recently developed [4.41]. So far it was not demonstrated to shape pulses in an arbitrary way but the optical setup remains extremely simple and linear, demanding only waveplates rotation ability. Due to this simplicity it can almost be regarded as a static method — after initial alignment it does not require any high voltage or radio frequency signal to work continuously, however it may be realigned to produce some other output shape. Anyway, as there was no general shaping shown with this technique, it remains in its early stage of development and is not widely used in experiments where something more than bursts of pulses or rectangular shapes is demanded.

4.3 Static methods of femtosecond pulse shaping

Static methods fall into two groups: they may act on the phase of existing pulses and adjust it according to device specifications (like distributed Bragg mirrors)

or may create another pulse which is shaped and the input pulse is discarded (nonlinear poled crystals).

4.3.1 Fibre Bragg gratings

The static modulation of the optical pulses is investigated intensively in the context of the dispersion–managed optical telecommunication in the picosecond regime (the review and the theoretical analysis is presented in [4.42]). Superstructured Bragg gratings have been used to generate shaped rectangular pulses of a good quality [4.43]. The term "superstructured" refers to those fibre Bragg gratings whose refractive index contrast is not uniform along the fibre length, both in terms of amplitude and phase.

There was also developed a method of extracting a series of pulses from a broadband input by using a specially prepared fibre containing several distributed Bragg mirrors [4.44]. The spatial distances between the reflectors buried in the fibre correspond to spatial and temporal distances between the output pulses. The pulses can also be centred around different wavelengths selected from the input spectrum as the maximum reflectivity of each of the mirrors can be designed independently. A later review article explains thoroughly various experimental aspects of this technique [4.45].

4.3.2 Poled nonlinear crystals

The other general method relies on the creation of shaped pulses generated by a nonlinear frequency–conversion process using the interaction of an input pulse and a structured nonlinear medium. In these processes a shaped pulse is produced at a different wavelength to the input pulse. The original work of Fejer and co–workers [4.46] described creation of second harmonic femtosecond pulse trains obtained by using specially designed poled nonlinear crystals of lithium niobate. The pulses were generated in precisely selected regions within the crystals due to the presence of the phase–matching grating patterns which were repeated along the crystal to make possible the generation of subsequent pulses. The gaps between pulses were possible due to the positioning of the different poled sections of the crystal.

This simple localised–conversion approach was later extended theoretically by Reid and co–workers [4.47, 4.48] to the idea of an engineerable generalised transfer function. This was the inspiration of my experiment which tested the performance of the crystal manufactured according to the design based on this calculations method.

4.4 Spectral and temporal transfer functions

4.4.1 The transfer function concept

In the low–conversion regime, the pulse shaping process can be described in the frequency domain as a multiplication by a certain complex "frequency response function" (transfer function) $H(\omega)$:

$$E_{\mathrm{OUT}}(\omega) = H(\omega) \cdot E_{\mathrm{IN}}(\omega). \tag{4.1}$$

As a complex number, the transfer function can be represented in an exponential form: $H(\omega) = |H(\omega)| \cdot e^{(i \cdot \arg[H(\omega)])}$, where $|H(\omega)|$ is responsible for attenuation and $\arg[H(\omega)]$ contains the information about introduced delays (phase). This frequency domain approach is equivalent to engineering the pulse shape in the time domain. The difference here is that the temporal "impulse response function" $h(t)$ does not stay in a simple linear relation to the pulse shape but can be expressed as:

$$e_{\mathrm{OUT}}(t) = \int_{-\infty}^{\infty} e_{\mathrm{IN}}(\tau) \cdot h(t-\tau) \cdot d\tau, \tag{4.2}$$

which is a convolution of the input pulse shape and temporal response function. The simple pulse shaping description in the frequency domain is very convenient, as trying to shape femtosecond pulses by acting on temporal phase is not practical due to the lack of high–speed modulators and therefore most methods use selective addressing of spectral phase and amplitude, thus employing $H(\omega)$. Usually the desired shape of the pulse is known in the time domain, so either $h(t)$ can be calculated and then its Fourier transform taken to find $H(\omega)$:

$$H(\omega) = \mathcal{F}[h(t)] = \int_{-\infty}^{\infty} h(t) \cdot e^{-i\omega t} \cdot dt \tag{4.3}$$

or some iterative algorithm varying $H(\omega)$ and using $e_{\mathrm{OUT}}(t)$ as a feedback should be applied to obtain the correct spectral transfer function.

4.4.2 Pulse propagation in a poled crystal

To calculate the effect of the pulse propagation in the medium, the coupled wave equations must be considered. For the case of second harmonic generation in the low conversion regime, these simplify to one propagation equation, namely:

$$\frac{dE_{\mathrm{SH}p}}{dz} = i\kappa d_{pqr} e^{i\Delta kz}, \tag{4.4}$$

where κ is a constant expression containing:

$$\kappa = -\frac{\omega_{\mathrm{SH}} E_{\mathrm{F}q} E_{\mathrm{F}r}}{c n_{\mathrm{SH}}}. \tag{4.5}$$

$E_{\mathrm{SH}p}$ is the generated second harmonic field polarised along the p direction, d_{pqr} is an absolute value of a nonlinear coefficient, Δkz is a phase mismatch, ω_{SH} is a frequency of the second harmonic field, c is a velocity of light, n_{SH} is a refractive index for second harmonic frequency, $E_{\mathrm{F}q}$ and $E_{\mathrm{F}r}$ are fundamental fields polarised along directions q and r, respectively.

The analytic solution of the equation 4.4 for a single crystal (one domain) of length q_1 is:

$$E_{\mathrm{SH}p}|_{q_1} = \frac{\kappa d_{pqr}}{\Delta k} e^{i\Delta k q_1} - \frac{\kappa d_{pqr}}{\Delta k}. \tag{4.6}$$

The field generated in any further m^{th} domain can be analytically calculated with the general formula, taking into the account the alternating polarity of domains:

$$E_{\mathrm{SH}p}|_z = a_m e^{ik\Delta z} + b_m, \tag{4.7}$$

where

$$a_m = -(-1)^m a_1 = -(-1)^m \frac{\kappa d_{pqr}}{\Delta k} \tag{4.8}$$

and

$$b_m = b_{m-1} + (a_{m-1} - a_m) \exp\left(i\Delta k \sum_{l=1}^{m-1} q_l \right). \tag{4.9}$$

When applied recursively, this formula gives the cumulative field generated during the propagation in the crystal consisting of u domains, whose domain boundary positions are defined by the vector Q_{u} according to Fig. 4.7:

$$Q_{\mathrm{u}} \coloneqq [q_1, q_1 + q_2, q_1 + q_2 + q_3, \ldots, q_1 + \cdots + q_{\mathrm{u}}], \tag{4.10}$$

and the total field value is equal to:

$$E_{\mathrm{SH}p}(\omega) = -\frac{\kappa d_{pqr}}{\Delta k(\omega)} \left[1 - (-1)^u e^{i\Delta k(\omega) Q_{\mathrm{u}}} + \sum_{v=1}^{u} 2(-1)^v e^{i\Delta k(\omega) Q_{\mathrm{v}}} \right]. \tag{4.11}$$

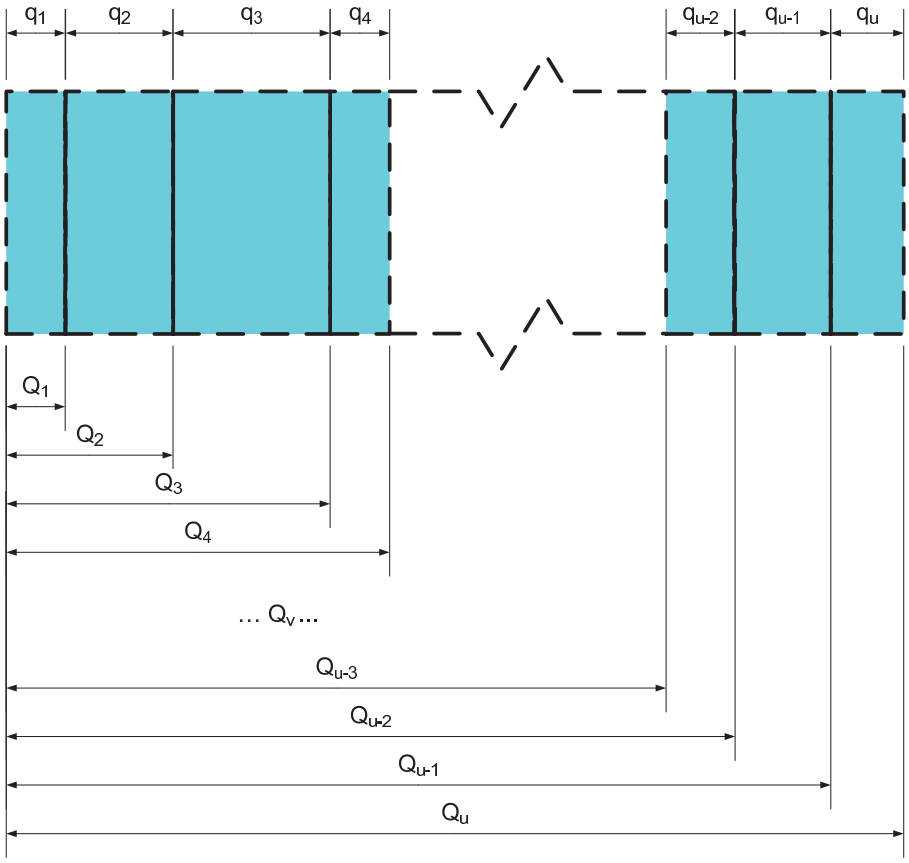

Figure 4.7: Definition of a Q_u vector. q_v are lengths of domains and Q_v are distances from the beginning of the crystal to the current boundary.

The κ contains the $E_{\mathrm{F}q}E_{\mathrm{F}r}$ component which, due to the assumption of a small conversion efficiency, is regarded as constant throughout the propagation and thus the initial fundamental field value for every domain is the same.

4.4.3 The crystal transfer function

The isolated total effect of the crystal on the propagation may be expressed in one equation describing the generalised transfer function:

$$E_{\mathrm{CRYS}}(\omega) = -\frac{\kappa' d_{pqr}}{\Delta k(\omega)}\left[1 - (-1)^u e^{i\Delta k(\omega)Q_\mathrm{u}} + \sum_{v=1}^{u} 2(-1)^v e^{i\Delta k(\omega)Q_\mathrm{v}}\right], \tag{4.12}$$

which, for the output intensity $|E(\omega)|^2$, in the case of a periodic crystal leads to the well–known $\mathrm{sinc}^2(\Delta k \cdot L/2)$ function. κ' is defined as:

$$\kappa' = \frac{\kappa}{E_{\mathrm{F}q}E_{\mathrm{F}r}} = -\frac{\omega_{\mathrm{SH}}}{cn_{\mathrm{SH}}}, \tag{4.13}$$

which makes it independent on the input fields. Now, when the calculation of the output second harmonic field $E_{\mathrm{SH}}(t)$ is carried out, it only requires a simple one–

step analytic formula with no need for introducing lengthy propagation loops:

$$E_{\mathrm{SH}}(t) = \mathcal{F}^{-1}\left\{\mathcal{F}\left[E_{\mathrm{IN}}^2(t)\right] \cdot E_{\mathrm{CRYS}}(\omega)\right\}, \tag{4.14}$$

where $\mathcal{F}$ is the Fourier transform operator and $\mathcal{F}^{-1}$ is the inverse Fourier transform operator.

This observation allows for a very flexible engineering of the output pulse temporal shape. A practical difficulty remains in the fact that there is no simple "reverse" calculation procedure which can work by applying a single formula to reveal the optimal grating design when the target pulse $E_{\mathrm{SH}}(t)$ is known.

4.5 Design of aperiodic gratings for pulse shaping

The well–established way of solving numerically a problem like the design of pulse–shaping domain pattern is using some iterative minimisation algorithm. In this particular situation the "simulated annealing" [4.49] method was employed.

The simulated annealing algorithm relies on the iterative calculations of the SH pulses, finding their effective "distance" from the ideal target pulses and using this difference as a feedback for next iterations which involve random perturbations, accepted or not depending on the gradually decreased "temperature" value, thus minimising the risk of finding false global minima. The number symbolising the distance between the current solution and the ideal one must be sensitive to even small differences, and due to this requirement the FROG–based RMS error definition was selected, which gives a good representation of the similarity between two pulses in amplitude and phase:

$$e_k = \sqrt{\sum_{\tau}\sum_{\omega}\left|I_{\mathrm{FROG}}^{\mathrm{SHG}}(\tau,\omega) - I_{\mathrm{FROG}}^{\mathrm{TARGET}}(\tau,\omega)\right|^2}. \tag{4.15}$$

The polarisation–gated FROG version was used as it discriminates between two time–reversed and otherwise identical solutions. The $I_{\mathrm{FROG}}(\tau,\omega)$ trace can be synthetically generated for any pulse and is defined as:

$$I_{\mathrm{FROG}}(\tau,\omega) = \left|\int_{-\infty}^{\infty} E_{\mathrm{F}}(t)|E_{\mathrm{F}}(t-\tau)|^2 e^{-i\omega t}dt\right|^2. \tag{4.16}$$

The exact algorithm structure is shown in the Fig. 4.8.

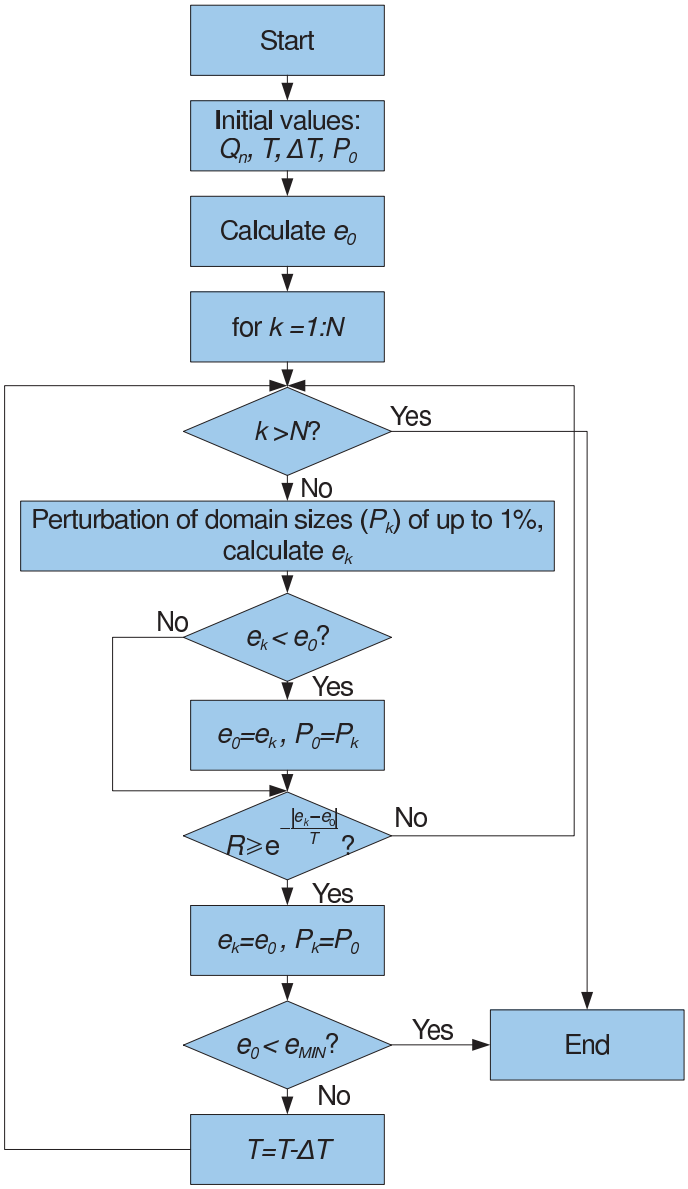

Figure 4.8: The algorithm flowchart for the crystal design procedure.

This approach requires the knowledge of the input pulse but it was not characterised at the time of performing the crystal design. This was the reason of assuming some ideal, but realistic pulse — a Fourier–limited Gaussian shape with the duration of 150 fs and spectrally centred around 1530 nm.

Nine grating patterns were designed with the help of this algorithm and the corresponding target SH pulse shapes are listed in the Table 4.1.

The final crystal design is shown in Fig. 4.9. It was fabricated by HC Photonics. The domain sizes for all the nine sections are shown in the Fig. 4.10. Some intuitive regularities can be found in these patterns. First of all, the constant slope in (f) and (g), which correspond to the positively and negatively chirped pulses,

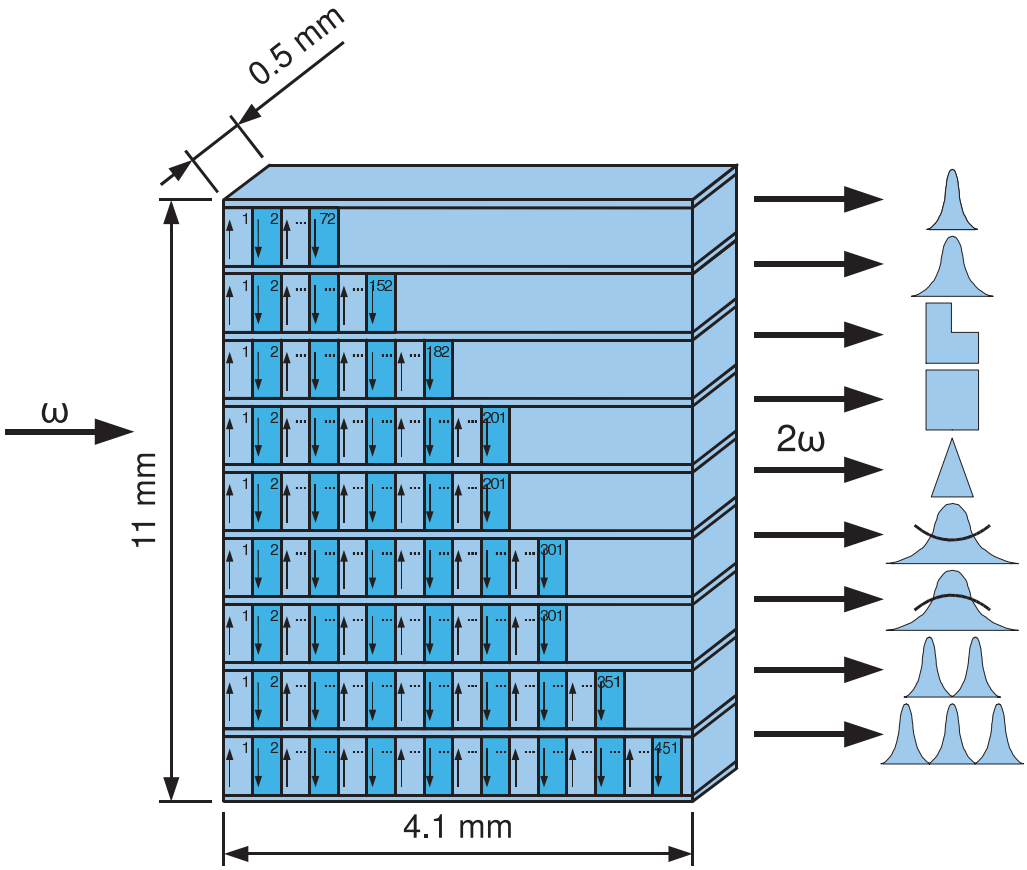

Figure 4.9: The details of the shaping crystal design. Nine gratings were created in one lithium niobate crystal. The exact numbers of domains are shown for each grating. The fundamental beam (ω) is coming from left to right and is polarised horizontally. The schematic expected shapes of second harmonic (2ω) pulses are shown in the right.

Table 4.1: Nine target pulses

(a)	Fourier–limited 150 fs Gaussian pulse
(b)	Fourier–limited 200 fs Gaussian pulse
(c)	stepped 400 fs pulse
(d)	rectangular 400 fs pulse
(e)	triangular 200 fs pulse
(f)	positively chirped 300 fs pulse
(g)	negatively chirped 300 fs pulse
(h)	two pulses, 150 fs each
(i)	three pulses, 150 fs each

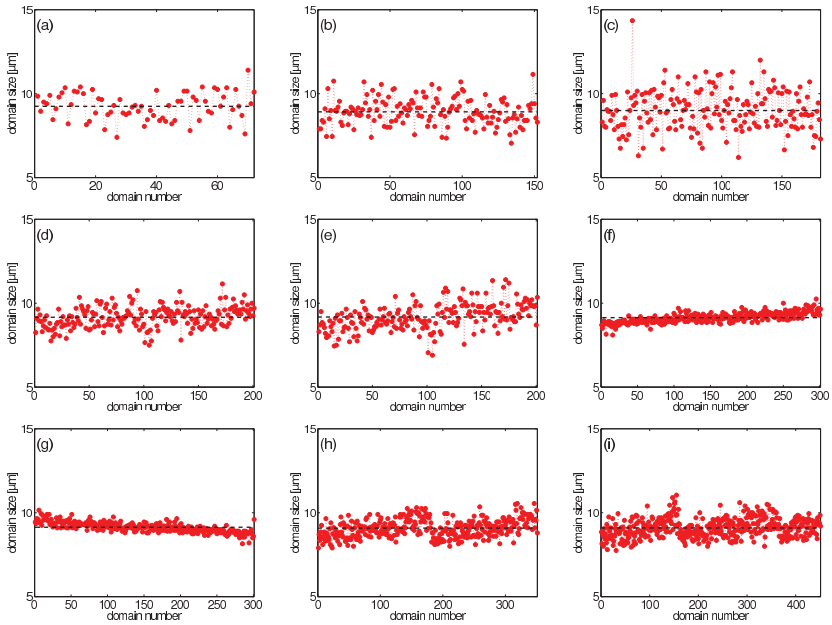

Figure 4.10: The actual sizes of the crystal domains as calculated with the algorithm. The mean value is marked with a horizontal black, dashed line. The lengths are not identical. The intuitive behaviour of the algorithm is visible in (f) and (g) chirped gratings and (h), (i) — the multiple pulse shapes.

respectively, is expected as it is obvious that a linearly chirped grating scheme results in a chirped output pulse if the input pulse is Fourier transform–limited. Additionally, (h) and (i), which are designed for the double– and triple pulses, show signs of "sectioning" — these shapes are generated pulse–by–pulse.

4.6 Pulse shaping experiment

4.6.1 Overview

The experiment was performed using a home–built Er:fibre femtosecond oscillator working at the central wavelength of 1530 nm, producing typically 300 fs chirped pulses, compressible down to ~250 fs. The full experimental configuration is shown in Fig. 4.11.

The first stage of the actual setup was a pulse compression section consisting of a pair of silicon prisms in a double–pass configuration, separated by 12 cm. It was necessary to introduce this part due to some residual chirp on the oscillator pulses, which had to be removed as the input pulses assumed in the model were Fourier transform–limited.

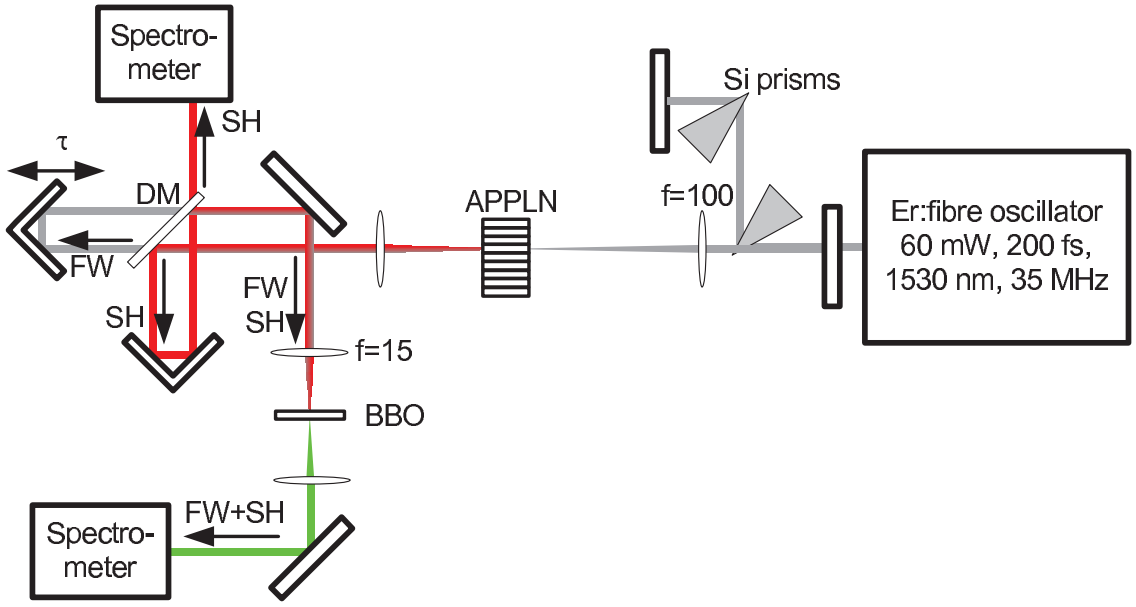

Figure 4.11: Experimental setup for pulse shaping and measurement. Beam from erbium fibre oscillator is compressed in a prismatic line and focused into an APPLN crystal. After recollimation fundamental wavelength (FW) is separated from second harmonic (SH) with a dichroic mirror (DM). Both beams are retroreflected in a Michelson interferometer, recombined and tightly focused into a thin (100 µm thick) BBO crystal phase–matched for sum frequency generation between fundamental and second harmonic. Resulting green light spectrum is used for XFROG measurement.

The compressed fundamental pulses were ready to be upconverted in the crystal, however to obtain any observable second harmonic intensity, a lens was used to focus the beam into the crystal. The optimal focal length giving the focal size ideal in terms of conversion efficiency was calculated as around 6 cm and subsequently f=5 cm was initially tested.

The red second harmonic light (765 nm) was readily visible by eye and the alignment was not very critical. After the collimating lens the remaining part of the setup was the monitoring section, namely a cross–correlator, later modified into an XFROG system for final measurements.

4.6.2 Er:fibre laser

The home–built erbium–doped fibre oscillator design was based on that presented by Lenz in [4.50] and is shown schematically in the Fig. 4.12.

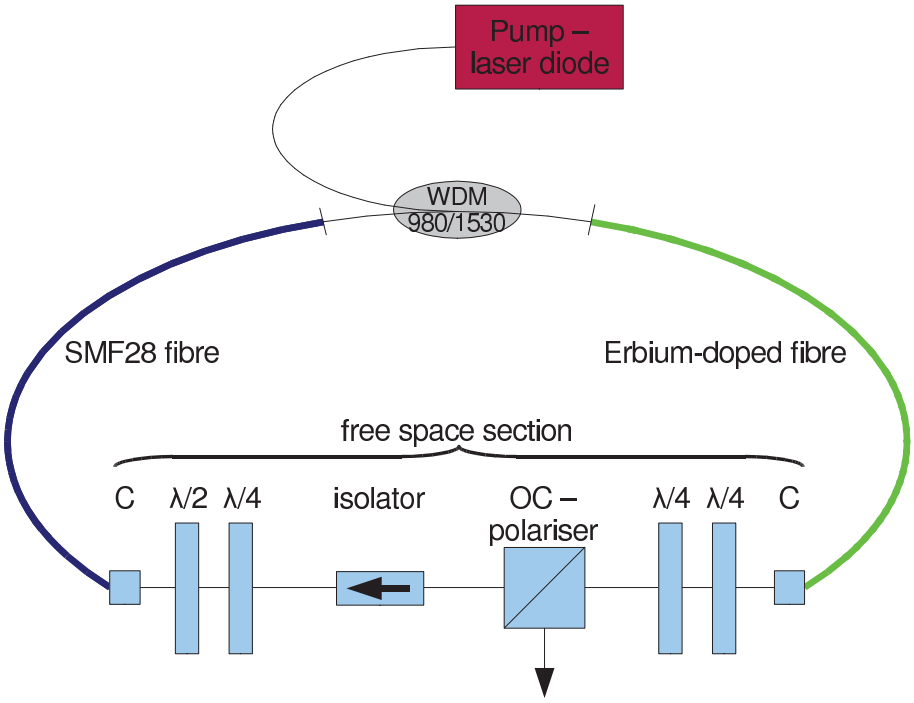

Figure 4.12: The schematic of the erbium–doped fibre oscillator. Pumping was performed with the laser diode working in a CW mode at 980 nm. C: collimators, λ/2: half–wave plate, λ/4: quarter–wave plates.

The cavity consisted of the free–space section and two fusion–spliced fibres which for the oscillating wavelength (~1530 nm) were characterised with the dispersion of the opposite signs. In the air section the beam was collimated. The unidirectional operation was forced by the Faraday isolator. The mode–locking in this type of laser is obtained by a nonlinear polarisation rotation in the fibre. This effect is peak power–dependent so for one proper alignment of the wave-plates strong pulses can be coupled back into the fibre section for feedback and the weaker ones are rejected. After reaching the steady state the single–pulse operation is established and the output is a stable pulse train. The stable pulse duration is ensured by the balanced stretching action of the erbium doped fibre and the compressing action of the SMF28 fibre. The oscillator was working in the stretched–pulse regime and the output pulses were positively chirped. To be as close as possible to the assumed situation of Gaussian unchirped pulses we used a pulse compressor consisting of two silicon prisms. The optimal distance between the prisms for the best pulse compression was of the order of 12 cm.

The oscillator was pumped with an optically pumped semiconductor vertical cavity surface emitting (VCSEL) laser, the TeleCom Coherent OPSL–980–500

model working at 980 nm and producing 500 mW of power. It was provided in a single–mode fibre pigtailed package.

The typical oscillator spectrum is shown in Fig. 4.13 and the compressed–pulse autocorrelation function in Fig. 4.14.

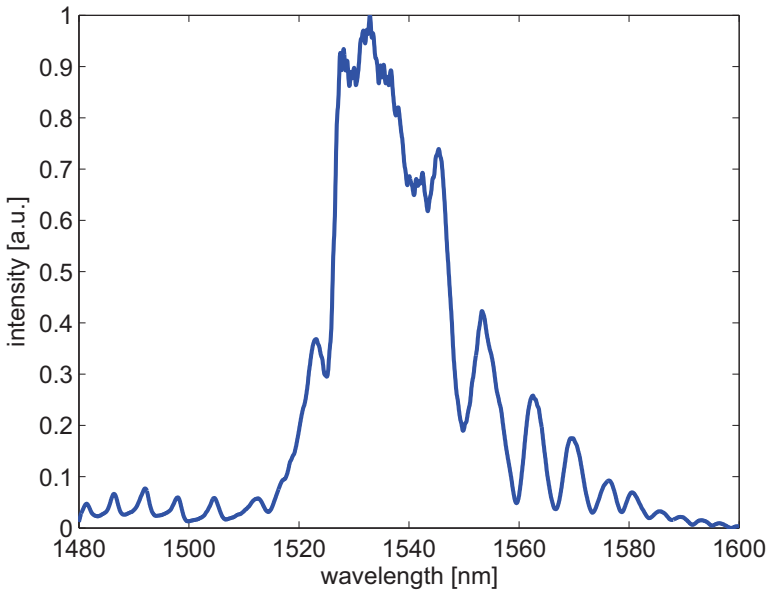

Figure 4.13: The typical spectrum of an Er:fibre oscillator used in the experiment.

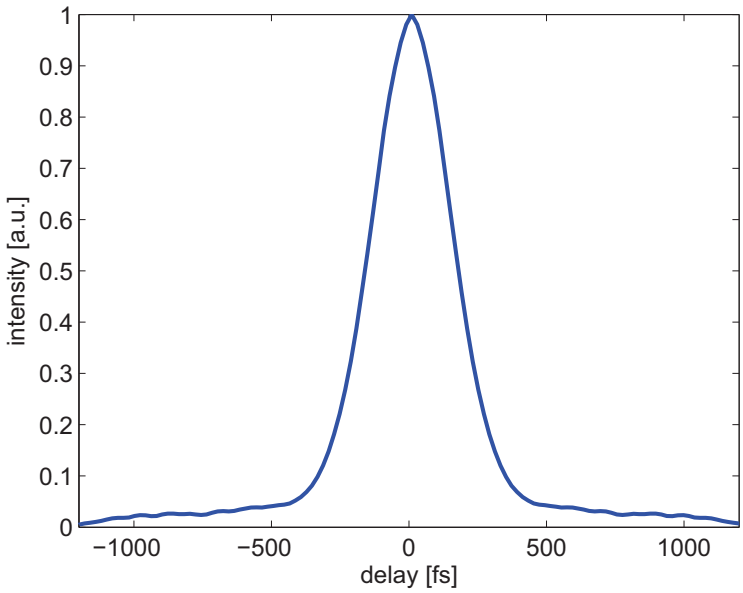

Figure 4.14: The typical autocorrelation function of compressed Er:fibre oscillator pulses used in the experiment.

The Gaussian shape–based estimation of the pulse duration after compression was 240 fs.

4.6.3 Measurement and optimisation of the shaped SH pulses

In the initial stage of the experiment the pulse measurement section was only a quality–monitoring device so a simple cross–correlator was used at that time. Both the fundamental and second harmonic beams were used, separated with a mirror dedicated for a Ti:sapphire oscillator cavity, which reflected the majority of the 765 nm light but was highly transparent for the 1530 nm component, effectively acting as a dichroic beamsplitter in the Michelson interferometer. The second harmonic retro–reflector was mounted on a piezo–stage and the relative delay between the arms was scanned at ~10 Hz frequency to obtain the cross–correlation measurement. The beams were focused into a common point inside a thin (100 µm) BBO crystal and the sum–frequency mixing signal at 510 nm was focused onto a silicon photodiode. The cross–correlation functions are shown in Fig. 4.15.

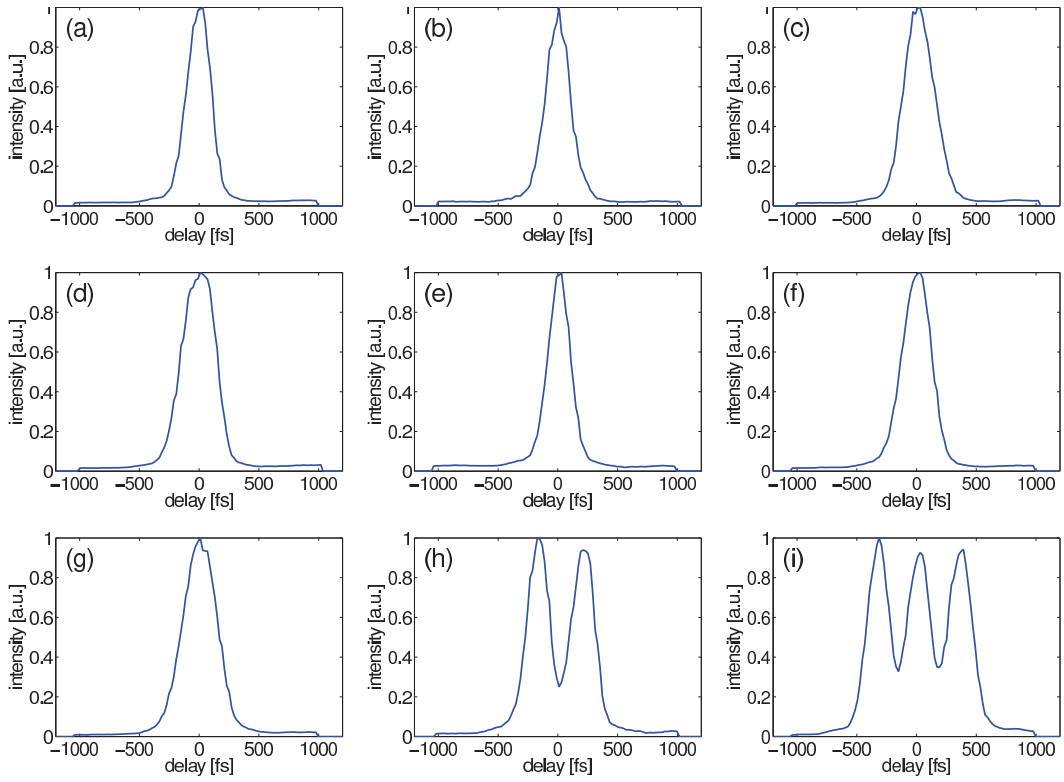

Figure 4.15: The measured cross–correlation functions of the target SH pulses shaped according to Table 4.1 with the fundamental frequency pulses.

Interestingly, this simple monitoring tool quickly revealed the fact that the 5 cm focusing lens had too short a focal length; it was found while observing the three–peaked cross–correlation function of the triple pulse and the fundamental one shown in Fig. 4.15 (i). The translation of the crystal along the beam caused an increase in the intensity of one of the peaks, apparently depending on the fact where the focus was localised. However, it was known from the model that all three intensities should be the same due to the plane wave and no–depletion approximations. The simple way to remove this intensity non–uniformity was by employing a lens with a longer focal length, losing some conversion efficiency but coming closer to the plane–wave situation. The 5 cm focusing lens was replaced with a 10 cm one, and the unwanted effect disappeared, indicating that the illumination became uniform enough under these focusing conditions.

For more exact measurements the cross–correlator was replaced with an XFROG system by the simple substitution of the photodiode with a spectrometer. The XFROG signal is obtained exactly in the same way as the cross–correlation, by nonlinear interaction of two different input pulse fields with a variable delay introduced between them, using the frequency–mixing effect:

$$I_{\mathrm{XFROG}}(\tau,\omega) = \left| \int_{-\infty}^{\infty} E_{\mathrm{SH}}(t) E_{\mathrm{F}}(t-\tau) e^{-i\omega t} dt \right|^2 . \tag{4.17}$$

The XFROG measurement apparatus required a Michelson interferometer with a variable delay in one of the arms, as already employed in the autocorrelation measurement. A frequency–mixing crystal was required and the same 0.5 mm–thick BBO crystal phase–matched for the mixing of 1530 nm and 765 nm was used for this purpose. The output signal at 510 nm was focussed on the OceanOptics USB4000 spectrometer slit for the spectrum measurement. The variable length arm retro–reflector position was precisely adjusted with a Newport NewStep motor offering 100 nm resolution. The stage movement and the spectrum acquisition were controlled by a dedicated LabVIEW program, using RS232 port for the stepper motor control and the USB port for the communication with the spectrometer. The program allowed for the modification of the delay step, the spectrum acquisition time and averaging, and for the choice of the number of points collected in one measurement. An example screenshot of the program interface is presented in Fig. 4.16.

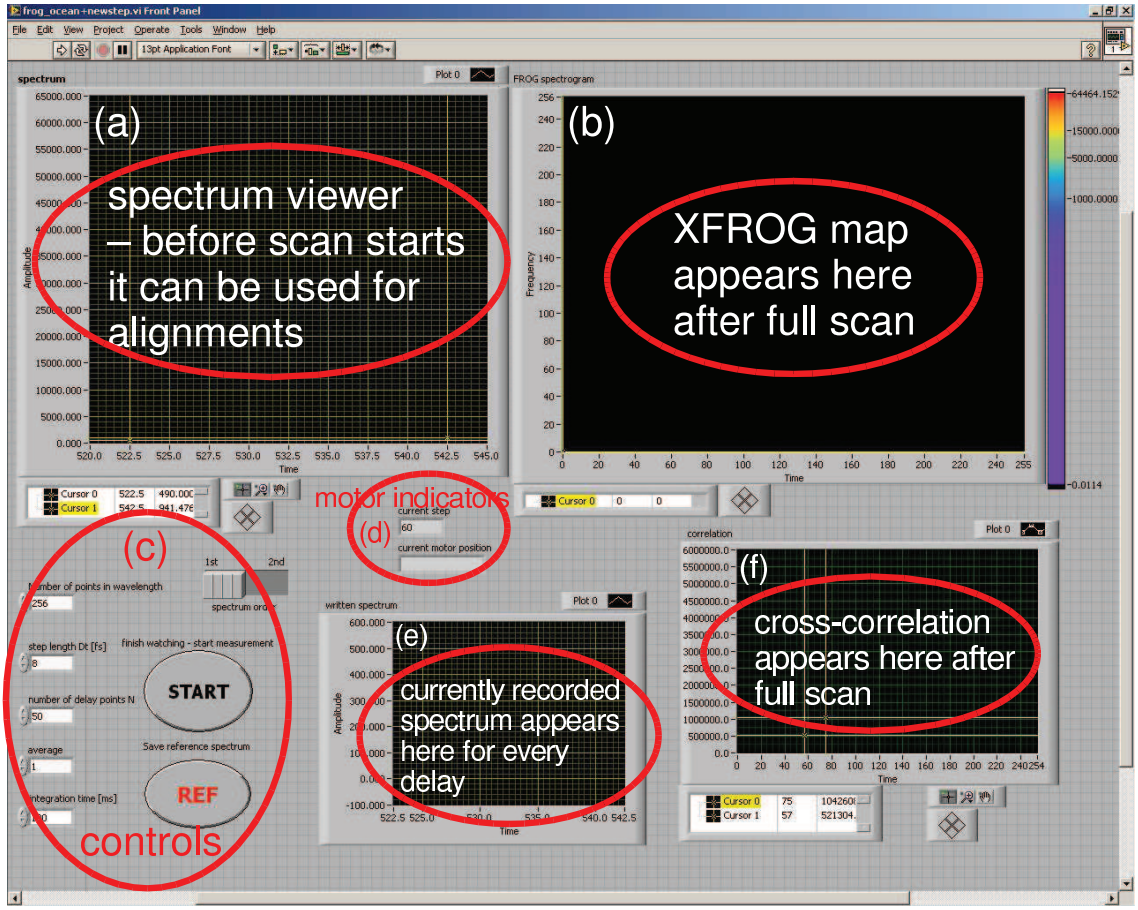

Figure 4.16: The screenshot of the LabVIEW program written for the acquisition of the XFROG data. The spectrum viewer (a) is continuously showing the output of the spectrometer before the scan commences. The vertical bars in the graph are movable and form the spectrum boundaries for the recorded traces. The panel (b) shows the XFROG map after all the spectra are collected. The controls (c) allow for the choice of the number of points in wavelength and delay, step length and spectrum acquisition features: averaging and integration time. The stepper motor indicators (d) show the current step number and the motor position which is constantly queried for while performing the scan. The written spectrum is shown during each step in the panel (e), while the graph (f) is filled with the autocorrelation function after the measurement is done.

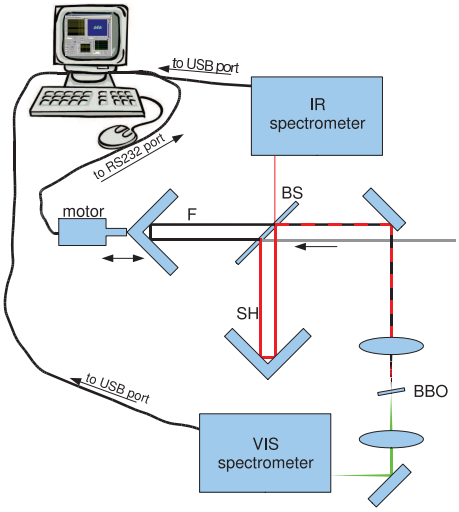

Figure 4.17: The schematic of the XFROG measurement setup. F: the arm with the fundamental beam, SH: the arm with the second harmonic, BS: dichroic beamsplitter (Ti:sapphire laser mirror), BBO: nonlinear crystal. The motor makes a step corresponding to 20 fs delay and the spectrum of the frequency–mixing signal is recorded. The setup is easily transferable to FROG apparatus by replacing the beamsplitter and tuning the BBO to the doubling position of the fundamental frequency.

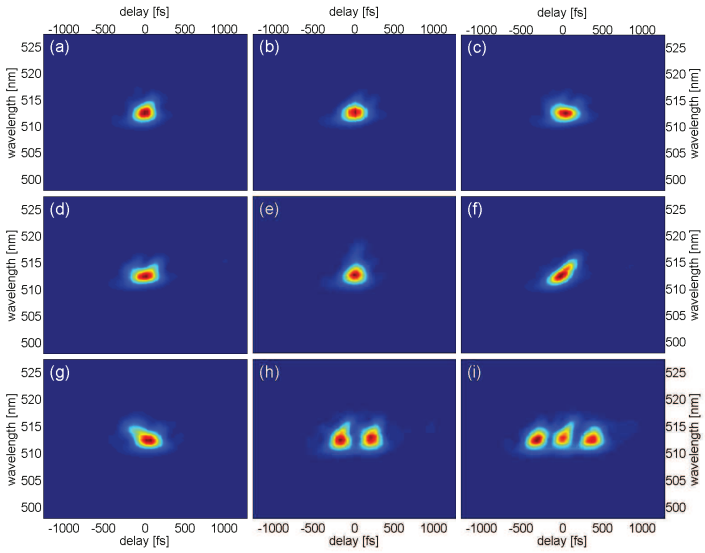

Figure 4.18: XFROG maps of shaped pulses. The delay step was chosen to be 20 fs and the spectrum resolution is 0.3 nm. After converting into the frequency domain and preparing for the retrieval using the algorithm, the points are distributed on a square matrix with dimensions 128×128.

The entire setup is shown schematically in Fig. 4.17. The Fig. 4.18 shows the measured XFROG maps.

4.7 Comparison with theory

The recorded XFROG traces contain complete information about both pulses involved so the temporal shapes of fundamental and second harmonic were retrieved from this data. The results cannot be directly compared to the originally designed target shapes due to the difference between the assumed input pulses and the actual ones. Instead, the real fundamental pulse was characterised and used as the E_{IN}, together with the E_{CRYS} based on the real domain sizes in the formula (4.14). This way the expected E_{SH} was calculated and compared to the experiment results. The comparison is shown in the Fig. 4.19.

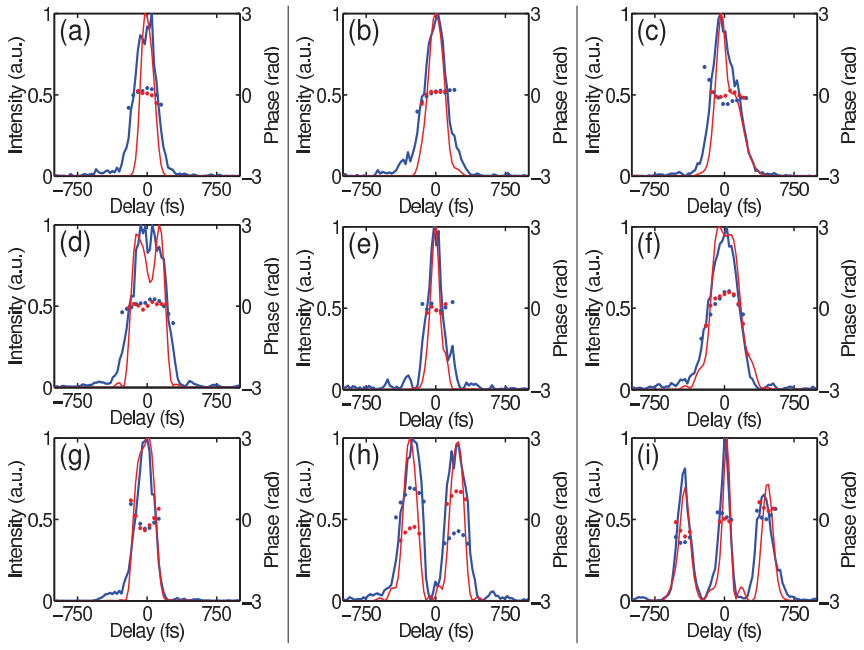

Figure 4.19: The comparison of measured (blue) and calculated (red) second harmonic pulses. The intensity is shown with solid lines and the left hand–side axis and the phase — with dots on the right hand–side axis. General agreement is good, however there are some significant differences, especially when it comes to (a) and (b). It can be explained by the presence of relatively long sections of unpoled material after the grating structure. These fragments do not contribute to the pulse shaping, but rather only add unwanted dispersion which can cause the difference.

The comparison is very satisfactory — the general agreement in terms of intensity and phase is good. There are some differences, namely the measured intensity envelopes are a bit broader than the predicted ones in the case of (a) and (b), simple Gaussian, Fourier–limited pulses. This may be caused by the propagation through a relatively long section of an unpoled crystal after the pulse is already shaped. This introduces unwanted dispersion without further contributing to the shaping process and is not taken into account in the designing algorithm. Another detail is that in the case (h) the phases are swapped, suggesting that the pulses are inverted in time but it should not be possible due to the use of the time–invariant FROG version. This is not a serious problem as the designed shape is symmetric anyway so there may have been several occasions when the data was accidentally inverted. It does not change the fact that the pulse was shaped accordingly to the theoretical prediction.

4.8 Conclusions

The experiment tested the applicability of the previously developed theory to the femtosecond pulse shaping with aperiodically poled lithium niobate crystals in the low–depletion regime. The theory proposed described the recipe for a simple and quick calculation of the shaped pulse field and additionally offered an algorithm for the design of a suitably tailored grating structure, given a known input pulse and a chosen target output one. Nine gratings were designed by means of this theory to create nine pulse shapes and the corresponding domain structures were incorporated into a commercially obtained crystal. The experiment of pulse shaping was performed with an Er:fibre femtosecond oscillator and the result pulses were accurately measured. These pulses were then compared to the simulated output of the formula, using as the input the known grating structure and the real data for the fundamental pulses. The comparison was very satisfactory and the differences were only rather small. It is estimated that the accuracy is sufficient to obtain any pulse structure if only the input spectrum is broad enough.

Any extensions of this technique into "power" applications (like femtosecond machining) are possible only when the depletion effect is included in the theory due to a high conversion efficiency expected in that case. However, it is not a general problem — the most important outcome of this experiment is the ver-

ification of the fact that a completely arbitrarily shaped copy of a femtosecond pulse may be produced with a poled lithium niobate crystal and that the result is predictable. Now the high–depletion effect needs to be put into the crystal design recipe but as long as the formula is physically accurate, the pulse will be shaped properly.

The experiment was described in a journal article [4.51], appeared as a Research Highlight in *Nature Photonics* magazine [4.52] and was presented at two conferences [4.53, 4.54].

4.9 References

[4.1] J. P. Heritage, R. N. Thurston, W. J. Tomlinson and A. M. Weiner, "Spectral windowing of frequency–modulated optical pulses in a grating compressor", *Applied Physics Letters* **47** (2), p. 87–89, 1985.

[4.2] W. S. Warren, R. Rabitz and M. Dahleh, "Coherent control of chemical reactions: the dream is alive", *Science* **259** (5101), p. 1581–1589, 1993.

[4.3] H. Kawashima, M. M. Wefers and K. A. Nelson, "Femtosecond pulse shaping, multiple–pulse spectroscopy, and optical control", *Annual Review of Physical Chemistry* **46**, p. 627–656, 1995.

[4.4] T. C. Weinacht, J. Ahn and P. H. Bucksbaum, "Controlling the shape of a quantum wavefunction", *Nature* **397**, 1999.

[4.5] R. Bartels, S. Backus, E. Zeek, L. Misoguti, G. Vdovin, I. P. Christov, M. M. Murnane and H. C. Kapteyn, "Shaped–pulse optimization of coherent emission of high–harmonic soft X–rays", *Nature* **406**, 2000.

[4.6] D. Umstadter, E. Esarey and J. Kim, "Nonlinear plasma waves resonantly driven by optimized laser pulse trains", *Physical Review Letters* **72** (8), p. 1224–1227, 1994.

[4.7] D. Meshulach and Y. Silberberg, "Coherent quantum control of two–photon transitions by a femtosecond laser pulse", *Nature* **396**, 1998.

[4.8] R. Stoian, M. Boyle, A. Thoss, A. Rosenfeld, G. Korn and I. V. Hertel, "Dynamic temporal pulse shaping in advanced ultrafast laser material processing", *Applied Physics A* **77**, p. 265–269, 2003.

[4.9] H. P. Sardesai, C.-C. Chang and A. M. Weiner, "A femtosecond code–division multiple–access communication system test bed", *IEEE Journal of Lightwave Technology* **16** (11), p. 1953–1964, 1998.

[4.10] C. J. Bardeen, V. V. Yakovlev, J. A. Squier, K. R. Wilson, S. D. Carpenter and P. M. Weber, "Effect of pulse shape on the efficiency of multiphoton processes: Implications for biological microscopy", *Journal of Biomedical Optics* **4** (3), p. 362–367, 1999.

[4.11] J. Ahn, A. Efimov, R. Averitt and A. Taylor, "Terahertz waveform synthesis via optical rectification of shaped ultrafast laser pulses", *Optics Express* **11** (20), p. 2486–2496, 2003.

[4.12] C.-C. Chang, H. P. Sardesai and A. M. Weiner, "Dispersion–free fiber transmission for femtosecond pulses by use of a dispersion–compensating fiber and a programmable pulse shaper", *Optics Letters* **23** (4), p. 283–285, 1998.

[4.13] G. Chériaux, O. Albert, V. Wänman, J. P. Chambaret, C. Félix and G. Mourou, "Temporal control of amplified femtosecond pulses with a deformable mirror in a stretcher", *Optics Letters* **26** (3), p. 169–171, 2001.

[4.14] A. Galler and T. Feurer, "Pulse shaper assisted short laser pulse characterization", *Applied Physics B* **90** (3–4), p. 427–430, 2008.

[4.15] D. Meshulach, D. Yelin and Y. Silberberg, "Adaptive real–time femtosecond pulse shaping", *Journal of the Optical Society of America B* **15** (5), p. 1615–1619, 1998.

[4.16] A. M. Weiner, D. E. Leaird, J. S. Patel and J. R. Wullert, "Programmable femtosecond pulse shaping by use of a multielement liquid–crystal phase modulator", *Optics Letters* **15** (6), p. 326–328, 1990.

[4.17] T. Brixner and G. Gerber, "Femtosecond polarization pulse shaping", *Optics Letters* **26** (8), p. 557–559, 2001.

[4.18] http://www.cri-inc.com

[4.19] http://www.bnonlinear.com

[4.20] http://www.forthdd.com

[4.21] A. M. Weiner, J. P. Heritage and E. M. Kirschner, "High–resolution femtosecond pulse shaping", *Journal of the Optical Society of America B* **5** (8), p. 1563–1572, 1988.

[4.22] http://www.hamamatsu.com

[4.23] C. Dorrer, F. Salin, F. Verluise and J. P. Huignard, "Programmable phase control of femtosecond pulses by use of a nonpixelated spatial light modulator", *Optics Letters* **23** (9), p. 709–711, 1998.

[4.24] R. Ragazzoni, E. Marchetti and G. Valente, "Adaptive–optics corrections available for the whole sky", *Nature* **403**, p. 54–56, 2000.

[4.25] J. Liang, D. R. Williams and D. T. Miller, "Supernormal vision and high–resolution retinal imaging through adaptive optics", *Journal of the Optical Society of America A* **14** (11), p. 2884–2892, 1997.

[4.26] S. Campbell, S. M. F. Triphan, R. El-Agmy, A. H. Greenaway and D. T. Reid, "Direct optimization of femtosecond laser ablation using adaptive wavefront shaping", *Journal of Optics A* **9** (11), p. 1100–1104, 2007.

[4.27] E. Steinhaus and S. G. Lipson, "Bimorph piezoelectric flexible mirror", *Journal of the Optical Society of America* **69** (3), p. 478–481, 1979.

[4.28] P. Wnuk, C. Radzewicz and J. S. Krasiński, "Bimorph piezo deformable mirror for femtosecond pulse shaping", *Optics Express* **13** (11), p. 4154–4159, 2005.

[4.29] E. Zeek, K. Maginnis, S. Backus, U. Russek, M. Murnane, G. Mourou, H. Kapteyn and G. Vdovin, "Pulse compression by use of deformable mirrors", *Optics Letters* **24** (7), p. 493–495, 1999.

[4.30] J. Garduño–Mejía, A. H. Greenaway and D. T. Reid, "Designer femtosecond pulses using adaptive optics", *Optics Express* **11** (17), p. 2030–2040, 2003.

[4.31] M. Hacker, G. Stobrawa, R. Sauerbrey, T. Buckup, M. Motzkus, M. Wildenhain and A. Gehner, "Micromirror SLM for femtosecond pulse shaping in the ultraviolet", *Applied Physics B* **76** (6), p. 711–714, 2003.

[4.32] `http://www.okotech.com`

[4.33] `http://www.bostonmicromachines.com`

[4.34] M. A. Dugan, J. X. Tull and W. S. Warren, "High–resolution acousto–optic shaping of unamplified and amplified femtosecond laser pulses", *Journal of the Optical Society of America B* **14** (9), p. 2348–2358, 1997.

[4.35] P. Tournois, "Acousto–optic programmable dispersive filter for adaptive compensation of group delay time dispersion in laser systems", *Optics Communications* **140** (4–6), p. 245–249, 1997.

[4.36] F. Verluise, V. Laude, Z. Cheng, C. Spielmann and P. Tournois, "Amplitude and phase control of ultrashort pulses by use of an acousto–optic programmable dispersive filter: pulse compression and shaping", *Optics Letters* **25** (8), p. 575–577, 2000.

[4.37] `http://www.fastlite.com`

[4.38] E. Seres, R. Herzog, J. Seres, D. Kaplan and C. Spielmann, "Generation of intense 8 fs laser pulses", *Optics Express* **11** (3), p. 240–247, 2003.

[4.39] A. M. Weiner, "Femtosecond pulse shaping using spatial light modulators", *Review of Scientific Instruments* **71** (5), p. 1929–1960, 2000.

[4.40] C. Radzewicz, M. J. la Grone and J. S. Krasiński, "Passive pulse shaping of femtosecond pulses using birefringent dispersive media", *Applied Physics Letters* **69** (2), p. 272–274, 1996.

[4.41] S. Zhou, D. Ouzounov, H. Li, I. Bazarov, B. Dunham, C. Sinclair and F. W. Wise, "Efficient temporal shaping of ultrashort pulses with birefringent crystals", *Applied Optics* **46** (35), p. 8488–8492, 2007.

[4.42] S. K. Turitsyn, V. K. Mezentsev and E. G. Shapiro, "Dispersion–managed solitons and optimization of the dispersion management", *Optical Fiber Technology* **4** (4), p. 384–452, 1998.

[4.43] P. Petropoulos, M. Ibsen, A. D. Ellis and D. J. Richardson, "Rectangular pulse generation based on pulse reshaping using a superstructured fiber Bragg grating", *IEEE Journal of Lightwave Technology* **19** (5), p. 746–752, 2001.

[4.44] L. R. Chen, S. D. Benjamin, P. W. E. Smith, J. E. Sipe and S. Juma, "Ultrashort pulse propagation in multiple–grating fiber structures", *Optics Letters* **22** (6), p. 402–404, 1997.

[4.45] S. Longhi, M. Marano, P. Laporta, O. Svelto and M. Belmonte, "Propagation, manipulation, and control of picosecond optical pulses at 1.5 μm in fiber Bragg gratings", *Journal of the Optical Society of America B* **19** (11), p. 2742–2757, 2002.

[4.46] G. Imeshev, A. Galvanauskas, D. Harter, M. A. Arbore, M. Proctor and M. M. Fejer, "Engineerable femtosecond pulse shaping by second–harmonic generation with Fourier synthetic quasi–phase–matching gratings", *Optics Letters* **23** (11), p. 864–866, 1998.

[4.47] D. T. Reid, "Engineered quasi–phase–matching for second–harmonic generation", *Journal of Optics A* **5** (4), p. S97–S102, 2003.

[4.48] U. K. Sapaev and D. T. Reid, "General second–harmonic pulse shaping in grating–engineered quasi–phase–matched nonlinear crystals", *Optics Express* **13** (9), p. 3264–3276, 2005.

[4.49] W. H. Press, S. A. Teukolsky, W. T. Vetterling and B. P. Flannery, *Numerical Recipes*, Cambridge University Press.

[4.50] G. Lenz, K. Tamura, H. A. Haus and E. P. Ippen, "All–solid–state femtosecond source at 1.55 μm", *Optics Letters* **20** (11), p. 1289–1291, 1995.

[4.51] Ł. Kornaszewski, M. Kohler, U. K. Sapaev and D. T. Reid, "Designer femtosecond pulse shaping using grating–engineered quasi–phase–matching in lithium niobate", *Optics Letters* **33** (4), p. 378–380, 2008.

[4.52] Research Highlights, "Colour–controllable LEDs, three–dimensional fluorescence nanoscopy, medical nanotags, and more", *Nature Photonics* **2** (3), p. 128–129, 2008.

[4.53] Ł. Kornaszewski, M. Kohler, D. T. Reid and U. K. Sapaev, "Designer femtosecond pulse shaping using grating–engineered quasi–phasematching in lithium niobate", in *Conference on Lasers and Electro–Optics/Quantum Electronics and Laser Science Conference and Photonic Applications Systems Technologies 2008 Technical Digest*, p. CWK3, (Optical Society of America, Washington, DC), 2008.

[4.54] Ł. Kornaszewski, M. Kohler, D. T. Reid and U. K. Sapaev, "Designer femtosecond pulse shaping using grating–engineered quasi–phasematching in lithium niobate", in *XVI Conference on Ultrafast Phenomena*, p. MON5l.9, (European Physical Society, 68060 Mulhouse Cedex, France), 2008.

Chapter 5

Conclusions and outlook

In my thesis I have presented the design process and the construction of two femtosecond optical parametric oscillators and one femtosecond pulse shaper, all based on the technology of periodically poled lithium niobate which permits flexible and engineerable phasematching of all $\chi^{(2)}$ processes within its transparency range.

The first device, the Ti:sapphire–pumped OPO was used as a broadband light source for methane sensing by utilising a mid–IR Fourier–transform spectroscopy approach. With the exception of thermal sources, broadband coverage in the spectral region of 3.3 μm is unavailable from any other sources but promises high efficiency of CH_4 detection. The experiment revealed an available practical sensitivity of around 1% which is still unsatisfactory compared to realistic requirements and performance using thermal sources, however there are some significant benefits in the concept demonstrated and also much can be improved. For example, in Chapter 2 I suggested the addition of a reference circuit which could remove the noise associated with the OPO's vulnerability to environmental noise. Then the full potential of this light source would be available and, based on the results obtained with a similar source [5.1] a sensitivity much better than 2 ppm would be possible. The reason for optimism here is the novel application of a photonic bandgap fibre which optimises the overlap between the light beam and the analysed gas volume and offers long interaction paths. It has been shown that precise drilling of the fibre side is possible [5.2] so in principle it is also possible that a sensing device employing such a fibre with multiple holes can exist without the need to load the gas into the fibre core using active pumping and so

detect the presence of the gas straight from the environment.

It would be a big step towards building a really portable device if the construction of the light source was simpler. The need for three laser systems in series makes the whole apparatus only rather a sophisticated and fragile laboratory device. There are already available quantum cascade lasers, lead– and antimonide–based laser diodes operating at the wavelength of the fundamental methane absorption (3.3 µm and 7.7 µm) but they are still not simple devices, and usually both diode and detector require cryogenic cooling. A sufficiently advantageous compromise would be the OPO pumped by a mode–locked laser diode. Pulse energies emitted by such diodes are three orders of magnitude smaller than these from Ti:sapphire oscillators and it would be a great challenge to obtain parametric oscillation but that is probably an idea to pursue. There are low–noise semiconductor optical amplifiers available at 1.3 µm [5.3] and recently multiple quantum–dot femtosecond oscillators were developed [5.4], however their peak powers are of the order of 1 W due to typically high (20 GHz) repetition frequency, so parametric oscillation could be difficult to obtain under these pumping conditions.

Another, still cheaper approach for the methane sensing at 3.3 µm would be using a fibre laser to pump the OPO, namely joining the pump from Chapter 3 with the cavity from Chapter 2, possibly with a modified grating, to replace the large and expensive Nd:YVO_4/Ti:sapphire oscillator system with a cheaper and potentially smaller fibre MOPA system. The spectral region of 3.3 µm (ν_3 oscillation) would be still accessible then.

An interesting alternative would be using a mode–locked Yb:KYW laser (for example, one similar to the system presented in [5.5]) for the OPO pumping. The laser itself is commonly pumped by butterfly–packaged pigtailed laser diodes which now are a mature and inexpensive technology. Moreover, the properties of the laser crystal remove the necessity for complicated thermal management, making the whole potential InGaAs diode/Yb:KYW laser/OPO system an attractive, cheap and simple tunable light source.

When it comes to the project started with the development of the long–cavity OPO (Chapter 3), I think it was a big success and there is still much to do and it is all well within the range of the current group's capabilities. The prediction is that cavity dumping will yield easy access to hundreds of nanojoules of signal energy

and then silicon machining will be feasible. Specifically, increasing the pump power from 2 W (demonstrated) to 7 W (the maximum available) should allow the extraction of ≈70 nJ signal pulses. Cavity dumping could access pulses with around ten–times higher energy again, yielding (conservatively), 500 nJ pulses.

More interesting prospects appear when frequency doubling is taken into account. The second harmonic generation may be either incorporated into the OPO crystal (intracavity) or performed outside the cavity, or the pump light may be upconverted prior to being launched into the oscillator. For example, the second harmonic of the long–cavity OPO described in Chapter 3 may potentially cover the spectral range of Ti:sapphire oscillators emission thus replacing them with a cheaper and simpler alternative.

The pulse shaping scheme demonstrated in Chapter 4 works by a second harmonic generation, and it could be used in an intracavity configuration to improve its efficiency. The shaping crystal design process would need to be completed by inclusion of the high depletion regime, but this is just a matter of extending the equations to a full 3–wave analysis, and attempts have been made by other groups already [5.6].

A separate interesting project could concentrate on passive modelocking of a holmium laser which hasn't been demonstrated yet. It offers broad emission spectra centred around 2 μm (for example 200 nm in $YAlO_3$ host material [5.7]). It is especially suitable for the pumping of an OPO based on ZGP crystal, in which tunability of a single device in the range of 3.8–12.4 μm has been shown, however at slightly different pumping wavelength [5.8]. At these wavelengths many gas detection systems can operate. Moreover, this spectral region could be a field of even more experiments exploiting optical nonlinearity if femtosecond pulses were readily available.

The world of parametric processes seems to offer a response to any demand of a light source — power may be scaled, wavelength may be tuned and CW or short pulse operation may be obtained. Potential applications seem to be countless and all problems solvable, waiting only for a researcher to identify them and then design and engineer a proper device. Not many events in the experimentalist's life are more rewarding than a bright flash of a parametric oscillator light after weeks of patient adjustments and I look forward to more of these.

5.1 References

[5.1] K. A. Tillman, R. R. J. Maier, D. T. Reid and E. D. McNaghten, "Mid–infrared absorption spectroscopy of methane using a broadband femtosecond optical parametric oscillator based on aperiodically poled lithium niobate", *Journal of Optics A* **7**, p. S408–S414, 2005.

[5.2] C. J. Hensley, D. H. Broaddus, C. B. Schaffer and A. L. Gaeta, "Photonic band–gap fiber gas cell fabricated using femtosecond micromachining", *Optics Express* **15** (11), p. 6690–6695, 2007.

[5.3] L. F. Tiemeijer, P. J. A. Thijs, T. van Dongen, R. W. M. Slootweg, J. M. M. van der Heijden, J. J. M. Binsma and M. P. C. M. Krijn, "Polarization insensitive multiple quantum well laser amplifiers for the 1300 nm window", *Applied Physics Letters* **62** (8), p. 826–828, 1993.

[5.4] E. U. Rafailov, M. A. Cataluna, W. Sibbett, N. D. Ilinskaya, Y. M. Zadiranov, A. E. Zhukov, V. M. Ustinov, D. A. Livshits, A. R. Kovsh and N. N. Ledentsov, "High–power picosecond and femtosecond pulse generation from a two–section mode–locked quantum–dot laser", *Applied Physics Letters* **87** (8), p. 081107, 2005.

[5.5] G. Palmer, M. Emons, M. Siegel, A. Steinmann, M. Schultze, M. Lederer and U. Morgner, "Passively mode–locked and cavity–dumped Yb:$KY(WO_4)_2$ oscillator with positive dispersion", *Optics Express* **15** (24), p. 16017–16021, 2007.

[5.6] U. K. Sapaev and G. Assanto, "Efficient high-harmonic generation in engineered quasi–phase matching gratings", *Optics Express* **16** (1), p. 1–6, 2008.

[5.7] B. Q. Yao, X. M. Duan, L. L. Zheng, Y. L. Ju, Y. Z. Wang, G. J. Zhao and Q. Dong, "Continuous–wave and Q-switched operation of a resonantly pumped Ho:$YAlO_3$ laser", *Optics Express* **16** (19), p. 14668–14674, 2008.

[5.8] K. L. Vodopyanov, F. Ganikhanov, J. P. Maffetone, I. Zwieback and W. Ruderman, "$ZnGeP_2$ optical parametric oscillator with 3.8-12.4-μm tunability", *Optics Letters* **25** (11), p. 841–843, 2000.